SOLAR WIND ENTRY INTO THE MAGNETOSPHERE UNDER NORTHWARD IMF CONDITIONS

BY

WENHUI LI

B.S. in Physics, University of Science and Technology of China (1993)
M.S. in Physics, University of New Hampshire (1999)
M.S. in Computer Science, University of New Hampshire (2003)

DISSERTATION

Submitted to the University of New Hampshire
in Partial Fulfillment of
the Requirements for the Degree of

Doctor of Philosophy

in

Physics

May 2007

This dissertation has been examined and approved.

Dissertation director, Joachim Raeder

Associate Professor of Physics

Terry G. Forbes

Research Professor of Physics

Lynn Kistler

Associate Professor of Physics

Eberhard Möbius

Professor of Physics

Karsten Pohl

Associate Professor of Physics

Date

DEDICATION

To my parents, my wife and my son.

ACKNOWLEDGMENTS

My dissertation research was supported by NSF grants ATM 0420905 and ATM 0427754, LANL IGPP mini-grant 1518, and by grant ATM-0503189 from the National Science Foundation GEM program. I would like to thank the ACE plasma and magnetometer teams, the Cluster HIA and FGM teams, the LANL MPA team, NASA IMAGE FUV team, International Monitor for Aurora Geomagnetic Effects (IMAGE) magnetometer network, and NASA CDAweb for providing their data and plotting the data. The computations were performed at the National Center for Supercomputer Applications (NCSA), at the San Diego Supercomputer Center (SDSC), and on the Zaphod Beowulf cluster which was in part funded by the Major Research Instrumentation program of the National Science Foundation under grant ATM-0420905.

In particular, I wish to first thank my excellent mentor and friend, Professor Joachim Raeder, who has provided me this excellent research opportunity, given me tremendous help, and exceptional guidance. Working with him is a very pleasant and fruitful experience. I have benefited greatly from his reading and correction of my writing in papers, proposals, and this dissertation.

I am also very grateful to my doctoral committee and wish to thank Professor Terry Forbes, Professor Lynn Kistler, Professor Eberhard Möebius, and Professor Karsten Pohl for their suggestions and encouragement.

I would like to thank other people that directly involved in my dissertation research. I would like to specially thank Dr. Michelle Thomsen at Los Alamos National Laboratory (LANL). I am very grateful for her warm welcome and generous help and commitment during my visit at LANL. I have also benefited a lot from her insightful advices. I would like to thank Dr. Benoit Lavraud at LANL who has given great ideas and advices for my research and great help in my writing of paper and preparing presentations. I would like to thank Dr. Tai Phan and Dr. Marit Øieroset at Space Sciences Laboratory, UC Berkeley,

who have given great help in writing paper and great advices about the study of cold dense plasma sheet. I would like to thank Dr. Yongli Wang at NASA Goddard Space Flight Center for the valuable discussion about the MHD model.

My thanks must go to my colleagues and friends here in OpenGGCM group in Space Science Center at University of New Hampshire. Dr. John Dorelli is always happy to answer my questions about magnetic reconnection. He also helped me in installing software and running 3D visualization. Dr. Douglas Larson has provided generous help in my analysis, and valuable advices for my research. The humorous conversations with him and his jokes let me have a joyful time here. Tom Fogal and Burlen Loring have provide much help in visualization of the simulation data as well as in solving computer problems. Dr. Kai Germaschewski is always enthusiastic and prompt in helping running the supercomputer Zaphod cluster and solving other Linux problems. Dr. Eddie Kaghashvili is always willing to help and give advices.

I greatly appreciate Ms. Amber Perkins, and Ms. Katie Makem for their enthusiastic help during my research and study in the Space Science Center and the Department of Physics.

My special gratitude goes to Professor Eberhard Möebius who had given great support and help in my early career development in space science when I was working on ACE/SEPICA data. I would also like to thank Professor James Ryan and Professor Olof Echt whom I ever worked with. I would like to thank all the professors in Physics Department that have taught me, especially Professor Richard Kaufmann, Professor Charles Farrugia, and Professor Joseph Hollweg who have taught me space physics. I also would like to thank professors like Professor R. Daniel Bergeron, Professor Ted Sparr, and Professor Pilar de la Torre in Computer Science Department where I learned my computer and visualization techniques, which have helped me a lot in this dissertation research. I have received invaluable instruction, mentoring and encouragement from all these scientists and educators.

I am also very thankful for the education received in China. Without it, I cannot come

to this stage in the United States.

Finally, I would like to thank my family, especially my wife Huini Tang who has given me endless support and love, and my son, Andrew, who has given me so much happiness and inspiration.

TABLE OF CONTENTS

LIST OF TABLES

LIST OF FIGURES

ABSTRACT

SOLAR WIND ENTRY INTO THE MAGNETOSPHERE UNDER NORTHWARD IMF CONDITIONS

by

WENHUI LI
University of New Hampshire, May, 2007

The state of the plasma sheet in the magnetosphere is usually observed to be hot (1-10 keV) and tenuous ($\sim$0.1 cm^{-3}). However, sometimes part of it is observed to be colder ($<$ 1 keV) and denser ($\sim$1 cm^{-3}), and the plasma flow is almost stagnant. Much higher density ($\sim$10 cm^{-3}) plasma material (superdense plasma sheet) is also sometimes observed near the geosynchronous orbit. The cold dense plasma sheet (CDPS) is usually observed after a period of northward interplanetary magnetic field (IMF), which is also a necessary condition for the formation of a superdense plasma sheet (SDPS). Since the CDPS is generally absent of a cold O^+ component, and the ionospheric outflow is strong only under southward IMF condition, the source of the CDPS is thought to be the solar wind.

Usually, solar wind plasma and energy entry into the magnetosphere is considered to occur mainly during the southward IMF condition through reconnection processes that first occur at the dayside magnetopause and then in the magnetotail. However, the formation of CDPS suggests that there are also certain processes that let solar wind enter the magnetosphere when the IMF is northward. The purpose of this dissertation study is to find out the mechanism that transports solar wind plasma into the magnetosphere under northward IMF conditions, and thus to find out the mechanism of the formation of CDPS and SDPS.

To study the solar wind entry mechanism, I use global simulations of the magnetosphere in conjunction with the analysis of observation data. The model used here is the Open Global Geospace Circulation Model (OpenGGCM), which is a magnetosphere MHD model with a stretched grid that has higher grid resolution near the Earth. The simulation is driven by the upstream solar wind input. I run simulations for several CDPS events to

validate the model by comparing the simulation results with observations. I then establish that the double high-latitude reconnection process is the dominant process that leads to the entry of solar wind plasma under northward IMF conditions, and that it is sufficient to form the CDPS. With the successful simulation of CDPS events, I continue to study a SDPS event in detail using simulation and observations from a series of spacecraft. I find that the southward IMF following a long period of northward IMF condition compresses the pre-existing CDPS, and sets off the near-tail reconnection that causes the compressed CDPS to be pushed and accelerated toward the Earth and form the SDPS near the geosynchronous orbit.

I further systematically study how the solar wind plasma enters the magnetosphere due to double high-latitude reconnection for various solar wind, northward IMF and geomagnetic dipole conditions. I trace flow paths from the solar wind and study the variation of the magnetic field line topology along the flow paths. I find that there is an entry window through which the solar wind plasma can enter the magnetosphere as a result of double high-latitude reconnection under northward IMF conditions. I show how the entry window depends on solar wind, IMF and geomagnetic dipole parameters. With the entry window, I estimate the solar wind plasma entry rate for various conditions. I find that the entry rate under northward IMF conditions is of the order of 10^{26} to 10^{27} particles per second. I also estimate the conditions at which solar wind plasma entry is most efficient.

CHAPTER 1

INTRODUCTION

1.1 Magnetosphere under Northward IMF Conditions

As the supersonic magnetized solar wind plasma blows onto the Earth, the geomagnetic field forms a cavity within the solar wind, which is called the Earth's magnetosphere. There is a standing shock wave, the bow shock, in front of the magnetosphere, where the supersonic solar wind transits to subsonic flow. The magnetopause is a current layer that separates the solar wind and the magnetosphere. The region between the magnetopause and the bow shock is the magnetosheath where the solar wind plasma flows around the magnetopause. Inside the magnetosphere there are regions like plasma mantle, tail lobe, plasma sheet, radiation belts, plasmasphere, and boundary layers between these regions. Figure 1-1 shows a sketch of the magnetosphere.

The solar wind interaction with a magnetosphere is a complex process. A gas dynamic model was developed by (*Spreiter et al.*, 1966) to describe some basic properties around the magnetosphere such as the magnetosheath and the flow around the magnetosphere. Magnetic reconnection between the geomagnetic dipole field and the interplanetary magnetic field (IMF) traveling with the solar wind is generally believed to be the dominant process that affects the properties and structure of the Earth's magnetosphere (*Dungey*, 1961, 1963; *Russell and Elphic*, 1979; *Cowley*, 1982).

Magnetic reconnection requires the two merging fields to be antiparallel or partially antiparallel (*Dungey*, 1961; *Petschek*, 1964; *Fuselier et al.*, 2000). Since the orientation of the geomagnetic dipole field is relatively stable, the IMF direction then

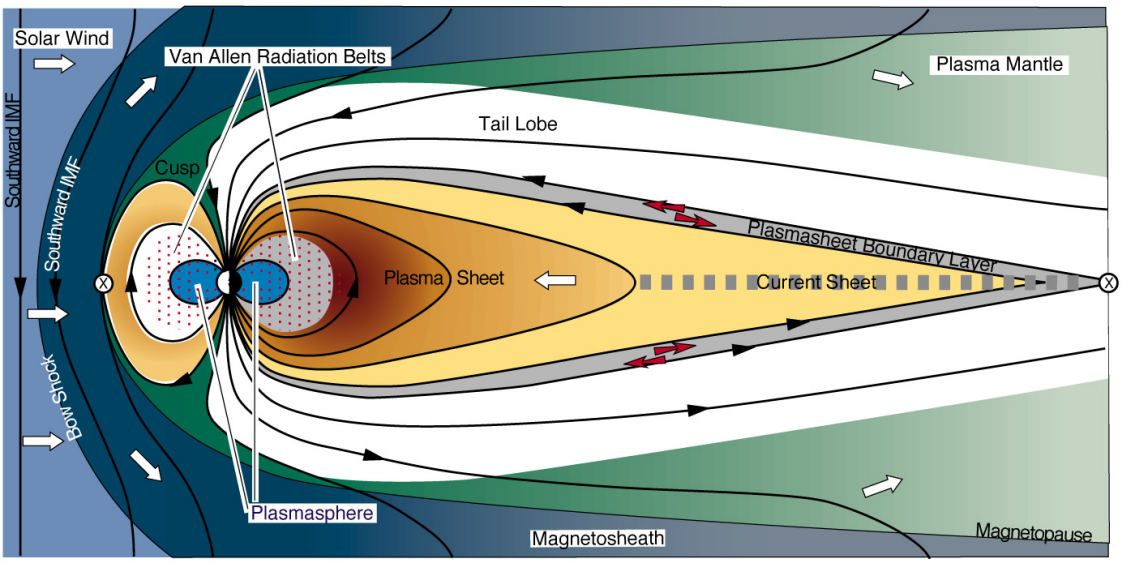

Figure 1-1: A sketch of the Earth's magnetosphere under southward IMF condition (adapted from T. W. Hill). The two circles with X inside indicate the locations of magnetic reconnection.

determines the properties of magnetic reconnection and thus the mechanism in which the magnetic reconnection affects the properties and structure of the magnetosphere.

When the IMF is southward, an IMF field line can reconnect with a geomagnetic field line at the dayside subsolar region as shown in Figure 1-2 (*Dungey*, 1961; *Cowley*, 1980; *Rosenbauer et al.*, 1975; *Sckopke et al.*, 1981). The two resulting new open field lines are then convected tailward by the solar wind flow. The magnetic tail is then formed from such open field lines. The magnetic tail is divided into northern tail lobe and southern tail lobe by a current sheet between them. The boundary between the tail lobes and the solar wind is the tailward magnetopause. In the tail, there is another magnetic reconnection process possible between the northern lobe field and the southern lobe field. This reconnection process results in a plasma boundary layer (PSBL) between the plasma sheet and the tail lobes. Transient magnetic reconnection in the tail may also occur between northern field and southern field of the plasma sheet, causes substorms and creates plasmoids, which are detached from the magne-

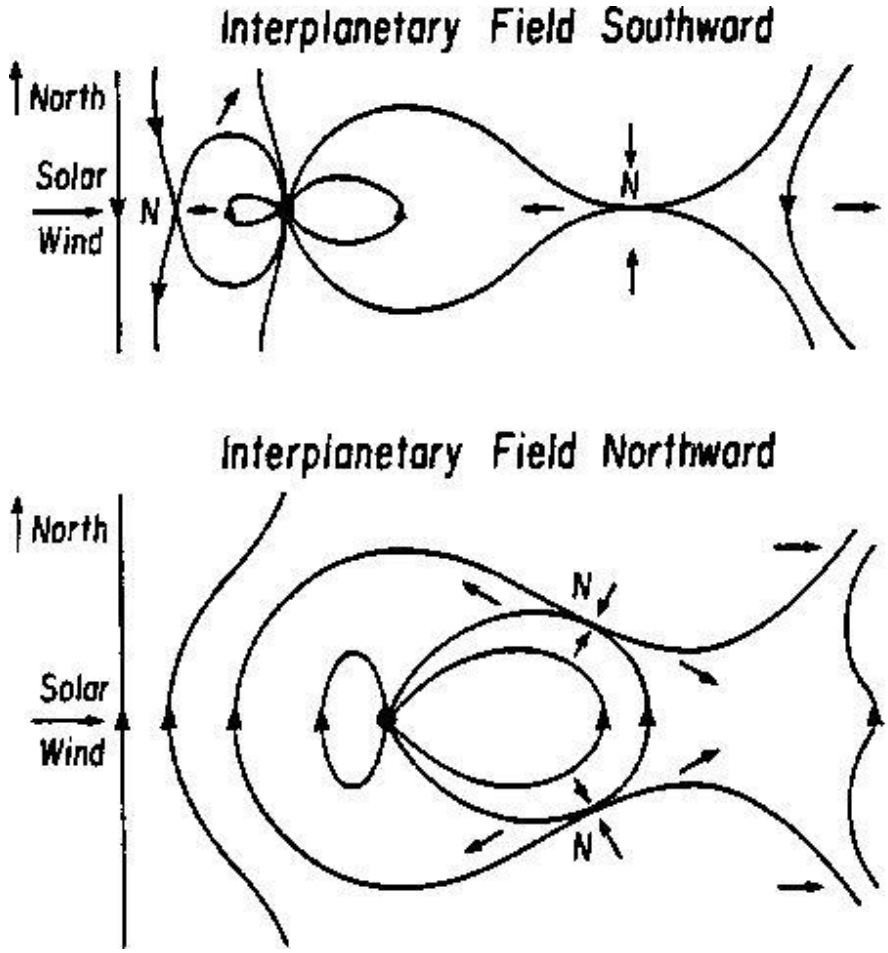

Figure 1-2: The Dungey reconnection model of the interaction of the interplanetary magnetic field with the terrestrial magnetic field.

tosphere and flow tailward. Reconnection at the dayside and in the tail completes a circle of field line convection, which is mirrored in the ionosphere. Solar wind plasma and energy can enter into the magnetosphere and down to the ionosphere through the cusp and via these two reconnection processes. Figure 1-1 shows a sketch of the magnetosphere under southward IMF conditions.

When the IMF is northward, it is not antiparallel to the geomagnetic field at the dayside subsolar region. Therefore, there will be no magnetic reconnection there, and reconnection in the tail will be reduced substantially. However, magnetic reconnection now occurs mainly at a location near the poleward cusp under northward IMF conditions. The properties and structure of the magnetosphere will change accordingly. In this section, I will discuss the properties and structure of the magnetosphere under northward IMF conditions.

1.1.1 High-latitude reconnection

Dungey [1963] first proposed that a northward interplanetary magnetic field (IMF) would be antiparallel to Earth's field at points poleward of the cusps and make reconnection possible there as shown in Figure 1-2. Such reconnection is usually called high-latitude reconnection. *Russell* [1972] proposed that the IMF field lines interconnect with open tail lobe field lines rather than closed field lines in either one or the other hemisphere. For a tilted geomagnetic field, *Cowley* [1981, 1983] suggested that a northward IMF field line merges with a closed geomagnetic field line in the northern hemisphere, forming an open field line that drapes over the dayside magnetopause and another open field line that connects to the southern hemisphere. After some time, the over-draped open field line merges with one of the previously opened field lines in the southern hemisphere, creating a new closed dayside field line and a completely detached field line.

Global magnetosphere MHD models have reproduced the high-latitude reconnection under northward IMF conditions (*Berchem et al.*, 1995; *Raeder et al.*, 1997; *Gombosi et al.*, 1998; *Guzdar et al.*, 2001). Observational evidence to support this physical process has also been presented in studies by *Omelchenko et al.* [1983], *Gosling et al.* [1991, 1996], *Kessel et al.* [1996], *Matsuoka et al.* [1996], *Fuselier et al.* [2000], *Le et al.* [2001], *Onsager et al.* [2001], *Phan et al.* [2003], and *Lavraud et al.* [2002,2004,2005b]. From the three-dimensional electron and ion distribution measured by the Polar Hydra instrument, *Onsager et al.* [2001] identified several distinct boundary layer regions associated with the high-latitude reconnection processes under northward IMF condition: (1) the cusp; (2) the magnetopause current layer; (3) magnetosheath field lines that have interconnected in only the Northern Hemisphere; (4) magnetosheath field lines that have interconnected in only the Southern Hemisphere; (5) magnetosheath field lines that have interconnected in both the Northern and Southern Hemispheres; (6) magnetosheath that is disconnected from the terrestrial magnetic field; and (7) high-latitude plasma sheet field lines that are participating in magnetosheath reconnection. They also found that reconnection during a northward IMF time period was occurring at high latitudes over a broad local-time extent, interconnecting magnetosheath and lobe and/or plasma sheet field lines in both the Northern and Southern Hemisphere. Newly closed boundary layer field lines were observed as reconnection occurred first at high latitudes in one hemisphere and then later in the other. This scenario was further confirmed observationally by *Lavraud et al.* [2005c, 2006b].

Although observations have shown substantial evidence of high-latitude reconnection, it is difficult to determine whether IMF reconnects with terrestrial open field or closed field, or both, and under what conditions. Since simulations can reproduce high-latitude reconnection, we may be able to find out the detailed processes by

the analysis of the simulation results. This is one of the primary objectives of this dissertation.

1.1.2 Magnetosphere boundary

The Magnetopause is the boundary between IMF and geomagnetic field with a current layer separating these two fields. Adjoining the magnetopause, there are several exterior boundary layers such as the dayside and tail flank portions of the low-latitude boundary layer (LLBL), the high latitude boundary layer (HLBL) (or plasma mantle), and the exterior cusp region (or entry layer). The formation and the properties of these boundary layers are complex and are still not fully understood. The entry layer and plasma mantle are generally believed to be on open magnetic field lines. They are populated by a mixture of magnetosheath plasma that entered the magnetosphere along open field lines in the cusp and ionospheric plasma that flowed up from the cusp and polar cap in an upward flow known as the"polar wind." The LLBL (*Gosling et al.*, 1990; *Fuselier et al.*, 1995; *Onsager and Scudder*, 2003) and HLBL (*Fedorov et al.*, 2001, 2003) are generally believed to be formed by magnetic reconnection.

It is well known that the magnetosphere is open under southward IMF condition. That is, there are open field lines threading the magnetopause. Since there is no reconnection at the dayside magnetopause when IMF is northward, the magnetosphere can possibly become closed and there may be no open field on the boundary (*Gombosi et al.*, 1998; *Song et al.*, 1999). However, observations (*Cowley*, 1983; *Troshichev*, 1990; *Fairfield*, 1993; *Fairfield et al.*, 1996) are too scarce to confirm a fully closed magnetosphere under prolonged northward IMF conditions. The closed magnetosphere produced in some MHD magnetosphere models for due northward IMF may be a result of error due to numerical resistivity (*Raeder*, 1999).

Of the magnetosphere boundary layers, the LLBL is the most complex layer, which

is identified as a region immediately inside the magnetopause with densities and temperatures that are intermediate between those in the neighboring magnetosheath and magnetosphere. The boundary layer outside the magnetopause is typically referred to as the magnetosheath boundary layer (MSBL) (*Cowley*, 1982). When IMF is southward, the LLBL forms directly at low latitudes, close to where reconnection is occurring. As a result of the reconnection and the subsequent evolution of the newly interconnected field lines, magnetosheath plasma originating from the solar wind and magnetospheric and ionospheric plasma are able to mix and form the LLBL and MSBL.

High-latitude reconnection has been proposed as a mechanism for the formation of the low latitude boundary layer for northward IMF conditions (e.g., *Cowley*, 1981; *Song and Russell*, 1992; *Lin and Wang*, 2006). *Fuselier et al.* [1995] suggested that the LLBL is on open field lines even when the magnetic shear across the local magnetopause is low. *Paschmann et al.* [1993] suggested that under conditions of low magnetic shear, the changes in plasma thermal and flow properties may be attributed to a transition from open interplanetary field lines to closed geomagnetic field lines. From ISEE observations, *Le et al.* [1996] concluded that there are two types of low-latitude boundary layer plasma inside the dayside magnetopause for northward interplanetary magnetic field: (1) an outer boundary layer where heated magnetosheath plasma is the dominant particle population and where the hot magnetospheric component is strongly depleted or missing; and (2) an inner boundary layer where the two components are more nearly equal. The two types of plasma characteristics can be explained by the process of magnetic reconnection poleward of the region of the cusp. They interpreted the outer boundary layer as a layer composed of open field lines that are formed by magnetic reconnection above one cusp. The inner boundary layer is composed of newly closed field lines that are formed from magnetosheath field

lines by double magnetic reconnection, first poleward of one cusp and later poleward of the other cusp.

The magnetosphere boundary layers in the tail flanks have been less explored. *Eastman and Hones* [1979] found that the LLBL in the flanks is normally on closed field lines. The particle distributions of the plasma in the low-latitude dusk flank region reported by *Phan et al.* [1997] also suggest that the LLBL is on closed field lines in that region.

Due to the lack of sufficient in-situ observations, the properties and structure of the magnetosphere boundary is not well known. Through the detailed analysis of the high-latitude reconnection in the simulation, I will present clearer picture about the magnetosphere boundary under northward IMF condition.

1.1.3 Plasma sheet

It is well known that the solar wind plasma can enter into the plasma sheet through reconnection processes first at the dayside subsolar merging site and then in the distant magnetotail, when the IMF is southward (*Dungey*, 1961; *Cowley*, 1980; *Rosenbauer et al.*, 1975; *Sckopke et al.*, 1981). The first reconnection process captures the solar wind plasma which then flows tailward into the mantle/lobe at high latitudes. The second reconnection process in the tail drives the plasma from the mantle/lobe toward the Earth. As a consequence of the reconnection process the plasma sheet is most of the time found to be consisting of hot (1-10 keV) and tenuous plasma ($\sim$0.1 cm^{-3}. It becomes denser and hotter for increasing geomagnetic activity (*Borovsky et al.*, 1998; *Wing and Newell*, 1998).

When the IMF is northward, there is no or little dayside reconnection. The plasma sheet density should therefore decrease because there is less plasma fed into it through the process described above. However, the plasma sheet often becomes denser and

colder under quiet geomagnetic conditions. At times, a very cold and dense plasma sheet is observed (e.g., *Fairfield et al.*, 1981; *Baumjohann et al.*, 1989; *Lennartsson*, 1992; *Fujimoto et al.*, 1996, 1998; *Terasawa et al.*, 1997). The ionosphere is an unlikely source of this plasma since (1) the ionospheric outflow has been found to be strongest during active times and for southward IMF (*Yau et al.*, 1985; *Øieroset et al.*, 1999), and (2) the CDPS is generally void of a cold O^+ component (e.g., *Rème et al.*, 2001). Therefore, the plasma entering the plasma sheet when the IMF is northward is believed to be primarily of solar wind origin.

The CDPS is often observed after a period when the IMF had been northward, on average, for several hours. This plasma is characterized by higher density ($\sim$1 cm^{-3}), lower temperature ($<$ 1 keV), and small flow velocity. It is found to be on closed field lines (*Fujimoto et al.*, 1998). Most of the CDPS observations are made near the Earth in the tail (*Fujimoto et al.*, 2002). Many observations show that it is located much more often near the flanks (e.g., *Fujimoto et al.*, 1996, 1998; *Phan et al.*, 1998; *Fuselier et al.*, 1999; *Øieroset et al.*, 2002) than at the center of the plasma sheet.

Most of the CDPS observations are made in the near tail($X_{GSE} >$ -30 R_E). The cold dense plasma usually does not penetrate into the near-Earth region (geosynchronous orbit) because of the very weak convection that exists during northward IMF, except the following two conditions as stated by (*Thomsen et al.*, 2003) in which a superdense plasma sheet (density up to $\sim$10 cm^{-3}) (*Borovsky et al.*, 1997) is detected by Los Alamos plasma instrument at geosynchronous orbit: (1) a sudden southward IMF turning that follows an extended interval of northward field and (2) a very strong magnetospheric compression caused by a large increase in the solar wind dynamic pressure, also under conditions of northward IMF. Under the above conditions, a plasma sheet with high density ($>$ 2.0 cm^{-3}) is often detected at the geosynchronous orbit by the Magnetospheric Plasma Analyzer (MPA) on board Los

Alamos National Laboratory (LANL) satellites (*Borovsky et al.*, 1997; *Thomsen et al.*, 2003; *Lavraud et al.*, 2005a, 2006a) .

1.1.4 Solar wind entry mechanisms

Although the geomagnetic field acts as a barrier to protect the Earth from solar wind, the magnetopause is not an impenetrable solid boundary separating the shocked solar wind plasma of the magnetosheath from the hot tenuous plasma of the magnetosphere. Plasma characteristic of magnetosheath origin has been found inside all the boundary layers adjoining magnetopause, and in the plasma sheet. Impulsive injection of magnetosheath plasma is found deep inside the Earth's dayside closed field region (*Woch and Lundin*, 1992; *Moen et al.*, 1994; *Stenuit et al.*, 2001). Northward IMF seems to be preferred for such sheath injections onto closed field lines (*Newell and Meng*, 2003). The occurrence of impulsive magnetosheath injections are found to be positively correlated with high solar wind pressure, and pressure variations (*Stenuit et al.*, 2001).

A number of processes have been proposed to account for the transfer of solar wind plasma into the magnetosphere. The solar wind plasma can enter the magnetosphere directly through the exterior cusp region where there is a magnetic null even in a closed magnetopause. The plasma is of magnetosheath characteristics, but the flows are low-speed, disordered, and probably turbulent. Under southward IMF condition, solar wind plasma can enter the magnetosphere along the open field lines through the plasma mantle and the cusp. The tail reconnection creating closed field lines from lobe field lines can also bring solar wind plasma into the plasma sheet.

Diffusion and viscous-like interaction involving finite gyroradii effect, wave-particle interaction, and turbulence have also been proposed as mechanisms for magnetosheath plasma be transferred into the magnetosphere (*Axford and Hines*, 1961; *Treumann*,

1997; *Thorne and Tsurutani*, 1991; *Tsurutani et al.*, 2003). *LeMaire* [1977] proposed that at some local weak $|B|$ location, solar wind plasma may impulsively penetrate the magnetic barrier on a local scale. However, this theory has not become widely accepted.

On the tail flanks, there is large velocity shear across the magnetopause. Such high gradient of velocity will cause the Kelvin-Helmholtz instability (KHI) to occur on the boundary and surface waves might form vortices that can mix the plasma from both sides of the magnetopause, as indicated in Figure 1-3. The magnetosheath plasma is thus mixed into the magnetosphere (*Fujimoto and Terasawa*, 1994; *Fairfield et al.*, 2000; *Nykyri and Otto*, 2001; *Nykyri et al.*, 2006; *Hasegawa et al.*, 2004). The wave length of the KH vortex is found to be as large as 8 R_E (*Hasegawa et al.*, 2004). Therefore the KHI possibly plays some role in large scale plasma transport.

Double high-latitude reconnection occurring tailward of the cusps of both hemispheres under northward IMF conditions has been proposed to be a large scale mechanism that can cause magnetosheath plasma enter the magnetosphere (*Song and Russell*, 1992; *Song et al.*, 1999; *Raeder et al.*, 1995, 1997). Double high-latitude reconnection can create new closed field lines composed of magnetosheath field and geomagnetic field and thus can bring in magnetosheath plasma into the magnetosphere.

The KHI process and double high-latitude reconnection process are believed to be the two main processes that can allow magnetosheath plasma to enter the magnetosphere in a large scale most efficiently. However, the studies of these two processes have not shown in sufficient detail how the plasma enters into the plasma sheet and what its expected properties are. The observations of the KHI process near the magnetosphere boundary are still not very few and have not been connected to plasma entry. How the roll-up vortices during the KHI process efficiently transport plasma

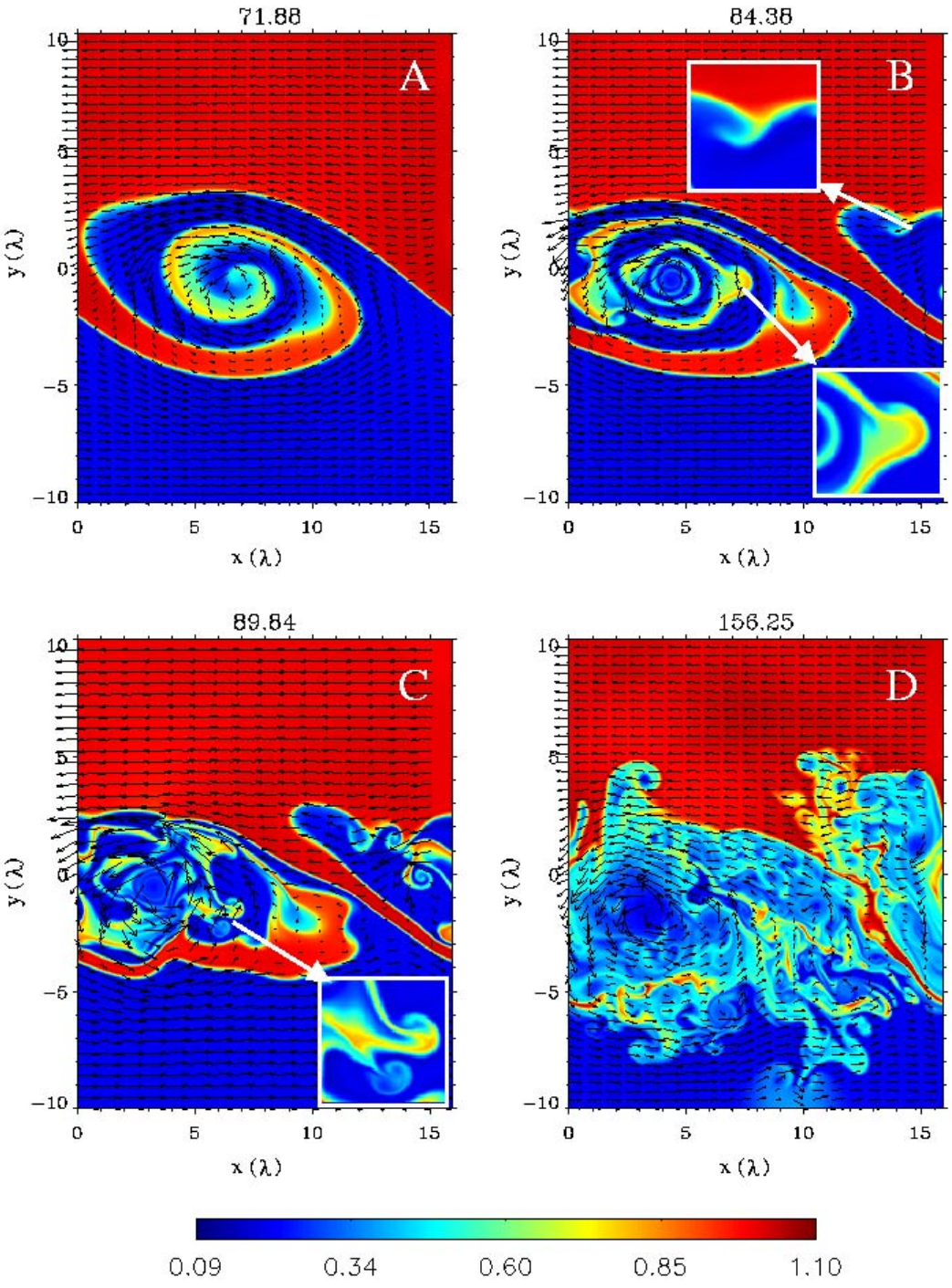

Figure 1-3: Two-dimensional MHD simulation of plasma mixing and transport due to Kelvin-Helmholtz instability (KHI). The plasma density is indicated by color. The number on each plot's title is the time stamp. (from Matsumoto)

from the magnetosheath to inside the magnetopause, and even onto closed field lines near the noon-midnight meridian, is still not clear. The double high-latitude reconnection process is believed to create newly closed field flux tubes with magnetosheath plasma in it at the dayside magnetopause. With only a few multi-spacecraft observations, how such captured magnetosheath plasma populates the magnetosphere boundary and the plasma sheet is not well known. It is not clear either how the solar wind and IMF conditions affect this process in bringing in the magnetosheath plasma into the magnetosphere, which may need a lot more observations. The advantage of the simulation study in this dissertation research is that, once an entry mechanism is established in the simulation, simulations can be further run with various geospace conditions and the physical processes can be explored in detail in the simulations.

1.1.5 Solar wind entry rate

Pilipp and Morfill [1978] estimated the solar wind entry rate of about 10^{26} to 10^{27} particles per second through the plasma mantle when the IMF is southward. *Cowley* [1980] also gave an estimation of particle influx at about 10^{27} s^{-1} through the new open field flux tube created from dayside magnetopause reconnection. *Eastman et al.* [1985] estimated that a few times 10^{26} particles per second enter the magnetosphere through the boundary layers. *Richard et al.* [1994] calculated the total entry rate to be 1.7×10^{27} particles per second using test particle calculations for northward IMF conditions. These studies also estimated that a particle entry rate of 10^{27} s^{-1} is sufficient to fill and to maintain the plasma sheet.

1.2 The Research in This Dissertation

In this study, I not only analyze observational data, but also use the MHD magnetosphere model OpenGGCM as a tool to study the phenomenon of solar wind and

magnetosphere interaction under northward IMF conditions. The advantage of using MHD simulation in this study is that I can explore the properties of the outer magnetosphere globally in much more detail than using scarce observations in space. Once the simulation reproduces the observations of an event, I will be able to find out the mechanism behind it.

In chapter 2, I introduce MHD model for the magnetosphere and the MHD equations used in OpenGGCM. I then introduce the basics of OpenGGCM including the simulation domain, numerical grid, boundary and initial conditions, and simulation algorithm.

As a fundamental approach, I first perform event studies to validate the model used in this study. Two cold dense plasma sheet events and a superdense plasma sheet event (SDPS) are selected to perform simulations using OpenGGCM. The simulation results are then compared to the observations, and are used to analyze the solar wind entry process. After validating the model, parametric studies are then performed to study in detail the entry mechanism and the dependence of the plasma entry rate on solar wind, IMF and geomagnetic dipole conditions.

In this dissertation study, I establish that the OpenGGCM reproduces the formation of the CDPS, and that the simulation results match the observations extremely well. I also show that OpenGGCM also reproduces the superdense plasma sheet, and that the simulation results match the observations.

Starting from the CDPS simulation results, I show along which paths the solar wind plasma enters the magnetosphere and forms the CDPS. Further more, I show the detailed process by which the superdense plasma sheet forms near the geosynchronous orbit, initiated by the southward IMF turning after a previous long period of northward IMF.

I follow up by running simulations for a parametric study using selected solar

wind conditions and generic parameters similar to the ones used in the CDPS event studies. Using these simulation results, I compute the paths of fluid elements from the solar wind, and the magnetic field lines threading the fluid element at each calculation step. I derive the topological properties of the magnetic field lines near the magnetopause, and the behavior of high-latitude reconnection. I examine in detail how the magnetosheath plasma is captured by double high-latitude reconnection and convected to the tail flanks and into the plasma sheet. I construct entry windows through which the solar wind plasma enters the magnetosphere as a result of double high-latitude reconnection. How and why the solar wind, IMF and geomagnetic dipole parameters affect the entry window is then been explored in more detail. With the entry window, I then estimate the solar wind plasma entry rate for various solar wind and IMF conditions.

During this dissertation study, the study of the CDPS event presented in Chapter 3 has been published on Geophysical Research Letters (*Li et al.*, 2005), and the study of the solar wind entry mechanism and entry rate presented in Chapter 5 and Chapter 6 also has been submitted to Journal of Geophysical Research (*Li et al.*, 2007).

CHAPTER 2

MHD THEORY AND GLOBAL MHD MODEL

2.1 Introduction

Magnetohydrodynamic theory is widely used in studying magnetized plasma systems in the universe. The simulation model used in this study is MHD theory applied to the magnetosphere and the solar wind around it. MHD theory has long been established to describe macroscopic properties of magnetized plasma system (*Cravens*, 1997; *Parks*, 2004; *Priest and Forbes*, 2006; *Gurnett and Bhattacharjee*, 2005). I will give a detailed derivation of the equations here, and will discuss the limitations of MHD theory in the applications. I will then introduce the computation grid, boundary and initial conditions, and numerical algorithm in the OpenGGCM model used in this dissertation study.

2.2 MHD Theory for the Magnetosphere

In the solar wind near the Earth's orbit, average values of the solar wind plasma parameters are $\sim$6.6 cm^{-3} for plasma density , $\sim$10 m for the Debye Length, $\sim$80 km for the proton gyroradius, $\sim$4 $\times 10^6$ s for the proton-proton collision time, and $\sim$3 $\times 10^5$ s for the electron-electron collision time (*Kivelson and Russell*, 1995). In the magnetosphere, the conditions vary for different regions. In the outer magnetosphere

regions (plasma sheet, plasma sheet boundary layer, tail lobes, magnetopause), the plasma density is usually lower than that in the solar wind. For the regions in the solar wind and in the outer magnetosphere, the plasma can be considered to be collisionless. Thus, the system of solar wind and outer magnetosphere can be modeled as a plasma system in which: (1) there are only protons and electrons, (2) gravitation is neglected, (3) the plasma is collisionless, and (4) the speed of particles is much less than light speed.

A particle ensemble can be described by the distribution functions for each particle species. A distribution function $f_s(t, \mathbf{r}, \mathbf{v})$ is defined on a six-dimensional phase space $(\mathbf{r}, \mathbf{v})$, as the number of type s particles per unit volume of phase space ($dV = d\mathbf{r}d\mathbf{v}$), centered at a point in phase space:

$$\begin{aligned} \text{number of type } s \text{ particles in } dV &= f_s(t, \mathbf{r}, \mathbf{v}) d^3\mathbf{r} d^3\mathbf{v} \\ &= f_s(t, x, y, z, v_x, v_y, v_z) dx dy dz dv_x dv_y dv_z. \end{aligned} \tag{2.1}$$

The total time derivative of $f_s(t, \mathbf{r}, \mathbf{v})$ is

$$\begin{aligned} \frac{df_s}{dt} = \frac{\partial f_s}{\partial t} + \frac{\partial f_s}{\partial x}\frac{dx}{dt} + \frac{\partial f_s}{\partial y}\frac{dy}{dt} + \frac{\partial f_s}{\partial z}\frac{dz}{dt} + \frac{\partial f_s}{\partial v_x}\frac{dv_x}{dt} + \frac{\partial f_s}{\partial v_y}\frac{dv_y}{dt} + \frac{\partial f_s}{\partial v_z}\frac{dv_z}{dt} \\ = \frac{\partial f_s}{\partial t} + \mathbf{v} \cdot \nabla f_s + \mathbf{a} \cdot \nabla_v f_s. \end{aligned} \tag{2.2}$$

In the absence of collisions, the total time derivative of the phase space distribution function is zero. Thus, the system of solar wind and outer magnetosphere can be described by the Vlasov equation:

$$\frac{df_s}{dt} = \frac{\partial f_s}{\partial t} + \mathbf{v} \cdot \nabla f_s + \mathbf{a} \cdot \nabla_v f_s = 0. \tag{2.3}$$

Here $\mathbf{a}$ is the acceleration of a particle of type s, located at position $\mathbf{r}$ with velocity $\mathbf{v}$. The acceleration of a particle in a plasma is the effect of noncollisional forces including gravity and the Lorentz force. Neglecting gravity in our system, $\mathbf{a}$ is given

by the electromagnetic force

$$\mathbf{a}(t, \mathbf{r}, \mathbf{v}) = \frac{q_s}{m_s}[\mathbf{E}(t, \mathbf{r}) + \mathbf{v} \times \mathbf{B}(t, \mathbf{r})], \tag{2.4}$$

where $\mathbf{E}$ and $\mathbf{B}$ can be found using Maxwell's equations. Here $\mathbf{E}$ and $\mathbf{B}$ are macroscopic fields that do not include the microscopic fields associated with discrete particle collisions. Substituting 2.4 into 2.3, the Vlasov equation reads:

$$\frac{df_s}{dt} = \frac{\partial f_s}{\partial t} + \mathbf{v} \cdot \nabla f_s + \frac{q_s}{m_s}(\mathbf{E} + \mathbf{v} \times \mathbf{B}) \cdot \nabla_v f_s = 0. \tag{2.5}$$

The phase space distribution function is a description of the particle ensemble. Although the concept of infinitely small volume and time is used in definition and derivative of the distribution function, the time and space scale of a studied system and process should be much greater than the characteristic microscales such as the ion gyroradius, Debye length, and ion gyroperiod.

The macroscopic variables of the plasma system can be constructed from the phase space distribution function by taking moments. The n^{th} moment of the distribution function is defined by

$$M^n(f_s) = \int \mathbf{v}^n f_s d^3\mathbf{v}, \tag{2.6}$$

where $\mathbf{v}^n$ is the n^{th} tensor.

The number density is just the 0^{th} moment:

$$n_s(t, \mathbf{r}) = \int f_s d^3\mathbf{v}. \tag{2.7}$$

The particle flux of species s is the first moment:

$$\chi(t, \mathbf{r}) = \int \mathbf{v} f_s d^3\mathbf{v}. \tag{2.8}$$

The bulk flow velocity is the average velocity defined as

$$\mathbf{u}(t, \mathbf{r}) = \frac{\chi(t, \mathbf{r})}{n_s} = \frac{1}{n_s} \int \mathbf{v} f_s d^3\mathbf{v}. \tag{2.9}$$

The second moment is related to the pressure tensor, which is the flux of momentum relative to the frame moving with the plasma flow:

$$\tilde{P}_s(t,\mathbf{r}) = m_s \int (\mathbf{v}-\mathbf{u})(\mathbf{v}-\mathbf{u}) f_s d^3\mathbf{v}. \tag{2.10}$$

A scalar pressure p_s is defied as one third of the trace of $\tilde{P}_s$:

$$p_s = \frac{1}{3}\sum_{j=1}^{3} P_{sjj} \tag{2.11}$$

The third moment of the distribution function is related to heat flux which is the flux of internal kinetic energy of the plasma system:

$$Q_s(t,\mathbf{r}) = \frac{1}{2} m_s \int (v-u)^2 (\mathbf{v}-\mathbf{u}) f_s d^3\mathbf{v}. \tag{2.12}$$

Some other macroscopic variables of interest are mass density ρ_s, density of electric charge ρ_{qs}, density of electric current $\mathbf{J}_s$, and internal kinetic energy ε defined as follows:

$$\rho_s = m_s n_s,\ \rho = \sum_s \rho_s; \tag{2.13}$$

$$\rho_{qs} = q_s n_s,\ \rho_q = \sum_s \rho_{qs}; \tag{2.14}$$

$$\mathbf{J}_s = q_s n_s u_s,\ \mathbf{J} = \sum_s \mathbf{J}_s; \tag{2.15}$$

$$\varepsilon = \int \frac{1}{2} m_s (v-u)^2 f_s d^3\mathbf{v}. \tag{2.16}$$

With the Vlasov equation (2.5) and the macroscopic variables derived from moments of the phase space distribution function, I now construct the macroscopic equations.

Integrating equation (2.5) over the velocity gives:

$$\int \frac{\partial f_s}{\partial t} d^3\mathbf{v} + \int \mathbf{v}\cdot\nabla f_s d^3\mathbf{v} + \frac{q_s}{m_s}\int (\mathbf{E}+\mathbf{v}\times\mathbf{B})\cdot\nabla_v f_s d^3\mathbf{v} = 0. \tag{2.17}$$

The first term is

$$\int \frac{\partial f_s}{\partial t} d^3\mathbf{v} = \frac{\partial}{\partial t}\int f_s d^3\mathbf{v} = \frac{\partial n_s}{\partial t}. \tag{2.18}$$

The second term is

$$\int \mathbf{v}\cdot\nabla f_s d^3\mathbf{v} = \nabla\cdot\int \mathbf{v} f_s d^3\mathbf{v} - \int f_s \nabla\cdot\mathbf{v} d^3\mathbf{v} = \nabla\cdot(n\mathbf{u}) \tag{2.19}$$

where the vector identity $\nabla\cdot f\mathbf{v} = (\mathbf{v}\cdot\nabla)f + f\nabla\cdot\mathbf{v}$, and $\nabla\cdot\mathbf{v} = 0$ are used. The third term is

$$\begin{aligned}
&\frac{q_s}{m_s}\int(\mathbf{E}+\mathbf{v}\times\mathbf{B})\cdot\nabla_v f_s d^3\mathbf{v} \\
&= \frac{q_s}{m_s}\int \nabla_v\cdot(f(\mathbf{E}+\mathbf{v}\times\mathbf{B}))d^3\mathbf{v} - \frac{q_s}{m_s}\int f_s\nabla_v\cdot(\mathbf{E}+\mathbf{v}\times\mathbf{B})d^3\mathbf{v} \\
&= \frac{q_s}{m_s}\oint f_s(\mathbf{E}+\mathbf{v}\times\mathbf{B})\cdot d\mathbf{S} - \frac{q_s}{m_s}\int f_s\nabla_v\cdot(\mathbf{E}+\mathbf{v}\times\mathbf{B})d^3\mathbf{v} = 0
\end{aligned} \tag{2.20}$$

Here we assume that $\lim_{v\to\infty} f_s = 0$, which is necessary for the plasma to have finite energy density. Thus the integral over the infinite surface in the third line of (2.20) vanishes. Since $\mathbf{E}$ and $\mathbf{B}$ do not depend on v, then $\nabla_v\cdot\mathbf{E} = 0$ and $\nabla_v\cdot(\mathbf{v}\times\mathbf{B}) = 0$.

Equation (2.17) then becomes

$$\frac{\partial n_s}{\partial t} + \nabla\cdot(n_s\mathbf{u}_s) = 0 \tag{2.21}$$

which is called the continuity equation. Multiplying (2.21) with m_s, we obtain the mass conservation equation

$$\frac{\partial \rho_s}{\partial t} + \nabla\cdot(\rho_s\mathbf{u}_s) = 0 \tag{2.22}$$

Now let we determine the first moment of the Vlasov equation by multiplying (2.5) by $\mathbf{v}$ and integrating it over the velocity space. This is the momentum equation, which is a vector equation with three components. The first term is

$$\int \mathbf{v}\frac{\partial f_s}{\partial t} d^3\mathbf{v} = \frac{\partial}{\partial t}\int \mathbf{v} f_s d^3\mathbf{v} = \frac{\partial}{\partial t}(n_s\mathbf{u}_s). \tag{2.23}$$

where (2.9) is used. The second term is

$$\begin{aligned}
&\int \mathbf{v}(\mathbf{v}\cdot\nabla f_s)d^3\mathbf{v} = \nabla\cdot\int \mathbf{v}\mathbf{v} f_s d^3\mathbf{v} \\
&= \nabla\cdot[\int(\mathbf{v}-\mathbf{u}_s)(\mathbf{v}-\mathbf{u}_s)f_s d^3\mathbf{v} + \int(\mathbf{v}\mathbf{u}_s + \mathbf{u}_s\mathbf{v} - \mathbf{u}_s\mathbf{u}_s)f_s d^3\mathbf{v}] \\
&= \nabla\cdot(\frac{\tilde{P}_s}{m_s} + n_s\mathbf{u}_s\mathbf{u}_s),
\end{aligned} \tag{2.24}$$

where the equations (2.7), (2.9), and (2.10) are used. The third term is

$$\int \frac{q_s}{m_s}\mathbf{v}(\mathbf{E}+\mathbf{v}\times\mathbf{B})\cdot\nabla_v f_s d^3\mathbf{v}$$
$$= \frac{q_s}{m_s}[\int(\mathbf{vE})\cdot\nabla_v f_s d^3\mathbf{v} + \int(\mathbf{vv}\times\mathbf{B})\cdot\nabla_v f_s d^3\mathbf{v}]. \tag{2.25}$$

Each term of equation (2.25) can be simplyfied to:

$$\int(\mathbf{vE})\cdot\nabla_v f_s d^3\mathbf{v} = \int\nabla_v\cdot(\mathbf{vE}f_s)d^3\mathbf{v} - \int f_s\nabla_v\cdot(\mathbf{vE})d^3\mathbf{v}$$
$$= 0 - \int f_s\mathbf{E}d^3\mathbf{v} = -\mathbf{E}\int f_s d^3\mathbf{v} = -n_s\mathbf{E}, \tag{2.26}$$

and

$$\int(\mathbf{vv}\times\mathbf{B})\cdot\nabla_v f_s d^3\mathbf{v} = \int\nabla_v\cdot(f_s\mathbf{vv}\times\mathbf{B})d^3\mathbf{v} - \int f_s\nabla_v\cdot(\mathbf{vv}\times\mathbf{B})d^3\mathbf{v}$$
$$= 0 - \int f_s\mathbf{v}\times\mathbf{B}d^3\mathbf{v} = -(\int f_s\mathbf{v}d^3\mathbf{v})\times\mathbf{B} = -n_s\mathbf{u}_s\times\mathbf{B}, \tag{2.27}$$

where the fact that $\mathbf{E}$ and $\mathbf{B}$ are independent of $\mathbf{v}$, and the surface integrals at infinity are used:

$$\int\nabla_v\cdot(\mathbf{vE}f_s)d^3\mathbf{v} = \oint(\mathbf{vE}f_s)\cdot d\mathbf{S} = 0, \tag{2.28}$$
$$\int\nabla_v\cdot(f_s\mathbf{vv}\times\mathbf{B})d^3\mathbf{v} = \oint(f_s\mathbf{vv}\times\mathbf{B})\cdot d\mathbf{S} = 0. \tag{2.29}$$

Equation 2.29 requires that $\lim_{v\to\infty} v^2 f_s = 0$, i.e., f_s falls off faster than v^2. Equation (2.25) then becomes:

$$\int\frac{q_s}{m_s}\mathbf{v}(\mathbf{E}+\mathbf{v}\times\mathbf{B})\cdot\nabla_v f_s d^3\mathbf{v} = -\frac{n_s q_s}{m_s}(\mathbf{E}+\mathbf{u}_s\times\mathbf{B}). \tag{2.30}$$

Putting (2.23), (2.24), and (2.30) together gives the equation for conservation of the momentum:

$$\frac{\partial}{\partial t}(n_s\mathbf{u}_s) + \nabla\cdot(\frac{\tilde{P}_s}{m_s} + n_s\mathbf{u}_s\mathbf{u}_s) - \frac{n_s q_s}{m_s}(\mathbf{E}+\mathbf{u}_s\times\mathbf{B}) = 0. \tag{2.31}$$

The (i,j) component of the pressure tensor is given by

$$P_{sij}(t,\mathbf{r}) = m_s\int(\mathbf{v}-\mathbf{u}_s)_i(\mathbf{v}-\mathbf{u}_s)_j f_s(t,\mathbf{r},\mathbf{v})d^3\mathbf{v}. \tag{2.32}$$

Let $\mathbf{w} = \mathbf{v} - \mathbf{u}_s$, then

$$P_{sij}(t, \mathbf{r}) = m_s \int w_i w_j f_s(t, \mathbf{r}, \mathbf{w}) d^3\mathbf{w}. \tag{2.33}$$

In the pressure tensor, the off-diagonal elements represent the shear stresses. These stresses severely complicate the equation. For a distribution function that is axis-symmetric , i.e.,

$$f_s(\mathbf{v} - \mathbf{u}_s) = f_s(\mathbf{v} + \mathbf{u}_s), \tag{2.34}$$

the off-diagonal terms of P_s vanish. Further more, if f_s is spherical symmetric in velocity space with $\mathbf{u}_s$ as the center, i.e.,

$$f_s(\mathbf{v} - \mathbf{u}_s) = f_s(|\mathbf{v} - \mathbf{u}_s|), \tag{2.35}$$

then the diagonal terms are all given by

$$p_s(t, \mathbf{r}) = \frac{1}{3} m_s \int w^2 f_s(t, \mathbf{r}, w) d^3\mathbf{w}, \tag{2.36}$$

and the pressure tensor can be written as

$$\tilde{P}_s = p_s \mathbf{I}, \tag{2.37}$$

where $\mathbf{I}$ is the unit tensor. The momentum conservation equation (2.31) then simplifies to

$$\frac{\partial}{\partial t}(n_s \mathbf{u}_s) + \nabla \cdot (\frac{p_s \mathbf{I}}{m_s} + n_s \mathbf{u}_s \mathbf{u}_s) - \frac{n_s q_s}{m_s}(\mathbf{E} + \mathbf{u}_s \times \mathbf{B}) = 0. \tag{2.38}$$

or

$$\frac{\partial}{\partial t}(\rho_s \mathbf{u}_s) + \nabla \cdot (p_s \mathbf{I} + \rho_s \mathbf{u}_s \mathbf{u}_s) - \rho_{qs} \mathbf{E} - \mathbf{J}_s \times \mathbf{B} = 0. \tag{2.39}$$

The Maxwellian distribution function and kappa distribution function are the two common distribution function used in models. Both functions have spherical symmetry. In large parts of the solar wind and outer magnetosphere, the $f_s(\mathbf{v} - \mathbf{u}_s) = f_s(|\mathbf{v} - \mathbf{u}_s|)$ assumption are well satisfied. However, the violations of spherical

symmetry can be significant in the ring current, in regions of strong diffusion, and possibly in the plasma sheet.

Now I construct the energy conservation equation from the second velocity moment of equation (2.5). Multiplying equation (2.5) by $\mathbf{vv}$ and integrating it over the velocity gives an equation for second rank pressure tensor:

$$\int \frac{\partial f_s}{\partial t}\mathbf{vv}d^3\mathbf{v}+\int(\mathbf{v}\cdot\nabla f_s)\mathbf{vv}d^3\mathbf{v}+\frac{q_s}{m_s}\int(\mathbf{E}\cdot\nabla_v f_s)\mathbf{vv}d^3\mathbf{v}+\frac{q_s}{m_s}\int[(\mathbf{v}\times\mathbf{B})\cdot\nabla_v f_s]\mathbf{vv}d^3\mathbf{v}=0. \tag{2.40}$$

The first term is

$$\begin{aligned}\int \frac{\partial f_s}{\partial t}\mathbf{vv}d^3\mathbf{v} &= \frac{\partial}{\partial t}\int f_s\mathbf{vv}d^3\mathbf{v}-\int f_s\frac{\partial}{\partial t}(\mathbf{vv})d^3\mathbf{v}\\ &= \frac{\partial}{\partial t}\int f_s\mathbf{vv}d^3\mathbf{v}-0\\ &= \frac{\partial}{\partial t}\left[\int f_s(\mathbf{v}-\mathbf{u}_s)(\mathbf{v}-\mathbf{u}_s)d^3\mathbf{v}+\int f_s(\mathbf{vu}+\mathbf{uv}-\mathbf{uu})d^3\mathbf{v}\right]\\ &= \frac{\partial}{\partial t}(\frac{\tilde{P}_s}{m_s}+n_s\mathbf{u}_s\mathbf{u}_s)\end{aligned} \tag{2.41}$$

where the definitions of $\tilde{P}_s$ and $\mathbf{u}_s$ are used, and the term $\int f_s\frac{\partial}{\partial t}(\mathbf{vv})d^3\mathbf{v}$ vanishes since t and $\mathbf{v}$ are independent variables. In the approximation used here for the magnetosphere, the pressure tensor $\tilde{P}_s$ is reduced to $p_s\mathbf{I}$, where only diagonal components exist, and these components are equal. Since the sum of all the terms in equation (2.40) is zero, we may only consider the diagonal components of the tensors in this equation. Therefore, in working with the other terms of (2.40), I may just sum over the diagonal components of each term. In other words, I take the trace of all the terms of equation (2.40).

Using (2.36) and (2.16), the trace of the first term is

$$\frac{\partial}{\partial t}(\frac{3p_s}{m_s}+n_su_s^2)=\frac{\partial}{\partial t}(\frac{2\varepsilon_s}{m_s}+n_su_s^2) \tag{2.42}$$

Since $\mathbf{r}$ and $\mathbf{v}$ are independent variables, the second term of (2.40) becomes

$$\int\mathbf{v}\cdot\nabla f_s\mathbf{vv}d^3\mathbf{v}=\nabla\cdot\int\mathbf{vvv}f_sd^3\mathbf{v}. \tag{2.43}$$

The term $\int \mathbf{vvv} f_s d^3\mathbf{v}$ can be expanded as

$$\begin{aligned}\int \mathbf{vvv} f_s d^3\mathbf{v} = &\int (\mathbf{v}-\mathbf{u}_s)(\mathbf{v}-\mathbf{u}_s)(\mathbf{v}-\mathbf{u}_s) f_s d^3\mathbf{v} + \int \mathbf{v}\mathbf{u}_s\mathbf{v} f_s d^3\mathbf{v} \\ &+ \int \mathbf{u}_s\mathbf{v}\mathbf{v} f_s d^3\mathbf{v} - \int \mathbf{u}_s\mathbf{u}_s\mathbf{v} f_s d^3\mathbf{v} + \int \mathbf{v}\mathbf{v}\mathbf{u}_s f_s d^3\mathbf{v} \\ &- \int \mathbf{v}\mathbf{u}_s\mathbf{u}_s f_s d^3\mathbf{v} - \int \mathbf{u}_s\mathbf{v}\mathbf{u}_s d^3\mathbf{v} + \int \mathbf{u}_s\mathbf{u}_s\mathbf{u}_s f_s d^3\mathbf{v}. \end{aligned} \tag{2.44}$$

The sum of the diagonal terms of 2.44 is:

$$\begin{aligned}\sum_{i=x,y,z} \int v_i^2 \mathbf{v} f_s d^3\mathbf{v} = &\sum_{i=x,y,z} \int [(v_i - u_{si})^2 (\mathbf{v}-\mathbf{u}_s)] f_s d^3\mathbf{v} + \sum_{i=x,y,z} \int v_i u_{si} \mathbf{v} f_s d^3\mathbf{v} \\ &+ \sum_{i=x,y,z} \int u_{si} v_i \mathbf{v} f_s d^3\mathbf{v} - \sum_{i=x,y,z} \int u_{si} u_{si} \mathbf{v} f_s d^3\mathbf{v} \\ &+ \sum_{i=x,y,z} \int v_i v_i \mathbf{u}_s f_s d^3\mathbf{v} - \sum_{i=x,y,z} \int v_i u_{si} \mathbf{u}_s f_s d^3\mathbf{v} \\ &- \sum_{i=x,y,z} \int u_{si} v_i \mathbf{u}_s f_s d^3\mathbf{v} + \sum_{i=x,y,z} \int u_{si} u_{si} \mathbf{u}_s f_s d^3\mathbf{v} \\ = &\sum_{i=x,y,z} \int [(v_i - u_{si})^2 (\mathbf{v}-\mathbf{u}_s)] f_s d^3\mathbf{v} + \sum_{i=x,y,z} \int 2 v_i u_{si} \mathbf{v} f_s d^3\mathbf{v} \\ &- \sum_{i=x,y,z} \int u_{si}^2 \mathbf{v} f_s d^3\mathbf{v} + \sum_{i=x,y,z} \int v_i^2 \mathbf{u}_s f_s d^3\mathbf{v} \\ &- \sum_{i=x,y,z} \int 2 u_{si} v_i \mathbf{u}_s f_s d^3\mathbf{v} + \sum_{i=x,y,z} \int u_{si}^2 \mathbf{u}_s f_s d^3\mathbf{v} \\ = &\int [(v-u_s)^2 (\mathbf{v}-\mathbf{u}_s)] f_s d^3\mathbf{v} + \int 2(\mathbf{v}\cdot\mathbf{u}_s)\mathbf{v} f_s d^3\mathbf{v} \\ &- \int u_s^2 \mathbf{v} f_s d^3\mathbf{v} + \int (\mathbf{v}\cdot\mathbf{v})\mathbf{u}_s f_s d^3\mathbf{v} \\ &- \int 2(\mathbf{v}\cdot\mathbf{u}_s)\mathbf{u}_s f_s d^3\mathbf{v} + \int \mathbf{u}_s^2 \mathbf{u}_s f_s d^3\mathbf{v} \\ = &\int [(v-u_s)^2 (\mathbf{v}-\mathbf{u}_s] f_s d^3\mathbf{v} + 2\mathbf{u}_s \cdot (\int \mathbf{vv} f_s d^3\mathbf{v}) \\ &- u_s^2 \int \mathbf{v} f_s d^3\mathbf{v} + \int [(\mathbf{v}-\mathbf{u}_s)\cdot(\mathbf{v}-\mathbf{u}_s)] \mathbf{u}_s f_s d^3\mathbf{v} \\ = &\frac{2}{m_s} Q_s + 2\mathbf{u}_s \cdot (\frac{\tilde{P}_s}{m_s} + n_s \mathbf{u}_s \mathbf{u}_s) - n_s u_s^2 \mathbf{u}_s + \frac{2}{m_s} e \mathbf{u}_s \\ = &\frac{2}{m_s} Q_s + 2\mathbf{u}_s \cdot \frac{\tilde{P}_s}{m_s} + n_s u_s^2 \mathbf{u}_s + \frac{2}{m_s} e_s \mathbf{u}_s \end{aligned} \tag{2.45}$$

Assuming a spherical symmetric phase space distribution function, the heat flux vector vanishes, i.e.,

$$Q_s(t,\mathbf{r}) = \frac{1}{2} m_s \int (v-u_s)^2 (\mathbf{v}-\mathbf{u}_s) f_s d^3\mathbf{v} = 0. \tag{2.46}$$

and

$$\tilde{P}_s = p_s\mathbf{I}, \text{ and } \mathbf{u}_s \cdot (p_s\mathbf{I}) = p_s\mathbf{u}_s. \tag{2.47}$$

Equation (2.45) then further simplifies to $(\frac{5p_s}{m_s} + n_s u_s^2)\mathbf{u}_s$, where $2\varepsilon_s = 3p_s$ is used. Thus, the trace of the second term of (2.40) becomes

$$\int \mathbf{v} \cdot \nabla f_s \mathbf{v}\mathbf{v} d^3\mathbf{v} = \nabla \cdot [(\frac{5}{m_s} p_s + n_s u_s^2)\mathbf{u}_s]. \tag{2.48}$$

The trace of the third term of (2.40) gives:

$$\begin{aligned}
\frac{q_s}{m_s} \sum_{i=x,y,z} \int v_i^2 \mathbf{E} \cdot \nabla_v f_s d^3\mathbf{v} &= \frac{q_s}{m_s} \int v^2 \mathbf{E}(t,\mathbf{r}) \cdot \nabla_v f_s d^3\mathbf{v} \\
&= \frac{q_s}{m_s}[\int \nabla \cdot (v^2 \mathbf{E} f_s) d^3\mathbf{v} - \int f_s \nabla \cdot (v^2\mathbf{E}) d^3\mathbf{v}] \\
&= \frac{q_s}{m_s}[\oint_{-\infty}^{\infty} (v^2\mathbf{E}) \cdot d\mathbf{S} - \int f_s \nabla \cdot (v^2\mathbf{E}) d^3\mathbf{v}] \\
= \frac{q_s}{m_s}[0 - 2\int f_s \mathbf{v} \cdot \mathbf{E} d^3\mathbf{v}] = -2\frac{q_s}{m_s}(\int \mathbf{v} f_s d^3\mathbf{v}) \cdot \mathbf{E} &= -2\frac{q_s}{m_s} n_s \mathbf{u}_s \cdot \mathbf{E} \\
&= -\frac{2}{m_s}\mathbf{J}_s \cdot \mathbf{E}.
\end{aligned} \tag{2.49}$$

Here I assume again that f_s decrease faster than $\frac{1}{v^2}$ in the limit of $v \to \infty$, which is satisfied for Maxwellian and kappa distribution function, and necessary for a plasma of finite energy density.

The trace of the fourth term of (2.40) gives:

$$\begin{aligned}
&\frac{q_s}{m_s} \sum_{i=x,y,z} \int v_i^2 (\mathbf{v} \times \mathbf{B}) \cdot \nabla_v f_s d^3\mathbf{v} \\
= \frac{q_s}{m_s}[\oint_{-\infty}^{\infty} (v^2 \mathbf{v} \times \mathbf{B} f_s) \cdot d\mathbf{S} - \int f_s \nabla_v \cdot (v^2 \mathbf{v} \times \mathbf{B}) d^3\mathbf{v}] \\
= 0 - \frac{q_s}{m_s} \int f_s [(\nabla_v v^2) \cdot (\mathbf{v} \times \mathbf{B}) + v^2 \nabla_v \cdot (\mathbf{v} \times \mathbf{B})] d^3\mathbf{v} \\
= -\frac{q_s}{m_s} \int f_s [2\mathbf{v} \cdot (\mathbf{v} \times \mathbf{B}) + v^2 \nabla_v \cdot (\mathbf{v} \times \mathbf{B})] d^3\mathbf{v} \\
= -\frac{q_s}{m_s} \int f_s [0 + 0] d^3\mathbf{v} = 0.
\end{aligned} \tag{2.50}$$

By combinning the previous results, the trace of equation (2.40) leads to the scalar energy conservation equation:

$$\frac{\partial}{\partial t}(\frac{3p_s}{m_s} + n_s u_s^2) + \nabla \cdot [(\frac{5}{m_s} p_s + n_s u_s^2)\mathbf{u}_s] - \frac{2}{m_s}\mathbf{J}_s \cdot \mathbf{E} = 0, \tag{2.51}$$

or

$$\frac{\partial}{\partial t}(\frac{3p_s}{2}+\frac{1}{2}\rho_s u_s^2)+\nabla\cdot[(\frac{5}{2}p_s+\frac{1}{2}\rho_s u_s^2)\mathbf{u}_s]-\mathbf{J}_s\cdot\mathbf{E}=0. \tag{2.52}$$

So far, the conservation equations for mass, momentum and energy are separate equations for protons and electrons. Combining them leads to a set of one-fluid conservation equations for the plasma. Substituting species s with p and e, I define the total mass density ρ, total pressure p, total density of electric charge ρ_q, total current density $\mathbf{J}$, and bulk flow velocity $\mathbf{u}$:

$$\begin{aligned}\rho=\rho_p+\rho_e,\ p=p_p+p_e,\\ n_p=n_e,\ \rho_q=n_pe-n_ee=0,\\ \mathbf{J}=\mathbf{J}_p+\mathbf{J}_e,\ m_e\ll m_p,\\ \text{and }\mathbf{u}=\frac{\rho_p\mathbf{u}_p+\rho_e\mathbf{u}_e}{\rho}.\end{aligned} \tag{2.53}$$

The one-fluid mass conservation equation is constructed by summing up the e and p contributions:

$$\frac{\partial}{\partial t}(\rho_p+\rho_e)+\nabla\cdot(\rho_p\mathbf{u}_p+\rho_e\mathbf{u}_e)=0. \tag{2.54}$$

It then becomes:

$$\frac{\partial\rho}{\partial t}+\nabla\cdot(\rho\mathbf{u})=0. \tag{2.55}$$

The one-fluid momentum conservation equation becomes:

$$\begin{aligned}\frac{\partial}{\partial t}(\rho_p\mathbf{u}_p)+\nabla\cdot(p_p\mathbf{I}+\rho_p\mathbf{u}_p\mathbf{u}_p)-\rho_{qp}\mathbf{E}-\mathbf{J}_p\times\mathbf{B}\\ +\frac{\partial}{\partial t}(\rho_e\mathbf{u}_e)+\nabla\cdot(p_e\mathbf{I}+\rho_e\mathbf{u}_e\mathbf{u}_e)-\rho_{qe}\mathbf{E}-\mathbf{J}_e\times\mathbf{B}=0,\end{aligned} \tag{2.56}$$

or

$$\frac{\partial(\rho\mathbf{u})}{\partial t}+\nabla\cdot(p\mathbf{I}+\rho\mathbf{u}\mathbf{u})-\rho_q\mathbf{E}-\mathbf{J}\times\mathbf{B}=0, \tag{2.57}$$

where the term $\rho_e\mathbf{u}_e\mathbf{u}_e$ is dropped since the electron mass density is much lower than the proton mass density, i.e., $\rho_e\ll\rho_p$.

Also dropping $\rho_e u_e^2 \mathbf{u}_e$ for the same reason, the one-fluid energy conservation equation is

$$\frac{\partial}{\partial t}(\frac{3p}{2} + \frac{1}{2}\rho u^2) + \nabla \cdot [(\frac{5}{2}p + \frac{1}{2}\rho u^2)\mathbf{u}] - \mathbf{J} \cdot \mathbf{E} = 0. \tag{2.58}$$

These equations need to be complemented by the Maxwell's equations for the fields:

$$\nabla \cdot \mathbf{E} = \frac{\rho_q}{\varepsilon_0}, \tag{2.59}$$

$$\nabla \cdot \mathbf{B} = 0, \tag{2.60}$$

$$\nabla \times \mathbf{E} = -\frac{\partial B}{\partial t}, \tag{2.61}$$

$$\nabla \times \mathbf{B} = \mu_0 \epsilon_0 \frac{\partial \mathbf{E}}{\partial t} + \mu_0 \mathbf{J}. \tag{2.62}$$

Since (2.59) and (2.60) do not relate $\mathbf{E}$ or $\mathbf{B}$ to other variables, we have now only 13 equations for 14 scalar variables. To complete the set of equations for the plasma system, we need one more equation. The generalized Ohm's law that relates $\mathbf{E}$ with other variables can be used to complete the equations, and will be developed in the following.

In deriving the momentum equation (2.39), I used the Vlasov equation (2.5), which assumes that the plasma is collisionless. Considering collisions, the Vlasov equation is replaced by the Boltzmann's equation:

$$\frac{\partial f_s}{\partial t} + \mathbf{v} \cdot \nabla f_s + \frac{q_s}{m_s}(\mathbf{E} + \mathbf{v} \times \mathbf{B}) \cdot \nabla_v f_s = (\frac{\delta f_s}{\delta t})_{collision}. \tag{2.63}$$

i.e., a collision term is added to the right hand side of (2.5).

Here I consider only the proton-electron collisions and the quasi-neutral condition in the momentum conservation equation by adding a collision term at the right hand side of (2.39). Let ν_{pe} be the collision frequency for momentum transfer for protons colliding with electrons, and ν_{ep} be the collision frequency for momentum transfer for electrons colliding with protons. The momentum transferred from electrons to

protons during the collision is $-\rho_p(\mathbf{u}_p - \mathbf{u}_e)\nu_{pe}$, and the momentum transferred from protons to electrons is $-\rho_e(\mathbf{u}_e - \mathbf{u}_p)\nu_{ep}$. Considering the conservation of momentum during the collisions, we have

$$-\rho_p(\mathbf{u}_p - \mathbf{u}_e)\nu_{pe} - \rho_e(\mathbf{u}_e - \mathbf{u}_p)\nu_{ep} = 0, \tag{2.64}$$

or

$$\rho_p\nu_{pe} = \rho_e\nu_{ep}. \tag{2.65}$$

The right hand side of equation (2.39) describes the total change of the momentum of the system. Thus we can add the transferred momentum due to collisions to the right hand side of (2.39):

$$\frac{\partial}{\partial t}(m_p n_p \mathbf{u}_p) + \nabla\cdot(p_p\mathbf{I} + m_p n_p \mathbf{u}_p\mathbf{u}_p) - n_p q_p(\mathbf{E} + \mathbf{u}_p \times \mathbf{B}) = -m_p n_p(\mathbf{u}_p - \mathbf{u}_e)\nu_{pe}, \tag{2.66}$$

$$\frac{\partial}{\partial t}(m_e n_e \mathbf{u}_e) + \nabla\cdot(p_e\mathbf{I} + m_e n_e \mathbf{u}_e\mathbf{u}_e) - n_e q_e(\mathbf{E} + \mathbf{u}_e \times \mathbf{B}) = -m_e n_e(\mathbf{u}_e - \mathbf{u}_p)\nu_{ep}. \tag{2.67}$$

Multiplying (2.66) with m_e and (2.67) with m_p, and subtracting them, we have

$$\begin{aligned}
&m_p m_e \frac{\partial}{\partial t}[n(\mathbf{u}_p - \mathbf{u}_e)] + (m_e\nabla p_p - m_p\nabla p_e) \\
&\qquad + m_p m_e \nabla\cdot(n\mathbf{u}_p\mathbf{u}_p - n\mathbf{u}_e\mathbf{u}_e) \\
&- m_e ne(\mathbf{E} + \mathbf{u}_p \times \mathbf{B}) - m_p ne(\mathbf{E} + \mathbf{u}_e \times \mathbf{B}) \\
&\qquad + m_p m_e n(\mathbf{u}_p - \mathbf{u}_e)(\nu_{pe} + \nu_{ep}) \\
&= m_p m_e \frac{\partial}{\partial t}[n(\mathbf{u}_p - \mathbf{u}_e)] + (m_e\nabla p_p - m_p\nabla p_e) \\
&\qquad + m_p m_e \nabla\cdot[n\mathbf{u}_p(\mathbf{u}_p - \mathbf{u}_e) + n(\mathbf{u}_p - \mathbf{u}_e)\mathbf{u}_e] \\
&\qquad - \rho e(\mathbf{E} + \mathbf{u} \times \mathbf{B}) + (m_p - m_e)\mathbf{j} \times \mathbf{B} \\
&\qquad + \frac{m_p m_e}{e}(\nu_{pe} + \nu_{ep})\mathbf{J} = 0.
\end{aligned} \tag{2.68}$$

Multiplying by e, we obtain

$$m_p m_e \frac{\partial \mathbf{J}}{\partial t} + e(m_e\nabla p_p - m_p\nabla p_e)$$

$$+m_p m_e \nabla \cdot (\mathbf{u}_p \mathbf{J} + \mathbf{J}\mathbf{u}_e)$$
$$-\rho e^2(\mathbf{E} + \mathbf{u} \times \mathbf{B}) + e(m_p - m_e)\mathbf{j} \times \mathbf{B}$$
$$+m_p m_e(\nu_{pe} + \nu_{ep})\mathbf{J} = 0. \tag{2.69}$$

Re-arranging terms in (2.69), it becomes

$$\mathbf{E} = -\mathbf{u} \times \mathbf{B} + \frac{m_p m_e}{\rho e^2}(\nu_{pe} + \nu_{ep})\mathbf{J} + \frac{(m_p - m_e)}{\rho e}\mathbf{J} \times \mathbf{B}$$
$$+\frac{1}{\rho e}(m_e \nabla p_p - m_p \nabla p_e) + \frac{m_p m_e}{\rho e^2}\frac{\partial \mathbf{J}}{\partial t} + \frac{m_p m_e}{\rho e^2}\nabla \cdot (\mathbf{u}_p \mathbf{J} + \mathbf{J}\mathbf{u}_e). \tag{2.70}$$

Considering $m_e \ll m_p$ and dropping terms that are of the order $\frac{m_e}{m_p}$, we have

$$\mathbf{E} = -\mathbf{u} \times \mathbf{B} + \eta \mathbf{J} + \frac{1}{ne}\mathbf{J} \times \mathbf{B} - \frac{1}{ne}\nabla p_e + \frac{m_e}{ne^2}[\frac{\partial \mathbf{J}}{\partial t} + \nabla \cdot (\mathbf{u}_p \mathbf{J} + \mathbf{J}\mathbf{u}_e)] \tag{2.71}$$

where $\eta = \frac{m_e}{ne^2}(\nu_{pe} + \nu_{ep})$ is the electric resistivity.

We have now a full set of equations for the solar wind and magnetosphere plasma system:

$$\frac{\partial \rho}{\partial t} = -\nabla \cdot (\rho \mathbf{u}), \tag{2.72}$$
$$\frac{\partial (\rho \mathbf{u})}{\partial t} = -\nabla \cdot (p\mathbf{I} + \rho \mathbf{u}\mathbf{u}) + \rho_q \mathbf{E} + \mathbf{J} \times \mathbf{B}, \tag{2.73}$$
$$\frac{\partial}{\partial t}(\frac{3p}{2} + \frac{1}{2}\rho u^2) = -\nabla \cdot [(\frac{5}{2}p + \frac{1}{2}\rho u^2)\mathbf{u}] + \mathbf{J} \cdot \mathbf{E}, \tag{2.74}$$
$$\mathbf{E} = -\mathbf{u} \times \mathbf{B} + \eta \mathbf{J} + \frac{1}{ne}\mathbf{J} \times \mathbf{B} - \frac{1}{ne}\nabla p_e + \frac{m_e}{ne^2}[\frac{\partial \mathbf{J}}{\partial t} + \nabla \cdot (\mathbf{u}_p \mathbf{J} + \mathbf{J}\mathbf{u}_e)], \tag{2.75}$$
$$\nabla \cdot \mathbf{E} = \frac{\rho_q}{\varepsilon_0}, \tag{2.76}$$
$$\nabla \cdot \mathbf{B} = 0, \tag{2.77}$$
$$\nabla \times \mathbf{E} = -\frac{\partial B}{\partial t}, \tag{2.78}$$
$$\nabla \times \mathbf{B} = \mu_0 \epsilon_0 \frac{\partial \mathbf{E}}{\partial t} + \mu_0 \mathbf{J}. \tag{2.79}$$

However,we still need to simplify (2.73) and (2.75). To do so, we normalize the above equations to find out the relative importance of the terms in these equations. The normalization also helps numerical simulation to avoid extremely large or small

numbers in calculation. The variables in the above equations can be normalized as:

$$\rho = \rho_0\rho',\ L = L_0L',\ T = T_0T',\ \rho_q = \rho_{q0}\rho'_q,\ p = p_0p',$$
$$\mathbf{u} = u_0\mathbf{u}',\ \mathbf{B} = B_0\mathbf{B}',\ \mathbf{E} = E_0\mathbf{E}',\ \mathbf{J} = J_0\mathbf{J}',\ \eta = \eta_0\eta', \tag{2.80}$$

where L and T are characteristic spatial and temporal scales, the primed variables are normalized variables without unit, and $\rho_0, L_0, T_0, \rho_{q0}, p_0, u_0, B_0, E_0, J_0$ and η_0 are the normalization parameters chosen such that the primed values are $O(1)$. The equations (2.72)–(2.79) are then rewritten as

$$\frac{\rho_0}{T_0}\frac{\partial\rho'}{\partial t'} = -\frac{\rho_0 u_0}{L_0}\nabla'\cdot(\rho'\mathbf{u}'), \tag{2.81}$$
$$\frac{\rho_0 u_0}{T_0}\frac{\partial(\rho'\mathbf{u}')}{\partial t'} = -\frac{1}{L_0}\nabla'\cdot(p_0p'\mathbf{I} + \rho_0u_0^2\rho'\mathbf{u}'\mathbf{u}') + \rho_{q0}E_0\rho'_q\mathbf{E}' + J_0B_0\mathbf{J}'\times\mathbf{B}', \tag{2.82}$$
$$\frac{1}{T_0}\frac{\partial}{\partial t'}(\frac{3}{2}p_0p' + \frac{1}{2}\rho_0u_0^2\rho'u'^2) = -\frac{1}{L_0}\nabla'\cdot[(\frac{5}{2}p_0p' + \frac{1}{2}\rho_0u_0^2\rho'u'^2)u_0\mathbf{u}'] + J_0E_0\mathbf{J}'\cdot\mathbf{E}', \tag{2.83}$$
$$E_0\mathbf{E}' = -u_0B_0\mathbf{u}'\times\mathbf{B}' + \eta_0J_0\eta'\mathbf{J}' + \frac{J_0B_0}{ne}\mathbf{J}'\times\mathbf{B}' - \frac{p_0}{L_0ne}\nabla'p'_e + \frac{m_e}{ne^2}[\frac{J_0}{T_0}\frac{\partial J'}{\partial t'} + \frac{J_0u_0}{L_0}\nabla'\cdot(u'_p\mathbf{J}' + \mathbf{J}'\mathbf{u}'_e)], \tag{2.84}$$
$$\frac{E_0}{L_0}\nabla'\cdot\mathbf{E}' = \frac{\rho_{q0}\rho'_q}{\epsilon_0}, \tag{2.85}$$
$$\nabla'\cdot\mathbf{B}' = 0, \tag{2.86}$$
$$\frac{B_0}{L_0}\nabla'\times\mathbf{B}' = \mu_0\epsilon_0\frac{E_0}{T_0}\frac{\partial\mathbf{E}'}{\partial t'} + \mu_0J_0\mathbf{J}', \tag{2.87}$$
$$\frac{E_0}{L_0}\nabla'\times\mathbf{E}' = -\frac{B_0}{T_0}\frac{\partial\mathbf{B}'}{\partial t'}. \tag{2.88}$$

Choosing only L_0, ρ_0, and B_0 as the independent normalization parameters, and letting the primed values be $O(1)$ in the above equations, I can obtain the other normalization factors as

$$u_0 = \frac{B_0}{\sqrt{\mu_0\rho_0}},\ T_0 = \frac{L_0}{u_0} = \frac{L_0\sqrt{\mu_0\rho_0}}{B_0},\ p_0 = \frac{B_0^2}{\mu_0},\ , \tag{2.89}$$
$$E_0 = \frac{B_0^2}{\sqrt{\mu_0\rho_0}},\ J_0 = \frac{B_0}{\mu_0L_0},\ \rho_{q0} = \frac{\epsilon_0E_0}{L_0},\ \eta_0 = \frac{\mu_0L_0^2}{T_0}. \tag{2.90}$$

Substituting them into (2.81)–(2.88), we obtain:

$$\frac{\partial \rho'}{\partial t'} = -\nabla' \cdot (\rho' \mathbf{u}'), \tag{2.91}$$

$$\frac{\partial (\rho' \mathbf{u}')}{\partial t'} = -\nabla' \cdot (p' \mathbf{I} + \rho' \mathbf{u}' \mathbf{u}') + \frac{u_0^2}{c^2} \rho'_q \mathbf{E}' + \mathbf{J}' \times \mathbf{B}', \tag{2.92}$$

$$\frac{\partial}{\partial t'}(\frac{3}{2}p' + \frac{1}{2}\rho' u'^2) = -\nabla' \cdot [(\frac{5}{2}p' + \frac{1}{2}\rho' u'^2)\mathbf{u}'] + \mathbf{J}' \cdot \mathbf{E}', \tag{2.93}$$

$$\mathbf{E}' = -\mathbf{u}' \times \mathbf{B}' + \eta' \mathbf{J}' + \frac{1}{2\pi n}\frac{T_{cp}}{T_0}\mathbf{J}' \times \mathbf{B}' - \frac{1}{2\pi n}\frac{T_{cp}}{T_0}\nabla' p'_e + \frac{1}{(2\pi)^2}\frac{T_{cp}T_{ce}}{T_0^2}[\frac{\partial J'}{\partial t'} + \nabla' \cdot (u'_p \mathbf{J}' + \mathbf{J}' \mathbf{u}'_e)], \tag{2.94}$$

$$\nabla' \cdot \mathbf{E}' = \rho'_q, \tag{2.95}$$

$$\nabla' \cdot \mathbf{B}' = 0, \tag{2.96}$$

$$\nabla' \times \mathbf{B}' = \frac{u_0^2}{c^2}\frac{\partial \mathbf{E}'}{\partial t'} + \mathbf{J}', \tag{2.97}$$

$$\nabla' \times \mathbf{E}' = -\frac{\partial \mathbf{B}'}{\partial t'}. \tag{2.98}$$

where $c = \frac{1}{\sqrt{\mu_0 \epsilon_0}}$ is the light speed, $T_{cp} = \frac{2\pi m_p}{eB_0}$ is the proton gyroperiod, and $T_{ce} = \frac{2\pi m_e}{eB_0}$ is the electron gyroperiod. Since $u_0^2 \ll c$ to a good approximation in the magnetosphere, I can safely drop the term of Coulomb force $\frac{u_0^2}{c^2}\rho'_q \mathbf{E}'$ in (2.92) and the displacement current $\frac{u_0^2}{c^2}\frac{\partial \mathbf{E}'}{\partial t'}$ in (2.97). For the model of the solar wind and magnetosphere, I am mainly interested in processes with characteristic time scales T_0 that are much larger than T_{cp} and T_{ce}. Therefore, I can neglect the third, fourth, and fifth terms of (2.94).

Rewriting (2.91)–(2.98) and dropping the prime for simplicity, I now have the magnetohydrodynamic (MHD) equations in normalized form for the plasma system including the outer magnetosphere and the solar wind around it:

$$\frac{\partial \rho}{\partial t} = -\nabla \cdot (\rho \mathbf{u}), \tag{2.99}$$

$$\frac{\partial (\rho \mathbf{u})}{\partial t} = -\nabla \cdot (p \mathbf{I} + \rho \mathbf{u} \mathbf{u}) + \mathbf{J} \times \mathbf{B}, \tag{2.100}$$

$$\frac{\partial \epsilon}{\partial t} = -\nabla \cdot [(p + \epsilon)\mathbf{u}] + \mathbf{J} \cdot \mathbf{E}, \tag{2.101}$$

$$\mathbf{E} = -\mathbf{u} \times \mathbf{B} + \eta \mathbf{J}, \tag{2.102}$$

$$\frac{\partial \mathbf{B}}{\partial t} = -\nabla \times \mathbf{E}, \tag{2.103}$$

$$\nabla \cdot \mathbf{B} = 0, \tag{2.104}$$

$$\mathbf{J} = \nabla \times \mathbf{B}, \tag{2.105}$$

$$\epsilon = \frac{3}{2}p + \frac{1}{2}\rho u^2, \tag{2.106}$$

where (2.95) is dropped because the plasma is quasi-neutral to an excellent approximation and thus (2.95) is redundant. Equation (2.104) is not needed in solving the equations, but it serves as an initial condition for $\mathbf{B}$. Faraday's law (2.103) ensures that if $\nabla \cdot \mathbf{B} = 0$ initially, this condition will also hold at later times:

$$\nabla \cdot (\frac{\partial \mathbf{B}}{\partial t}) = \frac{\partial}{\partial t}(\nabla \cdot \mathbf{B}) = -\nabla \cdot \nabla \times \mathbf{E} = 0$$

$$\Rightarrow \nabla \cdot \mathbf{B} = const. \tag{2.107}$$

The plasma is considered collisionless when deriving conservation equations, but is considered to have proton-electron collisions when deriving the generalized Ohm's law. Thus, in the computation, the η in (2.102) is a switch function depending on a threshold value such that η is non-zero in diffusive region, and is zero in other regions.

In deriving the above equations, I have made the following assumptions:

1 There are only protons and electrons.

2 The proton mass is much larger than the electron mass.

3 The proton number density is very close to the electron number density.

4 The spatial scale of the problem is much larger than the Debye length and the ion gyroradius.

5 The temporal scale of the problem is much larger than the ion gyroperiod.

6 The phase space density decreases faster than $\frac{1}{v^2}$ when $\mathbf{v}$ approaches infinity.

7 Plasma phase space distribution is spherically symmetric.

8 The plasma is collisionless except in reconnection region.

For the solar wind near the Earth's orbit and the outer magnetosphere, these conditions are usually well satisfied. However, one should note that there is ∼2% - 10% of He^{2+} in the solar wind, and a very small fraction of heavy ions. The population of O^+ in the magnetotail may increase during magnetic storm time (*Kistler et al.*, 2002, 2004; *et al*, 2004). Observations show that most of the solar wind has a phase space distribution represented by a bi-Maxwellian. However, the phase space distribution function of the plasma may not always be Maxwellian and spherically symmetric. The MHD equations do not describe all particle drifts, such as curvature drift and gradient drift, while $\mathbf{E}\times\mathbf{B}$ drift is included. Such drifts can be important in the tail current sheet or in the inner magnetosphere. Wave-particle interaction is not addressed by MHD theory either, but may play a role in diffusive entry of particles on the magnetosphere boundary layer (*Thorne and Tsurutani*, 1991) and in the heating of H^+ ions (*Horne and Thorne*, 1997). In deriving the conservation equations, I assumed that the plasma is collisionless, which may not be the case in diffusive region where magnetic reconnection occurs. To address magnetic reconnection which occur frequently in the outer magnetosphere, we derive the General Ohm's Law by considering proton-electron collisions in the conservation equation of momentum. The simplified Generalized Ohm's Law (2.102) drops the Hall term ($\frac{1}{ne}\mathbf{J}\times\mathbf{B}$), which may also play a role in magnetic reconnection (*Dorelli*, 2003).

2.3 OpenGGCM

Open Geospace General Circulation Model, previously UCLA Global MHD Model, is developed by Professor Joachim Raeder. A detailed description about the OpenG-

GCM can be found online http://openggcm.sr.unh.edu/wiki/index.php/Main_Page, the tutorial introduction (*Raeder*, 2003), and Dr. Yongli Wang's dissertation (*Wang*, 2003). Here I just give a brief introduction.

2.3.1 The governing equations

The governing MHD equations used in OpenGGCM are the equations 2.99 – 2.106. In most part of the studied region, the ideal MHD equations, where the resistivity in Ohm's law (equation 2.106) is zero, are used in the computation. For the diffusive area, the term with anomalous resistivity η is applied. Although the precise mechanisms that cause anomalous diffusion are not well known, it is generally believed that anomalous diffusion is a function of the local current density, thus a suitable parametrization is given by:

$$\eta = \begin{cases} \alpha j'^2 & : \quad j' \geq \delta \\ 0 & : \quad j' < \delta \end{cases}, \tag{2.108}$$

$$j' = \frac{|j|\Delta}{|B| + \varepsilon}, \tag{2.109}$$

where j' is a normalized local current density, Δ is the grid spacing, δ and α are empirical constants, and ε is a very small number to make sure the denominator of 2.109 is not zero (*Raeder et al.*, 1996).

2.3.2 Simulation geometry and grid

The geometric space of the Earth's magnetosphere in simulation is usually set to be a box where $Xgse \geq$ 18 R_E for the boundary in the sunward side, $Xgse \leq$ -200 R_E in the tailward direction, and $|Ygse|$ and $|Zgse| \geq$ 25 R_E in the transverse directions. The box should be well within supermagnetosonic flows. However, these values for the box is only a guide. Especially in choosing the sunward boundary when the solar wind magnetosonic Mach number is low, it must be farther away from Earth

to make sure that the bow shock is within the simulation domain. In OpenGGCM computation, a coordinate system related to GSE is used:

$$x = -x_{gse}, y = -y_{gse}, z = z_{gse}. \tag{2.110}$$

For the region from solar wind to the plasma sheet, there are various distinctive regions and boundaries between them. Thus, the numerical grid has an enormous effect on the performance of the simulation. A uniform Cartesian grid provides lowest programming overhead, but wastes computation resources for regions where solutions are smooth, and under resolves regions with sharp gradients and shocks (*Ogino*, 1986; *Ogino et al.*, 1994; *Watanabe and Sato*, 1990). A numerical grid with adaptive mesh refinement incurs substantial programming and computer overhead, but can provide more accurate solutions for a given number of grid cells (*Berger and Olinger*, 1984; *Berger and Colella*, 1989; *Powell et al.*, 1999) .

OpenGGCM uses a stretched Cartesian grid that can be adapted to the solution, and maintains essentially all of the advantages of a uniform Cartesian grid (*Raeder*, 1995; *Usadi et al.*, 1993). Figures 2-1 and 2-2 show an example of the grid spacing distribution on the GSE XY plane and YZ plane in an OpenGGCM simulation for this study. The grid spacing distribution indicates that this grid provides very high resolution in the X direction at the bow shock and the magnetopause, relative high resolution in the X direction at the near tail region, and very high resolution in the Y and Z direction near the equatorial plane (good for the tail plasma sheet) and the noon-midnight meridian. Thus, this grid can provide sufficient resolution for the study of solar wind plasma entry into the magnetosphere, which occurs mostly in the region from magnetosheath to $\sim$60 R_E in the magnetotail. Other areas have substantially lower resolution and consequently require less computation resources.

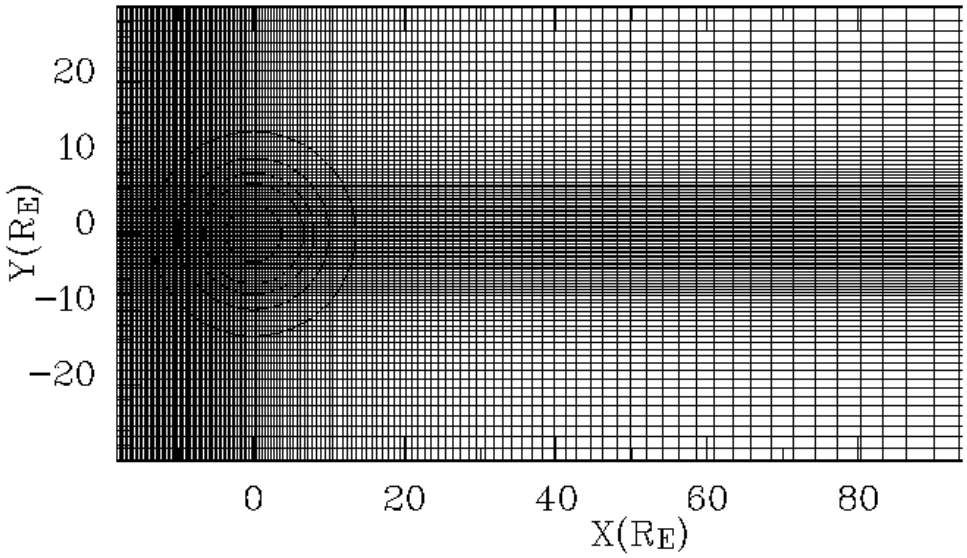

Figure 2-1: A stretched grid on XY plane. Note that here the X coordinate is the opposite of GSE X coordinate.

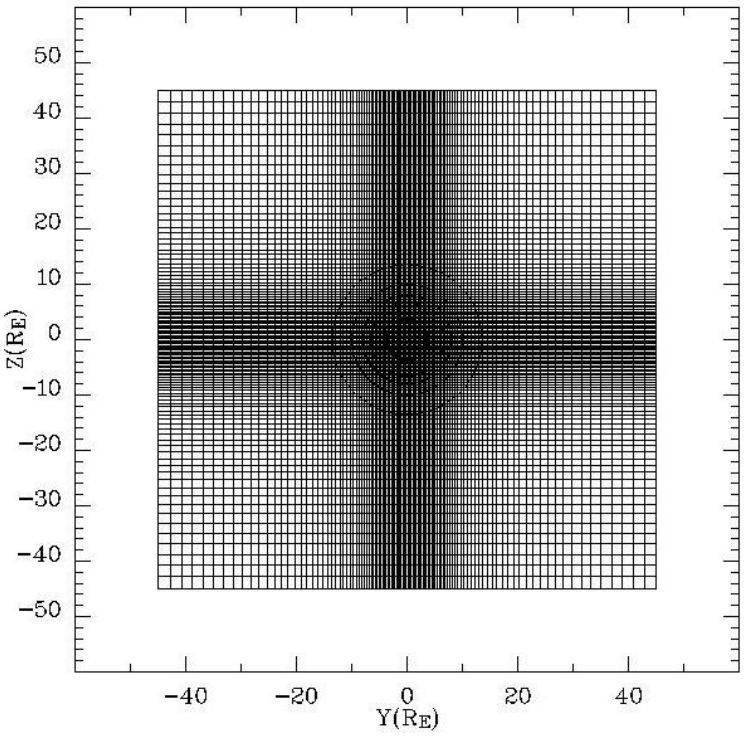

Figure 2-2: A stretched grid on YZ plane. Here the Y coordinate is the opposite of GSE Y.

2.3.3 Numerical methods

To solve the MHD equations numerically, we need to approximate both the time derivatives and the spatial derivatives. The plasma part of the conservation equations (2.99)–(2.100) has the form

$$\frac{\partial U}{\partial t} = -\nabla \cdot \mathbf{F}(U), \tag{2.111}$$

where U is a macroscopic value of the plasma, and $\mathbf{F}$ is the flux of U.

For time differencing, the predictor-corrector scheme is used:

$$U^{n+\frac{1}{2}} = U^n - \frac{1}{2}\Delta t \nabla \cdot \mathbf{F}(U^n), \tag{2.112}$$

$$U^{n+1} = U^n - \Delta t \nabla \cdot \mathbf{F}(U^{n+\frac{1}{2}}). \tag{2.113}$$

The numerical errors are proportional to Δt^2. The maximum allowed time step is restricted by the stability requirement (the Courant-Friedrichs-Levy, or CFL criterion) (*Sod*, 1985):

$$\Delta t_{max} \leq \delta \frac{min(\Delta x, \Delta y, \Delta z)}{|\mathbf{v}| + v_{MS}}, \tag{2.114}$$

where δ is a constant of the order $O(1)$, and $v_{MS} = \sqrt{\frac{\gamma p}{\rho} + \frac{B^2}{\rho}}$ is the fast magnetic sonic speed after normalization.

To spatially discretize the right hand side of equation (2.111) in a regular Cartesian grid (in 2d for simplicity here), the cell centers (U_{ij}) are on the grid points at (x_i, y_i), and the cell corners are at $(x_{i+1/2,j+1/2}, y_{i+1/2,j+1/2})$, where $x_i = i\Delta x, i = 1, ...$ and $y_j = j\Delta y, j = 1, ...$ The numerical fluxes are on the middle of the edges of the cells, as shown in Figure 2-3. The right hand side of equation (2.111) is discretized as:

$$\frac{\partial U}{\partial t} = -\frac{1}{\Delta x}(f_{i+\frac{1}{2},j}(U) - f_{i-\frac{1}{2},j}(U)) - \frac{1}{\Delta y}(f_{i,j+\frac{1}{2}}(U) - f_{i,j-\frac{1}{2}}(U)), \tag{2.115}$$

where the numerical fluxes $f_{i+\frac{1}{2},j}$ and $f_{i,j+\frac{1}{2}}$ are functions of the grid values. Such discretization guarantees the global conservation of the quantity U, because the sum of $\partial U/\partial t$ over the entire grid is zero,except for the fluxes through the physical boundaries. There are several schemes to construct the numerical fluxes. Different schemes

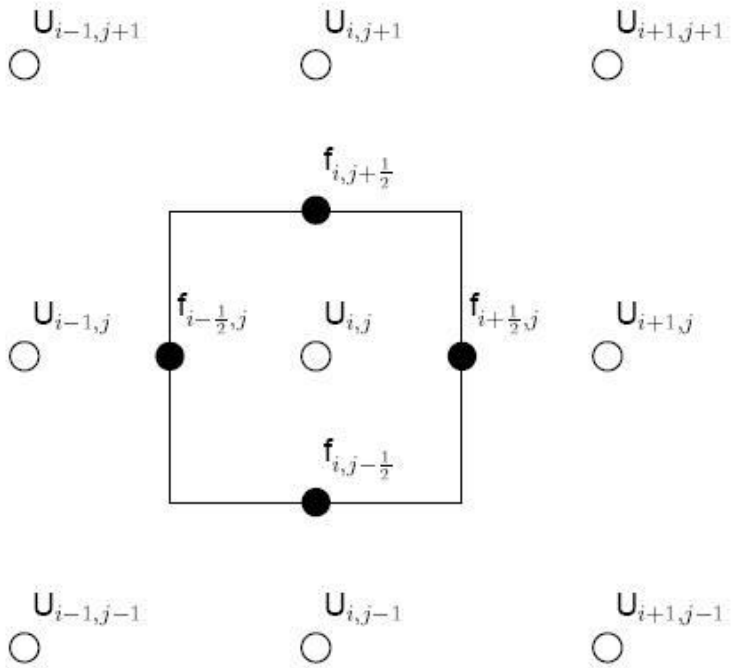

Figure 2-3: Variable placement of the numerical fluxes. The circles are grid points with value U and the solid circles are the numerical fluxes.

have different order of accuracy. The schemes used in OpenGGCM are the low order Rusanov scheme

$$f_{i+\frac{1}{2}} = \frac{1}{2}(F(U_i) + F(U_{i+1})) - \frac{1}{4}(|v_i| + |v_{i+1}| + c_i + c_{i+1})(U_{i+1} - U_i), \tag{2.116}$$

where c is the sound speed, and the fourth order central scheme

$$f_{i+\frac{1}{2}} = \frac{7}{12}(F(U_i) + F(U_{i+1})) - \frac{1}{12}(F(U_{i-1}) + F(U_{i+2})). \tag{2.117}$$

The error terms associated with the spatial discretization can be derived from the Taylor series expansion

$$\begin{aligned}\Delta x \frac{\partial U}{\partial t} = -(f_{i+\frac{1}{2}} - f_{i-\frac{1}{2}}) + a_1(\Delta x)^2 \frac{\partial^2}{\partial x^2} F(U) + b_1(\Delta x)^3 \frac{\partial^3}{\partial x^3} F(U) \\ + a_2(\Delta x)^4 \frac{\partial^4}{\partial x^4} F(U) + b_2(\Delta x)^5 \frac{\partial^5}{\partial x^5} F(U) + ...,\end{aligned} \tag{2.118}$$

where the coefficients a_1, b_1, etc. depend on the choice of the numerical flux scheme. The a terms cause numerical *diffusion*, which tends to smear out the solution, in

particular at discontinuities where the derivatives of the solution become large. The b terms cause numerical *dispersion*, which can cause under/overshoots near discontinuities, and may lead to nonphysical solutions, such as negative density or pressure. All a terms vanish when using symmetric central schemes. To avoid under/overshoots near discontinuities and achieve higher accuracy at regions where the solution is smooth, a hybrid flux scheme is used:

$$f_{i+\frac{1}{2}} = \theta_{i+\frac{1}{2}} f^h_{i+\frac{1}{2}} + (1 - \theta_{i+\frac{1}{2}}) f^l_{i+\frac{1}{2}} \tag{2.119}$$

where f^l is a low order (for example Rusanov) flux, f^h is a high order (for example fourth order central) flux, and θ is a switch function and depends on gradients in the solution (*Harten and Zwas*, 1972; *Zalesak*, 1981).

When computing the discretized magnetic field $\mathbf{B}$ and electric field $\mathbf{E}$, we must make sure that $\nabla \cdot \mathbf{B} = 0$ is conserved, as required by (2.107). To do so, a scheme conserving magnetic flux is used (*Yee*, 1966; *Evans and Hawley*, 1988). The magnetic field components are placed on the center of cell faces:

$$(B_x)_{i+\frac{1}{2},j,k},\ (B_y)_{i,j+\frac{1}{2},k},\ (B_z)_{i,j,k+\frac{1}{2}}, \tag{2.120}$$

and the electric field on the centers of the cell edges:

$$(E_x)_{i,j+\frac{1}{2},k+\frac{1}{2}},\ (E_y)_{i+\frac{1}{2},j,k+\frac{1}{2}},\ (E_z)_{i+\frac{1}{2},j+\frac{1}{2},k}. \tag{2.121}$$

According to Faraday's law, the magnetic field time integration is simply:

$$\frac{\partial}{\partial t}(B_x)_{i+\frac{1}{2},j,k} = \frac{1}{\Delta z}[(E_y)_{i+\frac{1}{2},j,k+\frac{1}{2}} - (E_y)_{i+\frac{1}{2},j,k-\frac{1}{2}}] - \frac{1}{\Delta y}[(E_z)_{i+\frac{1}{2},j+\frac{1}{2},k} - (E_z)_{i-\frac{1}{2},j+\frac{1}{2},k}], \tag{2.122}$$

and analogous for B_y and B_z. By advancing the field components in this way on all 6 cell faces and summing them up, the time change of the magnetic flux Φ through all 6 cell faces vanishes:

$$\frac{\partial}{\partial t} \int \int_{cell} \Phi df = 0. \tag{2.123}$$

Thus the combined magnetic flux Φ through all 6 cell faces remains unchanged during the time integration, and the magnetic field remains divergence-free.

The above discussion is based on the regular Cartesian grid. For the stretched Cartesian grid used in this model, the derivatives need only be multiplied with the appropriate geometric factors:

$$\frac{\partial}{\partial x}F(x,y,z) = \frac{\partial F}{\partial i}(\frac{\partial x}{\partial i})^{-1} \tag{2.124}$$

$$\frac{\partial}{\partial y}F(x,y,z) = \frac{\partial F}{\partial j}(\frac{\partial y}{\partial j})^{-1} \tag{2.125}$$

$$\frac{\partial}{\partial z}F(x,y,z) = \frac{\partial F}{\partial k}(\frac{\partial z}{\partial k})^{-1}, \tag{2.126}$$

where the coordinates (x, y, z) are analytic functions of the grid indices (i, j, k) which define the stretched grid.

2.3.4 Boundary and initial conditions

There are two boundary conditions: the outer boundary conditions provided by solar wind data and free flow conditions, and the inner boundary conditions in connection with the ionosphere. The solar wind data can be manually created or obtained from in-situ measurements. The inner boundary conditions involve the coupling between the magnetosphere model and an ionosphere model.

For the sunward side outer boundary, the three-dimensional structure of the solar wind needs to be known to satisfy the divergence free nature of the magnetic field (equation 2.104). That is, we need to know the normal vector $\mathbf{n}$ of the solar wind discontinuities. With usually only one (at most several) solar wind monitor spacecraft, the detailed structure of the solar wind is impossible to know. Boundary normal methods, e.g., the minimum variance method, have been used to relieve this problem (*Sonnerup and Cahill*, 1967, 1968) in OpenGGCM.

Sometimes the solar wind structure is manually set to be planar in the direction perpendicular to the Sun-Earth line. That is, the solar wind and IMF values only

vary with time along x coordinate. In this case, one must set IMF x component to be a constant. Otherwise the divergence of magnetic field would be non-zero on a YZ plane because $\frac{\partial B_y}{\partial y} = \frac{\partial B_z}{\partial z} = 0$, but $\frac{\partial B_x}{\partial x} \neq 0$.

For all other sides of the outer boundary, free flow conditions can be applied, i.e.,

$$\frac{\partial \Psi}{\partial \mathbf{n}} = 0, \tag{2.127}$$

for all variables Ψ, except for the normal magnetic field component which must be derived from the $\nabla \cdot \mathbf{B} = 0$ condition.

In the inner boundary region, the magnetosphere is connected to the ionosphere through the field aligned currents (FACs) and the electric field. The ionosphere has a finite conductance and the field lines are dragged through the ionosphere plasma, dissipating energy that must be supplied from the magnetosphere via Poynting flux (*Parker*, 1996; *Strangeway et al.*, 2000; *Strangeway and Raeder*, 2001). In the model, the FACs are generated in the magnetosphere where the MHD calculation extends to 3–4 R_E, and then are mapped along dipole field lines into the ionosphere. At the ionosphere end a potential equation is solved on a sphere (or a section thereof) to yield the ionospheric convection potential. The potential is then mapped back to the inner boundary of the MHD calculation. The ionospheric potential is controlled by the ionospheric conductance which is a tensor including the Hall conductance and Pedersen conductance.

The ionospheric conductance can be computed using empirical formulas, or by feeding the precipitation parameters, along with the potential, into a large-scale ionosphere-thermosphere model which then computes the conductances self-consistently from the electron-neutral collisions. In OpenGGCM, the ionospheric conductances can be either set to be uniform, computed with a build-in empirical formula, or provided by the NOAA Coupled Thermosphere Ionosphere Model (CTIM) (*Fuller-Rowell et al.*, 1996; *Raeder et al.*, 2001).

The initial magnetic field is constructed by the superposition of the geomagnetic dipole with mirror dipole to create $B_x = 0$ surface sunward of Earth. The field on sunward side is then replaced with the initial IMF, providing a $\nabla \cdot \mathbf{B} = 0$ transition. The geomagnetic dipole orientation is set by a given universal time. During each run, the dipole orientation is fixed through out the simulation. The initial plasma conditions are given by a cold (5000° K), tenuous (0.1 cm^{-3}), uniform plasma.

CHAPTER 3

COLD DENSE PLASMA SHEET

3.1 Introduction

It has long been established that the state of plasma sheet is dense and cold for extended northward IMF periods (*Lennartsson and Shelley*, 1986; *Baumjohann et al.*, 1989). The WIND and Geotail spacecraft recently provided many more observations of the cold dense plasma sheet (*Terasawa et al.*, 1997; *Fujimoto et al.*, 1998; *Phan et al.*, 1998, 2000). *Wing and Newell* [2002] examined the spatial extent of the cold dense ions under northward IMF using data from low-altitude DMSP satellites. Most recently, Cluster has observed several CDPS events in the mid-tail at a distance of $\sim$ 19 R_E. One of the events was reported by *Øieroset et al.* [2005] and was an unusually long lasting event. This event is also the main event that has been studied for this dissertation and which will be discussed in the next section. My simulation study and analysis of this event has been published on Geophysical Research Letters (*Li et al.*, 2005). I have also found several other CDPS events observed by Cluster, and one of them will also be presented in this chapter. The "superdense plasma sheet" event presented in Chapter 4 is also accompanied by CDPS observations at larger distance in the tail.

Figure 3-1 shows the locations of cold dense plasma observed by Geotail spacecraft in the tail from 1995 to 1999 (*Fujimoto et al.*, 2002). Most of the CDPS observations are made near the Earth in the tail (X_{GSE} > -30 R_E) and near the equatorial plane. However, there may be cold dense plasma beyond 30 R_E toward the tail and far away

from the equatorial plane can not be observed by Geotail since its apogee is 30 R_E and it is mainly near the equatorial plane from 1995 to 1999.

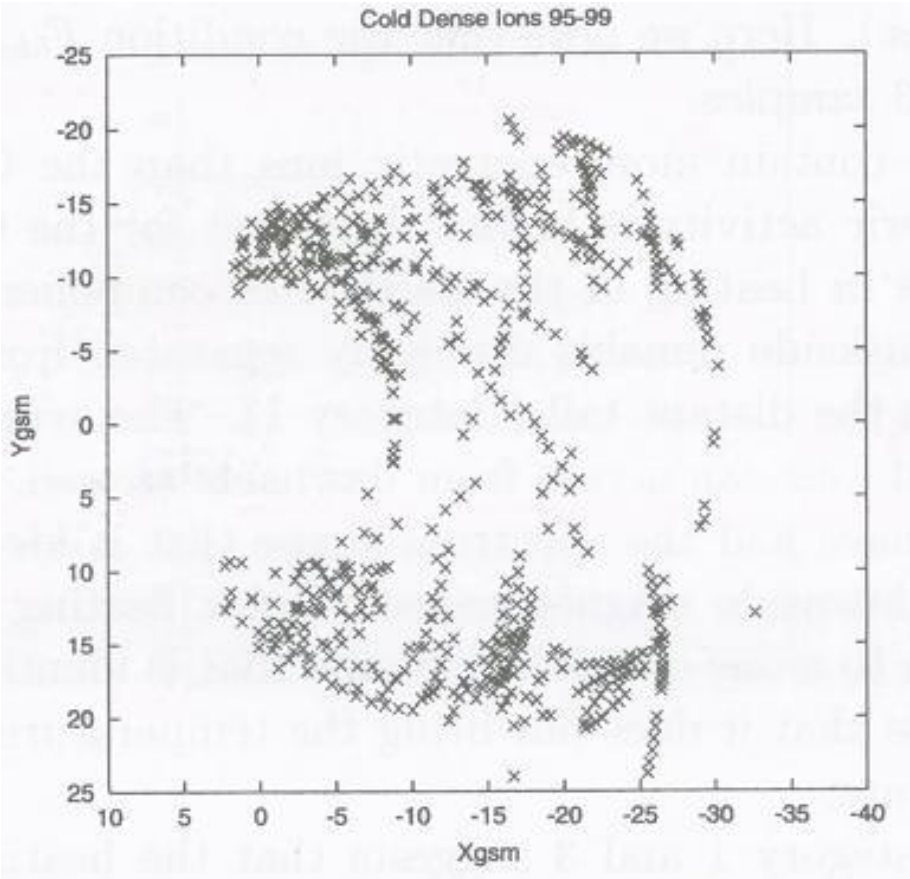

Figure 3-1: The cold dense plasma distribution observed by Geotail (adapted from Fujimoto [2002]). The crosses indicate the Geotail spacecraft locations when it observes CDPS for at least 3 hours.

The observations show that a cold dense plasma sheet is often observed in the mid-tail after a period when the IMF has been northward, on average, for several hours. Sometimes it is observed in the very near tail as close as to the geosynchronous orbit (*Borovsky et al.*, 1997; *Thomsen et al.*, 2003; *Lavraud et al.*, 2005a, 2006a). Most of the time, the CDPS is found to be located near the flanks, and sometimes it is found to penetrate to the center of the tail. It is also often found at high magnetic latitudes ($|B_x| > 15$nT) in the plasma sheet (*Phan et al.*, 1998; *Øieroset et al.*, 2002). The

CDPS plasma is characterized by higher density ($\sim$1 cm^{-3}), lower temperature ($<$ 1 keV), and small flow velocity ($<$ 100 km/s), compared to the usual hot ($>$ 1 keV) and tenuous ($\sim$0.1 cm^{-3}) plasma sheet. It is found to be located on closed field lines (*Fujimoto et al.*, 1998).

In this chapter, I study in detail a CDPS event on October 23, 2003 reported by *Øieroset et al.* [2005]. This is an extreme CDPS event in the sense that it has a very long period of strong northward IMF and relative stable solar wind conditions. During this event, Cluster observes the CDPS for a long period. I show that the OpenGGCM simulation of this event successfully reproduces the observed CDPS, and that it reveals the paths of solar wind plasma entry into the magnetosphere under northward IMF conditions. I then show simulation results of another event to further demonstrate that OpenGGCM can successfully reproduce this CDPS event as well.

3.2 CDPS Event 1 on October 23, 2003

3.2.1 Event observations

From October 18 to November 7, 2003, the Sun unleashed a series of eruptions from three active regions including the largest flare and one of the fastest coronal mass ejection (CME) of solar cycle 23 (*Gopalswamy et al.*, 2005). The CDPS event studied here occurred in a calm time between violent storms. The solar wind conditions and the Cluster observations of this event are shown in Figure 3-2, taken from the detailed report of this event by *Øieroset et al.* [2005].

Solar wind observations

From October 22, 2003, 17:50 UT to October 24, 2003, 02:25 UT, a period of more than 32 hours, an interval of almost purely northward strong IMF was observed by

ACE 235 R_E upstream of the Earth. Its B_x component is relatively small (2-4 nT compared to 6-12 nT for IMF B_z). During this long interval of northward IMF, the solar wind conditions are rather stable with the solar wind speed decreasing steadily from ∼550 km/s to ∼400 km/s, the pressure varying between 1 nPa and 3 nPa most of the interval, and the density staying at values of ∼3-6 cm^{-3}. With a solar wind speed of 550 km/s, the front of strongly northward IMF reaches the dayside magnetopause at ∼18:35 UT, ∼45 minutes after being observed by ACE (at 17:50 UT).

Cluster observations

During the 32 hours of strongly northward IMF, Cluster sampled the near-Earth plasma sheet ($X_{GSM} = -6$ R_E to -13 R_E) on the duskside ($Y_{GSM} = 5$ R_E to 13 R_E) and traversed from the northern to the southern hemisphere ($Z_{GSM} = 6$ R_E to -13 R_E). The CDPS observed by Cluster covered a region of at least 6 R_E in X_{GSM}, 4 R_E in Y_{GSM}, and 18 R_E in Z_{GSM}, including the neutral sheet. At 20:00 UT on October 22, Cluster entered the hot (∼5 keV) and tenuous (0.4 cm^{-3}) plasma sheet from the northern lobe. At 20:32 UT, two hours after the strongly northward IMF front reached the Earth's dayside magnetosphere, the plasma sheet density started to increase and the temperature began to drop as a cold (1 keV) component appeared in the ion distribution (frames g and h in Figure 3-2). At 20:47 UT the temperature had gone down to 1 keV and at 21:28 UT, almost three hours after the northward IMF front reached the Earth, the density reached 1.5 cm^{-3}. The plasma sheet density remained at this level the following 30 hours, while the temperature continued to decrease slowly as the hot plasma sheet ion component faded (frame e of Figure 3-2). The CDPS was nearly stagnant, with flow speeds generally below 50 km/s throughout the interval.

At the beginning of the CDPS interval the CDPS consisted of two distinct popula-

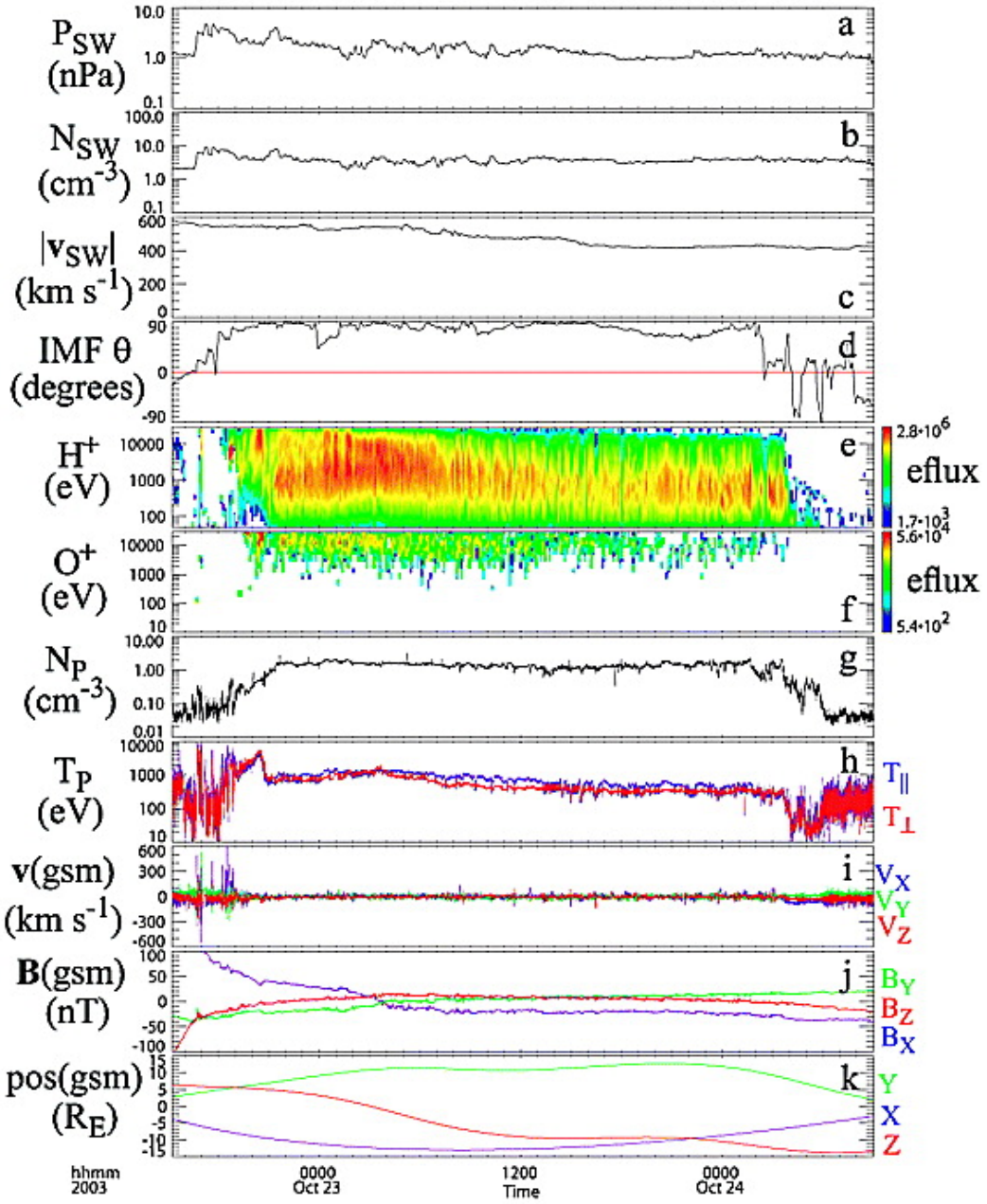

Figure 3-2: Unshifted ACE and Cluster 1 plasma and magnetic field observations from October 22, 2003, 15:00 UT to October 24, 2003, 09:00 UT. (a) ACE solar wind ram pressure; (b) ACE solar wind density; (c) ACE solar wind speed; (d) ACE IMF $\theta = \arctan(B_z/|B_y|)$ angle; (e) H^+ spectrogram from Cluster CODIF; (f) O^+ spectrogram from Cluster CODIF; (g) Cluster HIA density; (h) Cluster HIA temperature; (i) Cluster HIA velocity (GSM); (j) Cluster magnetic field (GSM); (k) Cluster spacecraft position (GSM).

tions of H^+, one at low energies (∼1 keV) and one at high energies (∼10 keV) (frame e of Figure 3-2). The high energy population gradually disappeared and the cooling and densification of the plasma sheet was due to the presence of the low energy component. High energy (> 10 keV) O^+ was present throughout the CDPS interval, with a gradually decreasing flux (frame f of Figure 3-2). No low-energy (∼1 keV) O^+ was present during the CDPS interval.

The end of the northward IMF interval observed by ACE at 02:30 UT reached the front side magnetopause at ∼03:30 UT on October 24, 2003. Cluster observed a drop in both density and temperature at 03:43 UT, indicating the exit of the spacecraft into the southern lobe after almost 32 hours of continuous plasma sheet observations.

3.2.2 Simulation

I run a simulation for this event with the OpenGGCM MHD model, using ACE solar wind and IMF data as input. The simulated time period is from 1500 UT on October 22 to 0300 UT on October 24, 2003. Full 3D data dumps of the simulation results are created every 300 seconds. The grid dimensions are $(-601, 25) \times (-45, 45) \times (-45, 45) R_E$ in GSE coordinates, and its resolution is $0.3 R_E$ in subsolar region and 0.5–1 R_E in the flanks. The primary output parameters are flow velocity components, magnetic field components, plasma density and plasma pressure.

3.2.3 Comparison

Figure 3-3 shows the comparison between the Cluster observations and simulation results for the plasma density, plasma temperature and plasma velocity for the first 14.5 hours of the event. This comparison shows that simulation nearly perfectly matches the observation of these three quantities. That is, the OpenGGCM simulation nearly perfectly reproduces this CDPS event. Further more, the simulation also reproduces the 3 hours of plasma sheet state transition from hot tenuous state to cold dense state

at the beginning of the northward IMF interval.

3.2.4 Entry path

Based on the good match of the simulation results and the data, I further investigated the simulation results to uncover the physical process that leads to the CDPS formation. I traced plasma parcels backward in time from a few locations around the position where the Cluster observed the cold dense plasma. I traced backward the plasma flow using the flow velocity field data from the simulation, i.e.,

$$\frac{d\vec{X}(t)}{dt} = -\vec{V}(\vec{X}(t), t). \tag{3.1}$$

Because the velocity data from the simulation are gridded in space and time, I use linear interpolation in both space and time to compute the right hand side of equation 5.1.

Figure 3-4 shows a typical tracing result for the seed point near the cluster location (-12.5, 14.0, -2.1) R_E in GSE coordinates at 1200 UT on October 23. This plasma parcel starts at 1025 UT in the solar wind. It then moves across the bow shock from 10:27:18 UT to 10:27:54 UT, and traverses the magnetosheath until 1037 UT. At this time, it enters the magnetosphere and is captured on a closed field line. It is subsequently driven northward and sunward in the reconnection zone until 1047 UT. This plasma parcel continues to move northward and sunward for a while, then turns tailward and toward the dusk side and to the flank area. The same time marks are used in Figure 3-5, which shows the variation of plasma and field parameters along the path of this parcel. At 1043 UT, the parcel is closest to the magnetic null point. This is indicated by the point M shown in Figure 3-5. The typical transport time to the Cluster location at (-12.5,14.0,-2.1) R_E is about 1.5 hours.

Figure 3-5 shows several MHD parameters along this path. The panels from the top are plasma temperature, plasma density, magnetic field, flow velocity and its Z-

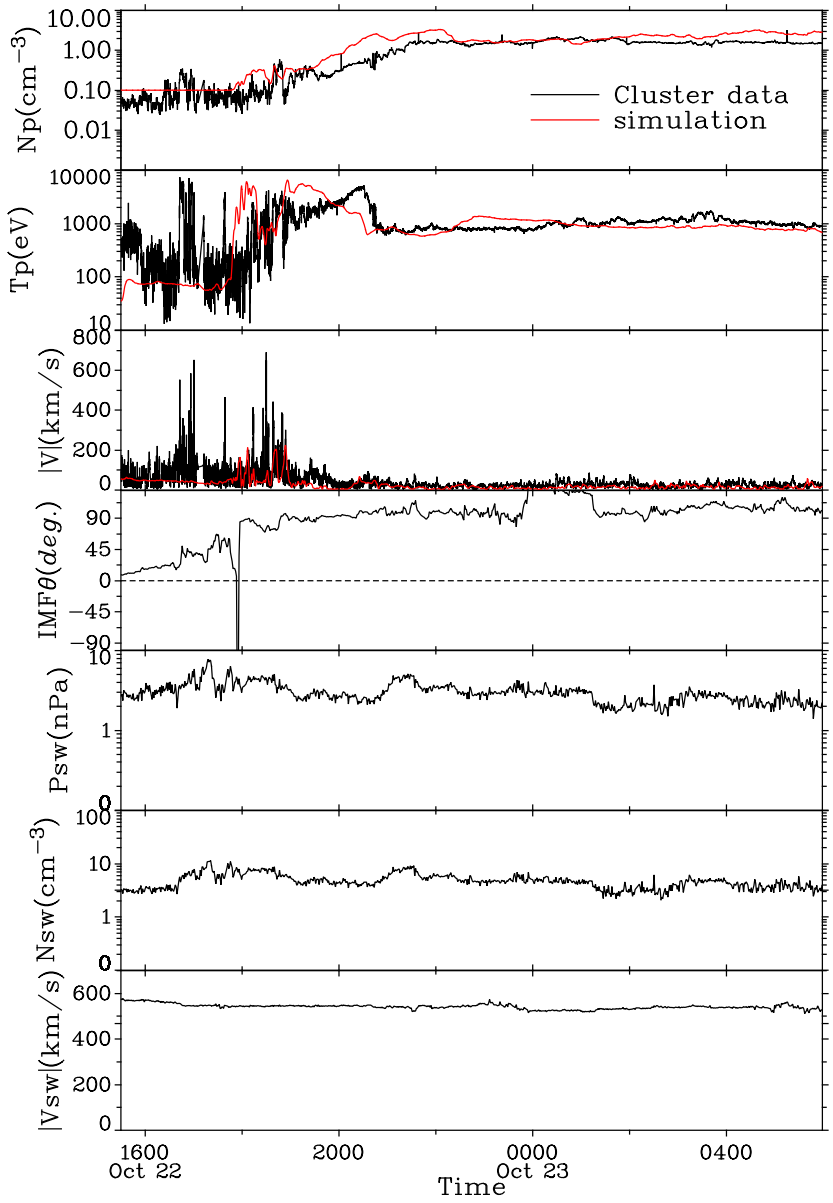

Figure 3-3: CDPS event 1 simulation compared to Cluster observations. The top 3 frames show Cluster observation of plasma density, plasma temperature and plasma velocity with black lines respectively, and show their corresponding simulation results with red lines. The rest of the frames show the ACE measurement of IMF clock angle, dynamic pressure, plasma density and plasma velocity.

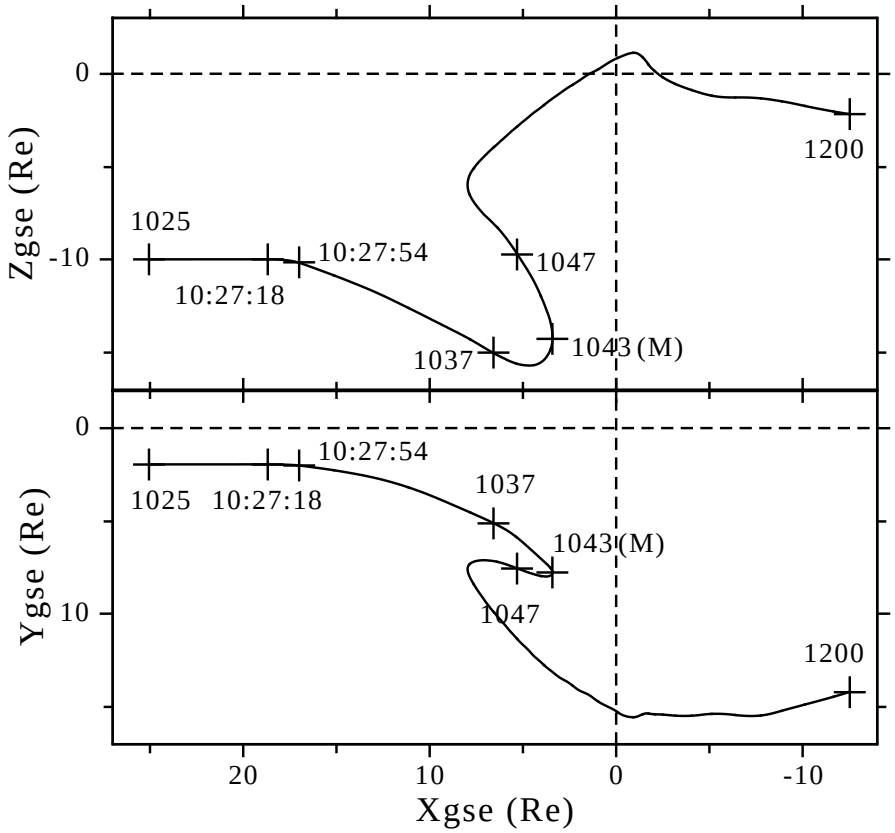

Figure 3-4: One typical plasma flow path that passes near the Cluster position at 1200 UT on October 23, 2003. The time marks between 1025 and 1200 are correspond to the vertical lines and point M in Figure 2.

component. Corresponding to the abrupt changes of the parameter values, the first and second vertical lines define the time at which the plasma moves across the bow shock boundaries. The third vertical line approximately defines the time at which the plasma parcel exits the magnetosheath and enters the magnetosphere. The position of this vertical line is estimated according to the acceleration in Z direction and the temperature enhancement at this time. This time is also in agreement with the time associated with the first closed field line shown in Figure 3-6 (see discussion below). The dotted fourth vertical line indicates the time at which the northward velocity reaches its maximum. The third and fourth vertical lines approximately define the time period during which the parcel is influenced by the cusp reconnection. The minimum magnitude of the magnetic field indicated by the point M suggests that the plasma is passing near the magnetic nulls associated with cusp reconnection. The velocity panels show that the flow is continuously slowing down in the magnetosheath and is further decelerated when it goes toward the reconnection site. It is likely that there is an outflow force from the reconnection site that slows down the plasma, reflects it back and pushes it northward for some time until it is out of the influence of the reconnection region. After entering the magnetosphere, the flow is very slow most of the time except for the small velocity increase near the reconnection site. The density is greater than 1 cm^{-3} throughout, which is substantially larger than the typical plasma sheet density, but is smaller than the magnetosheath density. The temperature panel shows that the plasma is heated by a factor of 3 when it travels from the magnetosheath into the magnetosphere.

Figure 3-6 shows a 3D visualization of the path in Figure 3-4, the plasma's frozen-in magnetic field lines, the equatorial plane color coded with plasma density at 1030 UT, and the magnetic nulls at this time. This figure displays how the magnetosheath plasma enters the magnetosphere. The magnetosheath appears as the yellow ribbon

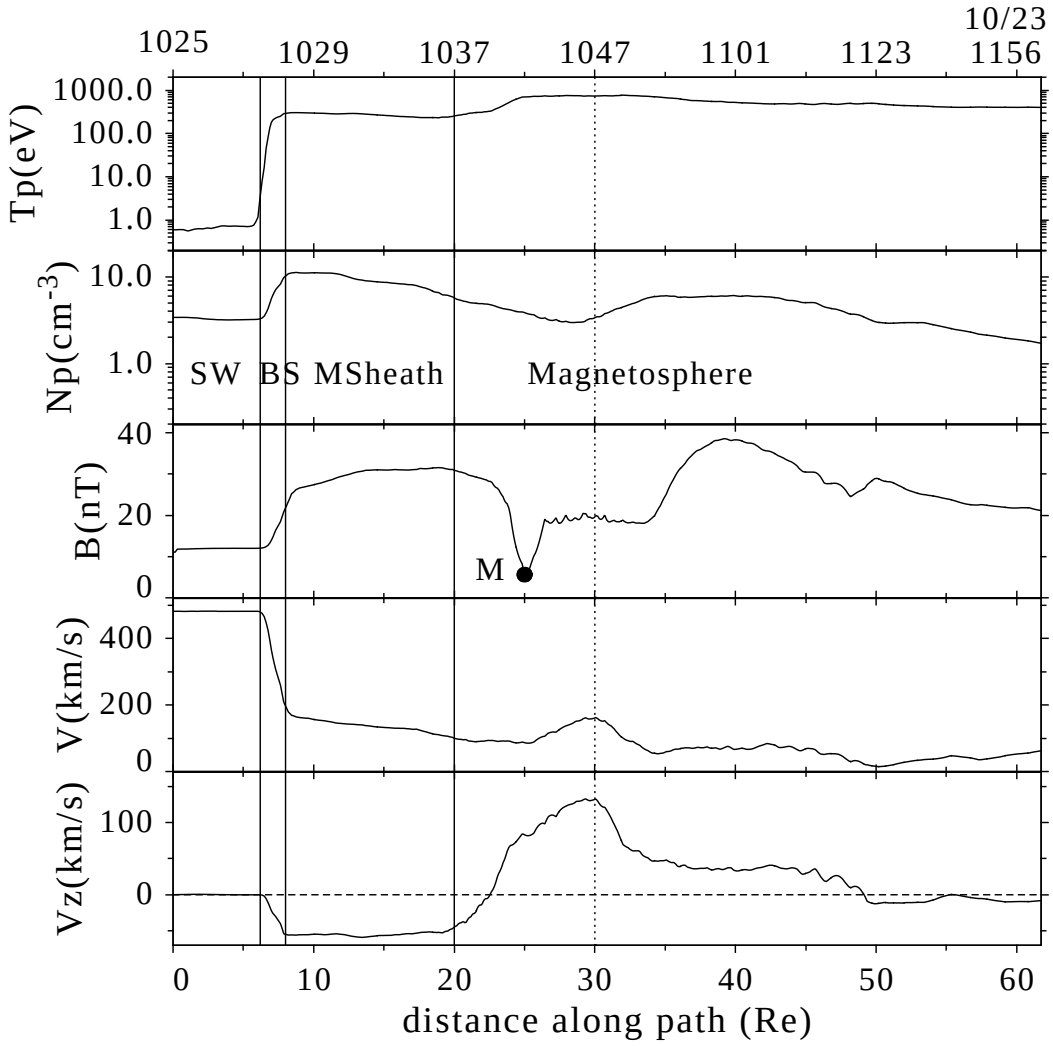

Figure 3-5: MHD parameters along the path shown in Figure 3-4. The top axis is labeled with the corresponding time. The four vertical lines are corresponding to time 10:27:18, 10:27:54, 10:37:00, and 10:47:00, respectively. Point M is at time 10:43:00 UT. SW, BS and MSheath denote the regions and stand for solar wind, bow shock and magnetosheath, respectively.

on the color map on the equatorial plane. The 7^{th} to 10^{th} magnetic field lines look like they result from reconnection between lobe field lines and magnetosheath field lines, especially the 10^{th} field line which is very close to the magnetic null at about (-0.6,12.0,-15.1) R_E. These field lines clearly indicate that there is magnetic tension at the sharply kinked section parallel to magnetopause that slows down the plasma, even turns it slightly sunward, and pushes it northward. This tension force also causes a drift with northward velocity component for ions on this kinked field line section. The 7^{th} to 19^{th} field lines show how the newly created closed flux tube sinks into the magnetosphere and sweeps around the flank to the tail.

3.3 CDPS Event 2 on October 24/25, 2003

3.3.1 Solar wind conditions

This event occurred just one day after the first CDPS event, and also occurred during the extreme solar activity period from October 18 to November 7, 2003. Figure 3-7 shows two days of solar wind conditions from October 24 to 25. At ∼14:45:00 UT October 24, an interplanetary shock arrived at the ACE location. The solar wind speed jumped from ∼400 km/s to ∼500 km/s and stayed at ∼500 km/s during the period of northward IMF, which ended at ∼11:30:00 UT on October 25. The solar wind speed then gradually decreased to ∼400 km/s. Before the shock arrived, the solar wind conditions were near mean values and the IMF had been southward for ∼8 hours. After the shock arrived, there was ∼10 hours of extremely strong northward IMF following by another ∼8 hours of strong northward IMF. The solar wind density and temperature are unusually high most of the time during the northward IMF period except the time period from ∼22:00:00 UT October 24 to ∼01:00:00 UT October 25, during which the solar wind plasma density and temperature dropped back to normal, but was accompanied by extremely strong northward IMF (∼30 nT).

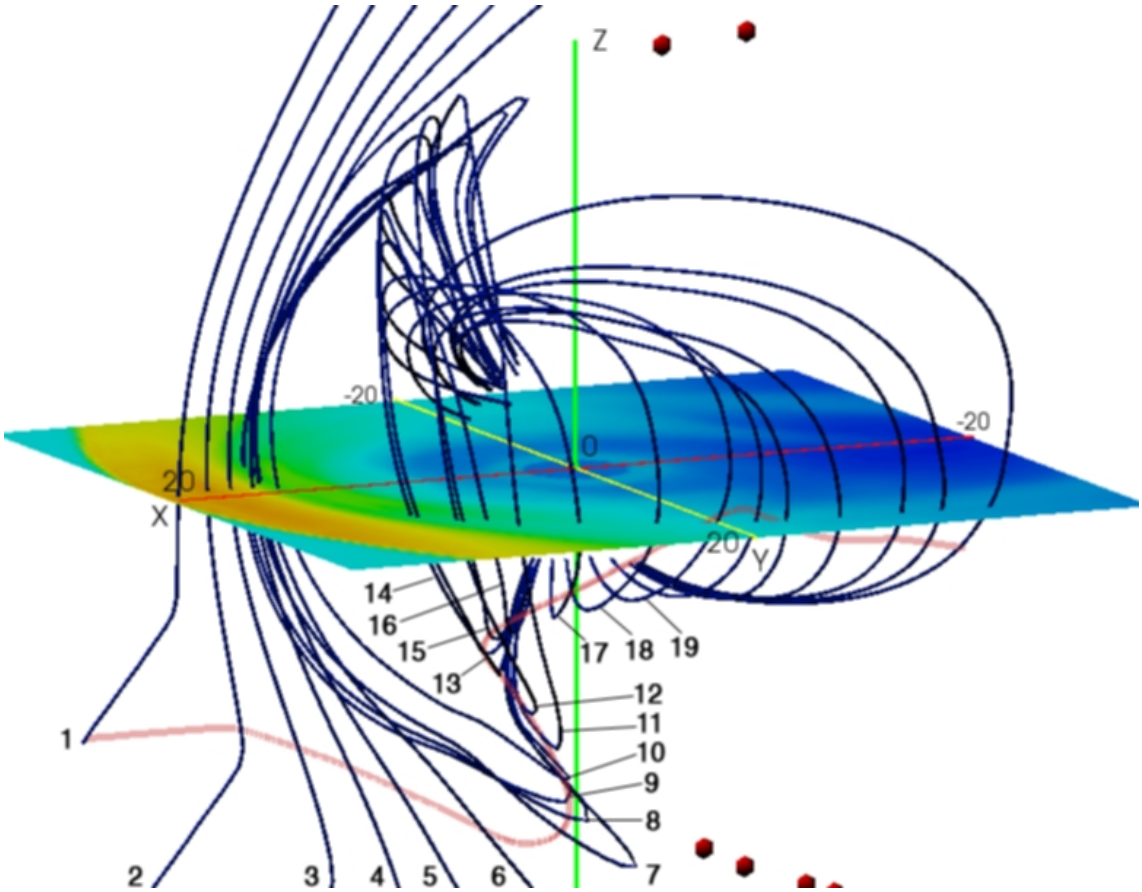

Figure 3-6: Three dimensional visualization of the solar wind plasma entry process. The equatorial plane is a color map of the plasma density. The pink curve is the path shown in Figure 1. The dark blue lines are this path's frozen-in magnetic field lines. The red dots are the magnetic nulls. The red, yellow, and green axes are GSE X, Y, and Z axes, respectively. The first 19 field lines are labeled sequentially in time.

The northward IMF ended on ∼11:30:00 UT October 24, and was followed by ∼2 hours of southward IMF from ∼11:30:00 UT to ∼14:00:00 on October 25.

3.3.2 Cluster observations

Cluster observations from 18:00:00 UT October 24 to 21:00:00 UT October 25, 2003 are shown in Figure 3-8. During this time period, Cluster moved from ∼3 R_E on the dayside to ∼12.4 R_E in the tail, from the dawn side to the dusk side and while staying close to the equatorial plane. This orbit let Cluster have a good chance to go through the plasma sheet. During the period of extremely strong northward IMF from 18:00:00 UT October 24 to 02:00:00 UT October 25, Cluster was close to the Earth (<∼8 R_E). Around 20:00:00 UT October 24, Cluster observed a spike of the plasma density because it was passing through the radiation belts. From 03:00:00 UT to 12:00:00 UT on October 25, Cluster observed the CDPS. Cluster then observed the plasma sheet changing from a state of cold and dense to a state of hot and tenuous.

3.3.3 Simulation

If a simulation period is too long, the error for the simulation near the end of the period will be very large. The geomagnetic dipole orientation is fixed according to a selected time stamp in the OpenGGCM simulation. In a long lasting simulation, the simulation result at a time that is far away from this selected time stamp may have large error due to the change of the dipole orientation in reality. Since the northward IMF lasted for a long period of 18 hours during this event, I run two simulations for shorter period of time to get better results. The first simulation runs from October 24 18:00:00 to October 25 10:30:00 UT to cover the time period during which Cluster moved from dayside to the plasma sheet. The second simulation runs from October 25 03:00:00 to October 25 14:20:00 UT to cover the time period during which Cluster observed the CDPS and the plasma sheet transition from cold and dense to hot and

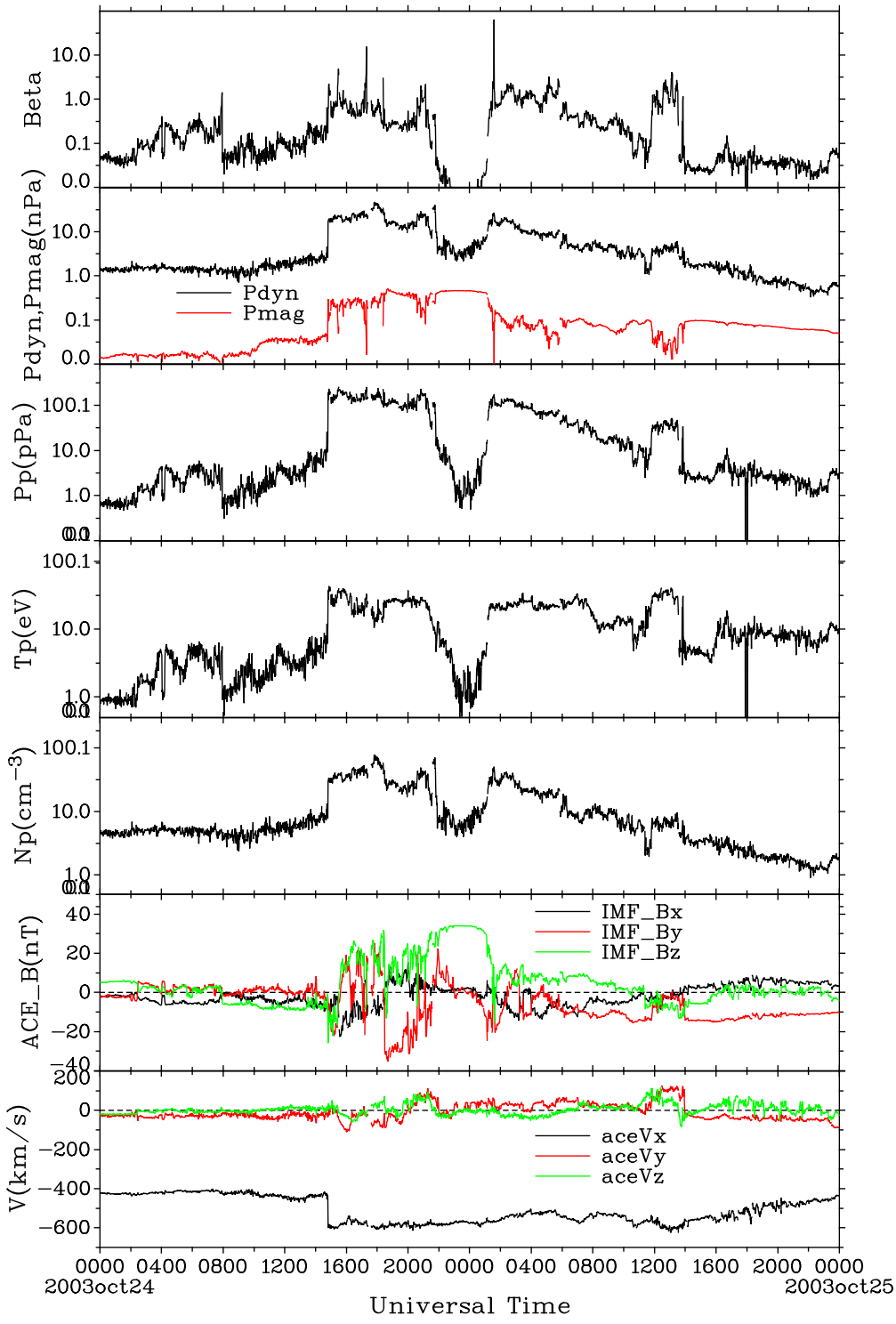

Figure 3-7: The solar wind conditions at ACE location on October 24 and 25, 2003.

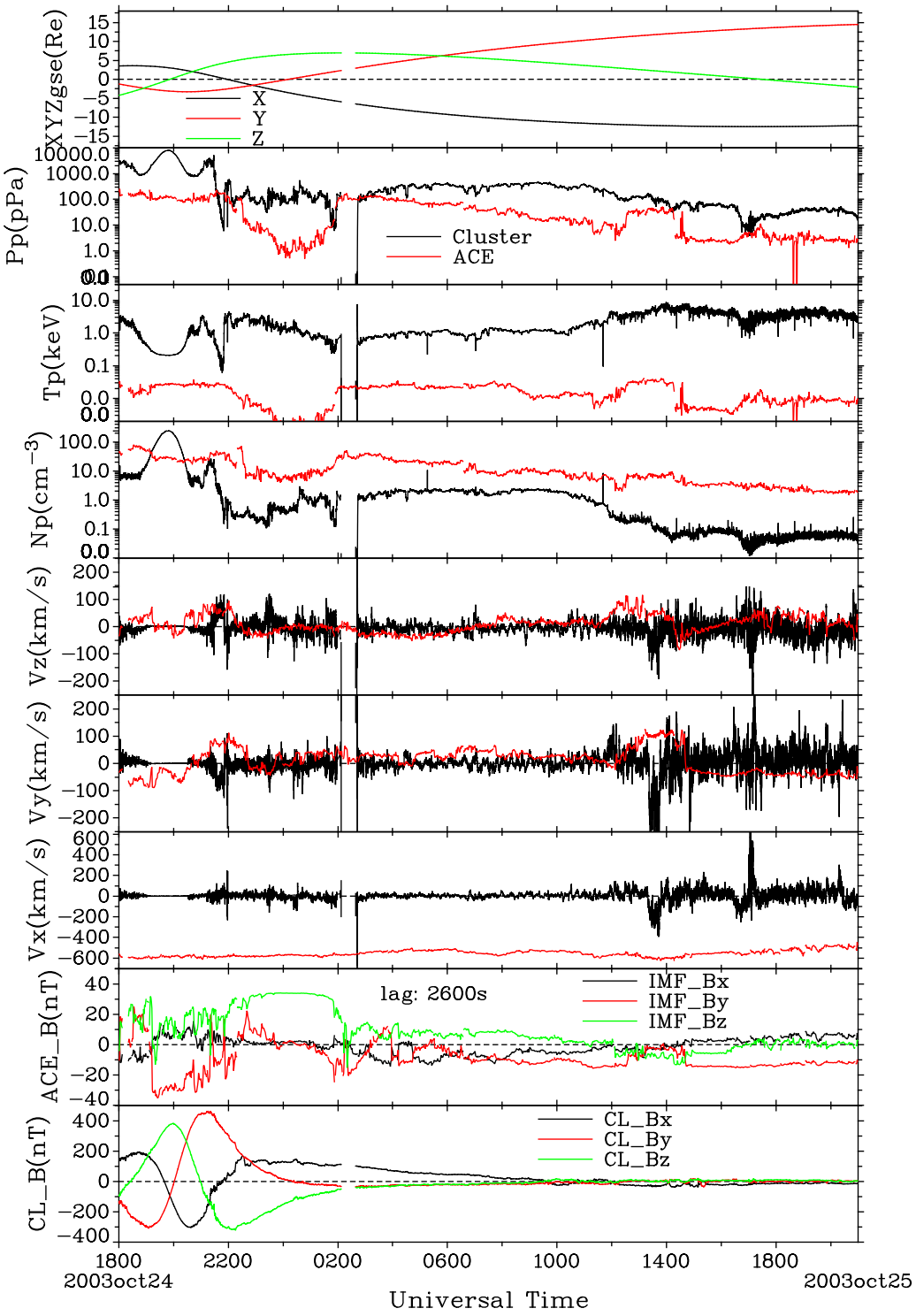

Figure 3-8: Cluster and ACE observations from 18:00:00 UT October 24 to 21:00:00 UT October 25, 2003. The top frame shows the Cluster orbit. The bottom two frames show the magnetic field measured by ACE and Cluster. In other frames, the ACE values are shown in red lines and the Cluster values are shown in black lines. The ACE observations are shifted for 2600 seconds here.

tenuous. The times for geomagnetic dipole orientations are 2003:10:25:05:00:00 and 2003:10:25:12:00:00 respectively. In these simulations, the domain is $[-25.01, 600.01]$ in x_{gse} direction and $[-40.01, 40.01]$ in y_{gse} and z_{gse} directions. The grid is $308(x) \times 200(y) \times 200(z)$ with the minimum grid spacing of 0.25 R_E. The IMF B_x is set to be zero.

3.3.4 Comparison

Figures 3-9 displays the first simulation results and the corresponding Cluster observations. The plasma velocity and the magnetic field in the first simulation match very well with the observations. Cluster is passing the ring current and radiation belt near 3-4 R_E at around 20:00:00 UT and observed a symmetric density and pressure distribution around this time. Not coupling with any model of ring current and radiation belts, the OpenGGCM simulation can not reproduce this density and pressure profile. Although OpenGGCM does not generally describe the near-Earth region ($\leq$ 6 R_E) well because of the lack of gradient and curvature drift of the hot ion population, this simulation run generates acceptable results for the first 6 hours when the Cluster was near the Earth. During the first 6 hours, the plasma temperature matches very well. This simulation reproduces the observation of CDPS when Cluster enters the plasma sheet. It reproduces almost the same value of plasma density and pressure as the observations in the CDPS. The temperature in the CDPS also matches quite well.

Figure 3-10 indicates that the second simulation also reproduces the CDPS matched well with the Cluster observations. In particular, it reproduces the plasma sheet state transition from cold and dense to hot and tenuous from $\sim$10:00:00 UT to 14:20:00 UT on October 25. During this period, the IMF changes from northward to dawn-dusk-ward and to southward.

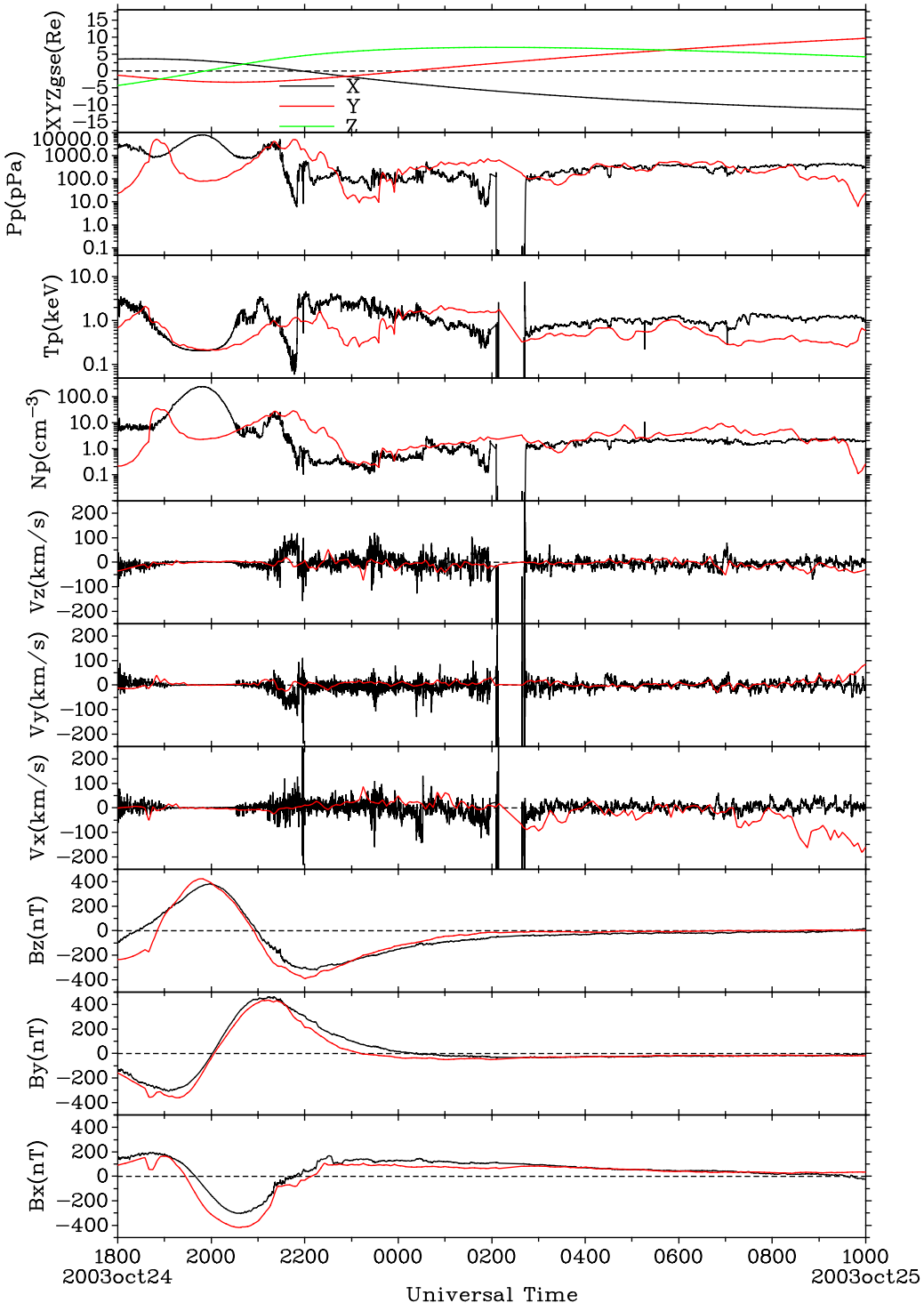

Figure 3-9: Simulation results vs Cluster observation from 24 18:00:00 to 25 10:30:00 UT in October 2003. The observations are shown with black lines and the corresponding simulation results are shown with red lines.

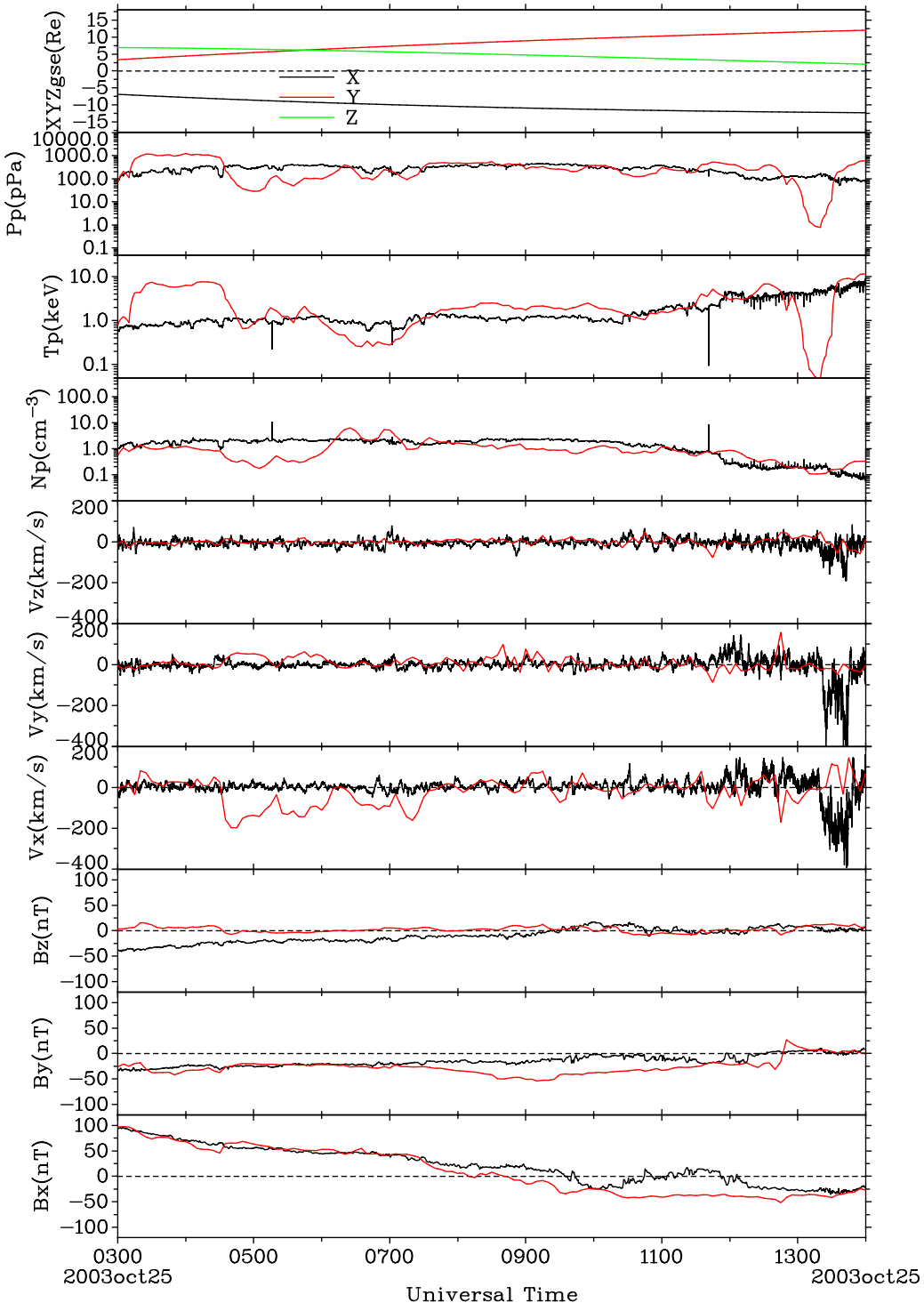

Figure 3-10: Simulation results vs Cluster observation from 25 03:00:00 to 25 14:20:00 UT in October 2003. The observations are shown with black lines and the corresponding simulation results are shown with red lines.

3.4 Summary and Discussion

Long duration events of nearly pure northward IMF are rare. The October events in 2003 therefore provide an excellent opportunity to test and extend the models.

Capturing of magnetosheath plasma by high-latitude reconnection has been first proposed by *Song and Russell* [1992] to explain the formation of LLBL under northward IMF conditions. In this model, IMF flux tubes pass through the subsolar point where the solar wind is almost stagnant. Reconnection then occurs for such flux tubes tailward of the cusps in both hemispheres. This model also describes the process of sinking in and the reorientation of the newly created closed flux tubes in the magnetosphere. Figure 3-6 shows a very similar process. The to-be-reconnected IMF flux tube first drapes over the dayside magnetopause. Once reconnected, it sinks and contracts into the magnetosphere. Subsequently it sweeps around the flank, and is convected tailward at the same time. During this process, the plasma in the southern (northern) part of the flux tube is pulled northward (southward) and sunward. *Song and Russell* [1992] did not discuss the sinking process in detail. Figure 3-6 indicates that magnetic tension plays a dominant role because the flux tubes first straighten out just after reconnection occurs.

The magnetosheath plasma near the subsolar region is cold, dense and almost stagnant. As the plasma is captured and transported to the tail, it is moderately heated near the reconnection site, and the temperature is just below 1 keV as shown in Figure 3-5. The density in the captured flux tubes is ultimately lower than the magnetosheath density. A possible reason is that the captured plasma expands in the parallel direction toward the Earth along the flux tube, and in perpendicular direction to enlarge its volume. In spite of this, the density is still greater than 1 cm^{-3} throughout. After entering the magnetosphere, the plasma flow speed stays small except that there is a small bump near the reconnection site as shown in the

velocity panel of Figure 3-5. Therefore the CDPS is characteristic of cold, dense and almost stagnant plasma. The values of temperature, density and low flow speed for the captured plasma are in good agreement with CDPS observations for this event.

The simulation shows that cusp reconnection and the associated capture of magnetosheath plasma is sufficient to produce a cold dense plasma sheet. Kelvin-Helmholtz mediated diffusion has also been suggested as a possible entry process (*Fairfield et al.*, 2000). In the simulations presented here, I do not observe any K-H waves at the dayside or flank magnetopause. This could be either due to the fact that the K-H waves are stable during the prevailing conditions or because the simulation does not resolve K-H waves sufficiently. In future studies, with higher numerical resolution, we will hopefully be able to answer this question.

The simulation results for the first event on October 23, 2003 indicates that OpenGGCM can reproduce not only the CDPS, but also the observed plasma sheet state transition from hot tenuous state to cold dense state. The simulation results for the second event on October 24/25, 2003 also show that OpenGGCM can not only reproduce the CDPS, but that the simulation also reproduce the observed plasma sheet state transition from the cold dense state to the hot tenuous state. Therefore, the OpenGGCM can be used with confidence to study the formation and the depletion of CDPS and its related magnetospheric properties.

CHAPTER 4

SUPERDENSE PLASMA SHEET

4.1 Introduction

The majority of CDPS observations are made from ∼10 R_E to ∼30 R_E in the mid-tail (*Fujimoto et al.*, 2002). The very weak convection that exists during northward IMF in the inner magnetosphere region and geosynchronous orbit does not usually allow cold dense plasma to penetrate. However, cold and very dense plasma is occasionally observed at the geosynchronous orbit by the Magnetospheric Plasma Analyzer (MPA) instruments on board the Los Alamos satellites (*Borovsky et al.*, 1997).

Borovsky et al. [1997] showed that the plasma sheet at geosynchronous orbit has densities in the range 0.4 - 2.0 cm^{-3} , with ∼6% of plasma observations with density higher than 2.0 cm^{-3}, which they classified as superdense plasma. The ion temperature of the superdense plasma ranges from 5 to 20 keV. The superdense plasma sheet (SDPS) is found to be associated with a particular temporal pattern of Kp: Kp increasing after it has been low. The duration of a superdense plasma sheet is typically 12 to 18 hours at geosynchronous orbit.

In a survey of the superdense events observed by MPA instruments, *Thomsen et al.* [2003] found that a superdense plasma sheet can occur under one of the following two conditions: (1) a sudden southward IMF that follows an extended interval of northward field, and (2) a very strong magnetospheric compression caused by a large increase in the solar wind dynamic pressure, also under conditions of northward IMF. They also suggested that, under condition (1), an southward turning of IMF causes

the cold dense plasma sheet formed in the mid-tail during the previous northward IMF period to be pushed toward the geosynchronous orbit.

In the statistical studies performed using MPA measurements for the period 1990-2004, *Lavraud et al.* [2005a; 2006a] reports the observation of two distinct cold ($T <$ 5 keV), dense ($N > 2$ cm^{-3}) ion populations at geosynchronous orbit. The first population is observed in the midnight region of geosynchronous orbit. The second population is detected on the dawn side of geosynchronous orbit. No such cold, dense population is observed on the dusk side of geosynchronous orbit on a frequent basis. The ion population is observed at midnight after the IMF has been northward for some time and is convected inward toward geosynchronous orbit after an observed mild southward turning of the average IMF. It is suggested that the source of the midnight population is the cold, dense plasma sheet (CDPS). The dawn-side cold and dense ion population is associated with previously strong southward IMF and consequently occurs during substantial geomagnetic activity.

In this chapter the focus is on the superdense plasma sheet whose formation is related to the cold dense plasma sheet. I investigate a superdense plasma sheet event classified in the paper of *Thomsen et al.* [2003] as an event that occurs under the condition (1) stated above. Michelle Thomsen and Benoit Lavraud at Los Alamos National Laboratory provided the MPA data and also provided the analysis of the MPA data and Cluster data. I run the corresponding simulation. Based on the simulation that produces the superdense plasma sheet in the near-earth region during this event, I study in detail the process that forms the SDPS.

4.2 Event Observations

4.2.1 Event overview

Figure 4-1 summarizes this event and shows time lines for observations. After ∼20 hours of strong northward IMF, the southward IMF arrived at the magnetopause at ∼22:54:00 UT September 14, 2001. The MPA instrument on LANL01a observed the arrival of the superdense plasma sheet at ∼23:22:00. Before the arrival of southward IMF, the CDPS had existed for some time at the Cluster location. The CDPS disappeared at 00:10:00 the next day, ∼1 hour and 16 minutes later after the arrival of southward IMF. The NASA IMAGE spacecraft records an auroral substorm event at 23:52:24 UT September 14, 2001. Ground magnetometers observed a disturbance beginning at ∼00:03:00 UT, and detected the maximum disturbance at ∼00:50:00 the next day.

During this event, from ∼22:40:00 UT on September 14 to ∼02:00:00 UT on September 15, LANL97a was on the dawn side from ∼03:00:00 LT to ∼07:00:00 LT, and LANL90 was on the dusk side from ∼20:00:00 LT to ∼24:00:00 LT. LANL01a was near the noon-midnight meridian from ∼23:00:00 LT to ∼02:30:00 LT. All the satellites were near the equatorial plane on the geosynchronous orbit. The Cluster spacecrafts were ∼20 R_E in the tail and near both the equatorial plane and the noon-midnight meridian.

4.2.2 Solar wind conditions

On September 14, 2001, ACE observed a long period (∼20 hours) of northward interplanetary magnetic field followed by a IMF southward turning at ∼21:52 UT. The southward IMF arrived at the magnetopause approximately at ∼22:54 UT, with a ∼3720 seconds lag. The arrival time at the magnetopause is estimated using the data from Wind. Wind spacecraft was fortuitously located at GSE(51.2, -42.7, 3.7) R_E

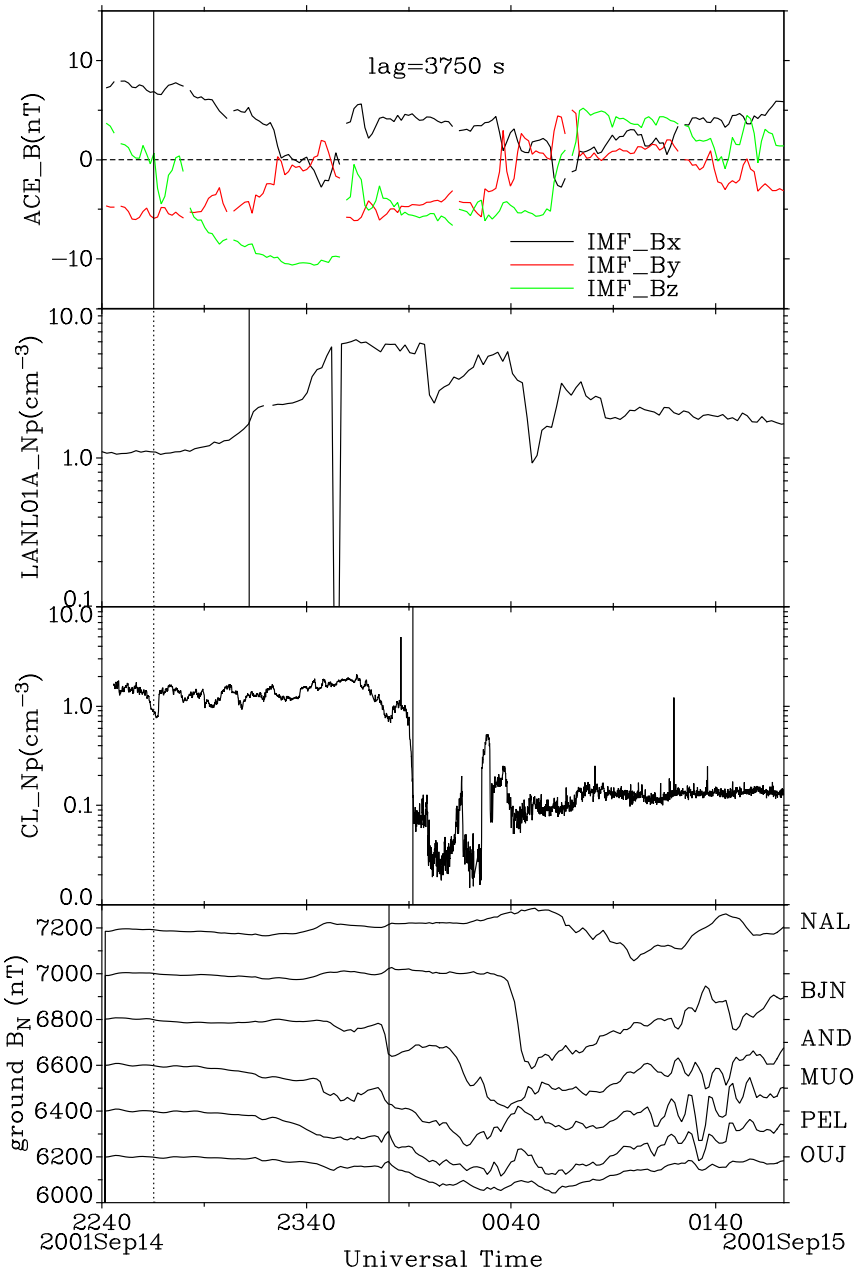

Figure 4-1: Overview of the SDPS event from 22:40 UT on September 14 to 02:00 UT on September 15, 2001. Shown from top to bottom are shifted IMF measured at ACE, proton number density measured by LANL01a MPA instrument, plasma density measured by Cluster, and the northern component of the ground magnetic field measured by ground stations.The solid vertical lines from top panel to bottom panel indicate the IMF southward turning at magnetopause, the arrival of SDPS at the geosynchronous orbit, the disappearance of CDPS at Cluster, and the beginning of ground magnetic field disturbance, respectively.

at 22:45:00 UT, and was observing the southward IMF turning at this time. It also observed the long period of northward IMF before the southward IMF arrival. Thus, the solar wind at ACE is correlated with the solar wind at Wind during this event. This southward IMF lasted for ∼2.4 hours. During this period of southward IMF, the solar wind speed was ∼460 km/s, and the plasma number density jumped from ∼5 cm^{-3} to ∼20 cm^{-3}.

4.2.3 Cluster observations

The Cluster observations are shown in Figure 4-3. On September 14, Cluster has no data before 22:40 UT. Cluster observed a cold dense plasma sheet from 22:40 UT on September 14 to 00:10 UT on September 15. At 00:10 UT on September 15, ∼76 minutes after the IMF southward turning, Cluster detected a sudden change from CDPS to hot tenuous plasma sheet. This suggests that Cluster suddenly exited the CDPS. Before the CDPS disappearance, the magnetic field in the CDPS was highly stretched. Cluster observed a substorm growth phase from ∼23:00 to ∼00:15 UT during which the magnetic field builds up and stretches further. The substorm onset occurs around ∼00:15 UT. Shortly after exiting the CDPS, a burst of sunward hot plasma flows with speed up to 800 km/s is observed at Cluster at 00:25:00 UT on September 15, indicated by the vertical line in Figure 4-3. Since the Cluster was moving from south to north, it is most likely that Cluster exited the northern proper of the CDPS, and then entered the hot tenuous plasma sheet. The magnetic field was then dipolized immediately after the plasma flow burst. Therefore, it is most likely that magnetotail reconnection occurred at the tailward side of the Cluster.

4.2.4 Observations at nightside geosynchronous orbit

During this event, three LANL satellites were on the nightside well positioned for the observation of the SDPS. As shown in Figure 4-4, one satellite was near midnight

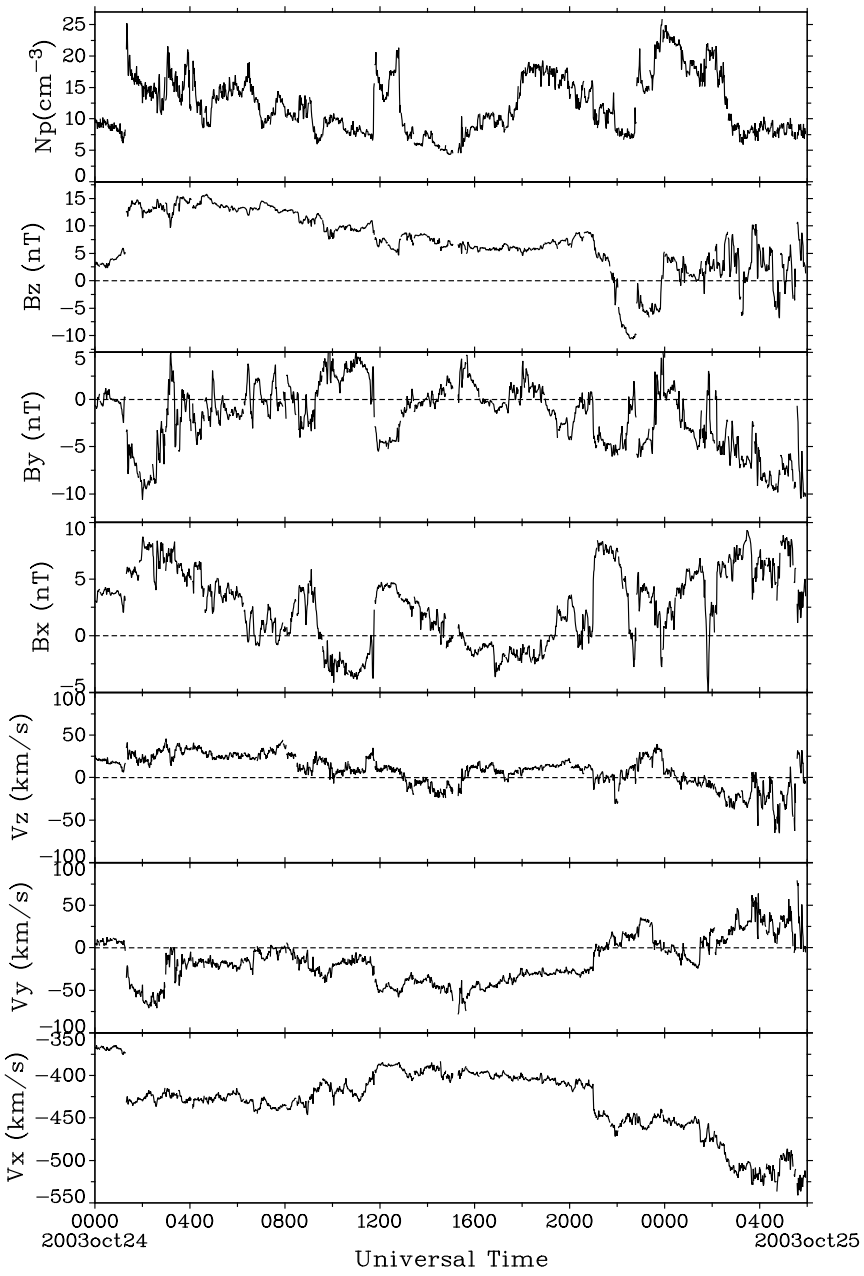

Figure 4-2: Solar wind conditions at ACE location from September 14 00:00:00 to September 15 06:00:00, 2001. Shown properties from top to bottom are plasma number density, B_z, B_y, B_x, V_z, V_y, and V_x, all in GSE coordinates.

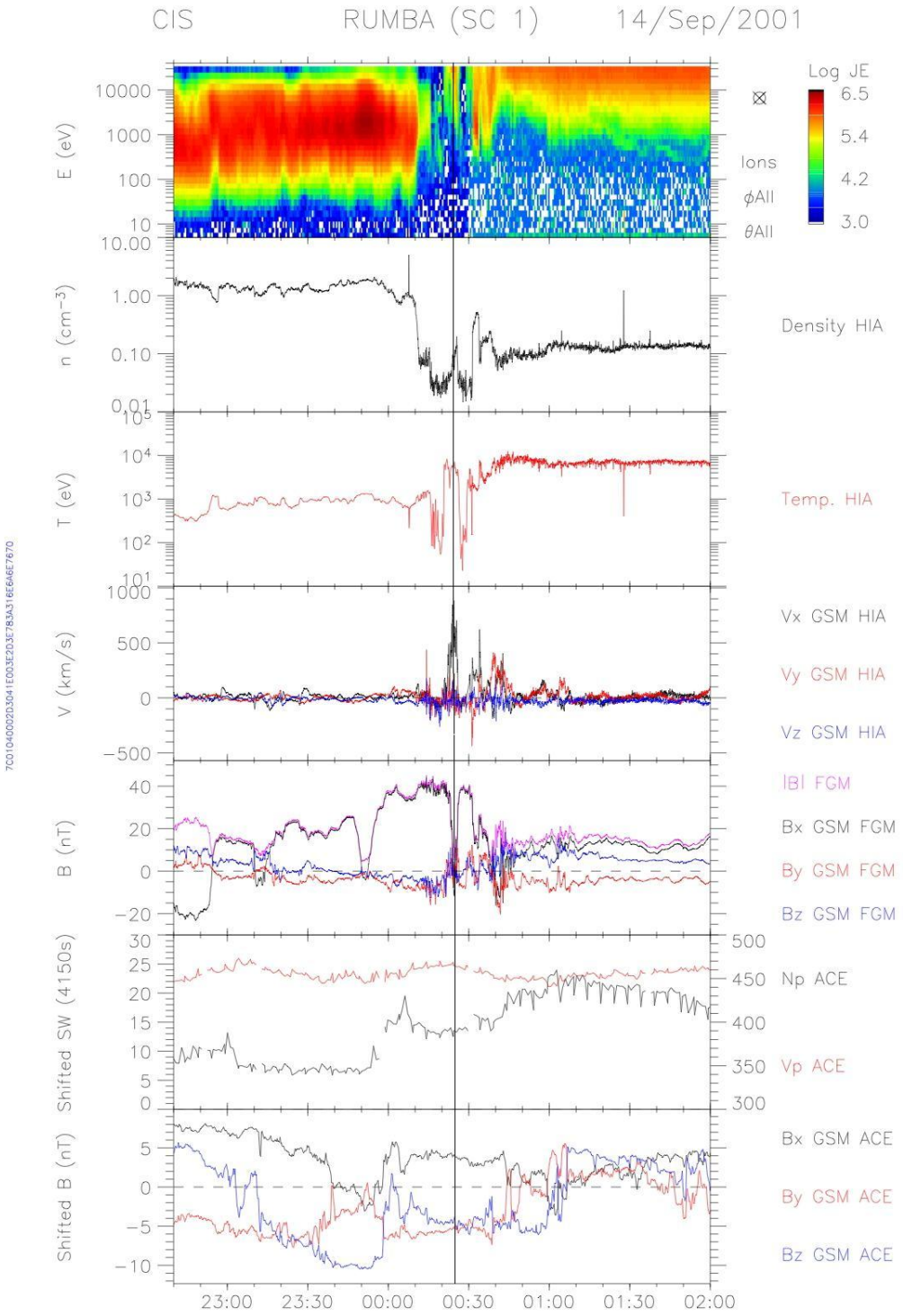

Figure 4-3: Cluster observations from 22:40:00 UT September 14 to 02:00:00 UT September 15, 2001. Shown from top to bottom are energy spectrum of ion flux, plasma density, plasma temperature, plasma velocity, magnetic field, all at Cluster, shifted solar wind density and speed at ACE, and shifted IMF at ACE.

and the other two were located at the dawn side and the dusk side, respectively. At ∼23:22, ∼28 minutes after IMF southward turning at the magnetopause, LANL-01A first detected high density (∼2 cm^{-3}) plasma near local midnight. At ∼23:40, LANL-97A and LANL 1990-095 began to detect similar plasma material at the dusk and the dawn side, respectively. The plasma then became superdense and the much colder for ∼40 minutes. At ∼23:45, ∼51 minutes after IMF southward turning at the magnetopause, LANL-01A began to detect superdense (∼6 cm^{-3}) plasma near local midnight. At ∼23:50, LANL-97A and LANL 1990-095 also began to detect the superdense plasma material at the dusk and the dawn side respectively. During this period of high density and super-high density plasma, the magnetic field at 6.6 R_E in the nightside was highly stretched, as indicated by the magnetic field elevation angle (θ) shown in Figure 4-4. The azimuthal flow speed increased significantly when the superdense plasma passed by the Cluster spacecrafts. The dipolization of the tail field at geosynchronous orbit was observed at 00:15 UT. After that, the azimuthal speed became almost stagnant again, and the superdense plasma gradually disappeared. The superdense plasma disappeared faster in the duskside than in the dawnside and near the midnight.

The timing of density profiles and the azimuthal flow speed for these three LANL spacecraft show that the cold dense plasma accesses the geosynchronous orbit at midnight first and then propagates to the dawn and dusk sides. The magnetic field started to stretch at all three spacecraft prior to and during CDPS observation. Before the substorm onset, enhanced convection brought dense plasma to geosynchronous orbit, but no flows were observed at the Cluster location. After the substorm onset at ∼00:15 UT, the plasma sheet observed at Cluster became hot and tenuous.

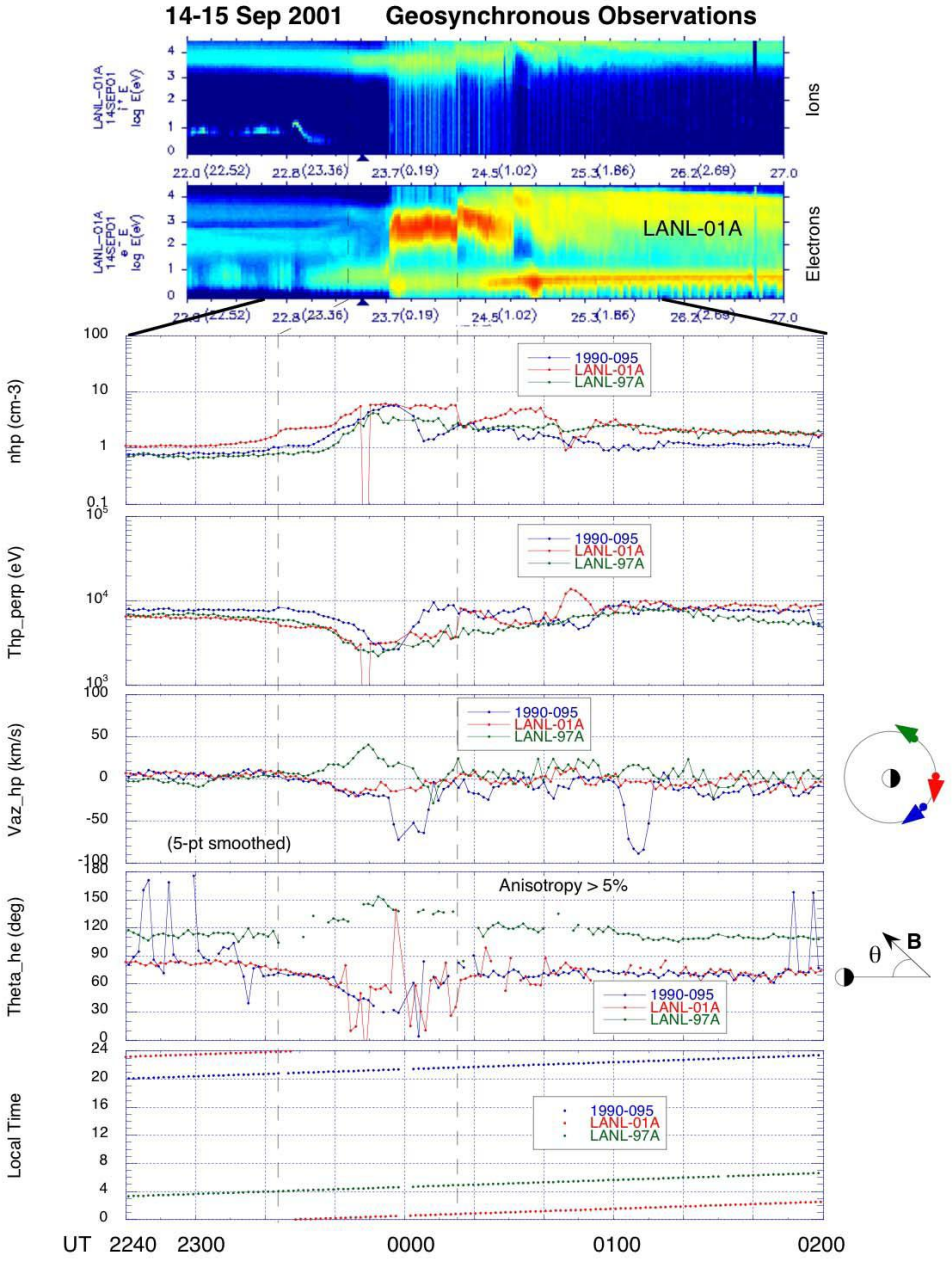

Figure 4-4: Nightside geosynchronous observations from 22:40:00 UT on September 14 to 02:00:00 UT on September 15, 2001. There are three LANL satellites, LANL97A, LANL01A, and LANL90, in the nightside during this time. Shown from top to bottom are the energy spectrum of ion and electron flux at LANL01A, proton density, plasma perpendicular temperature, plasma velocity along the geosynchronous orbit, magnetic field direction, and satellites' local time positions.

4.2.5 Related auroral observations

The NASA Imager for Magnetopause-to-Aurora Global Exploration (IMAGE) spacecraft observes an auroral substorm event commencing at 23:52:24 UT September 14, 2001 as shown in Figure 4-5. During the 23 hours before ∼23:00:00, the polar cap was calm and no auroral disturbances were observed (the auroral images for this time period are not shown here), as a result of the long period of northward IMF during this day. After ∼23:00:00, when the southward IMF arrives, the auroral oval started to grow slightly. At 00:10:49, the auroral oval suddenly brightens in comparison to the previous image at 23:56:29 UT. The dawn side aurora is substantially enhanced. That means a substorm onset has occurred. The electron auroral images show that the auroral substorm lasts until ∼02:00:00. It is most likely that this substorm is caused by the arrival of the southward IMF.

4.2.6 Ground magnetic disturbance

The ground magnetic disturbance related to this event, shown in Figure 4-6 and Figure 4-7, which show the northward component of the ground magnetic field measured at the "International Monitor for Aurora Geomagnetic Effects" (IMAGE) magnetometer network stations. Figure 4-8 shows the positions of the magnetometer stations. Like the auroral images, the ground measurement also shows that there was no disturbance before 23:00:00 UT during that day, corresponding to the calm day of northward IMF condition. From 23:00:00 UT to 02:00:00 UT on the next day, there was a substorm disturbance with the maximum disturbance occurring at 00:50:00 UT. The map with the locations of the ground station indicates that the stations were near the midnight local time location during this event.

Figure 4-9 shows that the Kp index had been low on September 14 during which the IMF was northward, and then Kp increased after the southward turning of IMF.

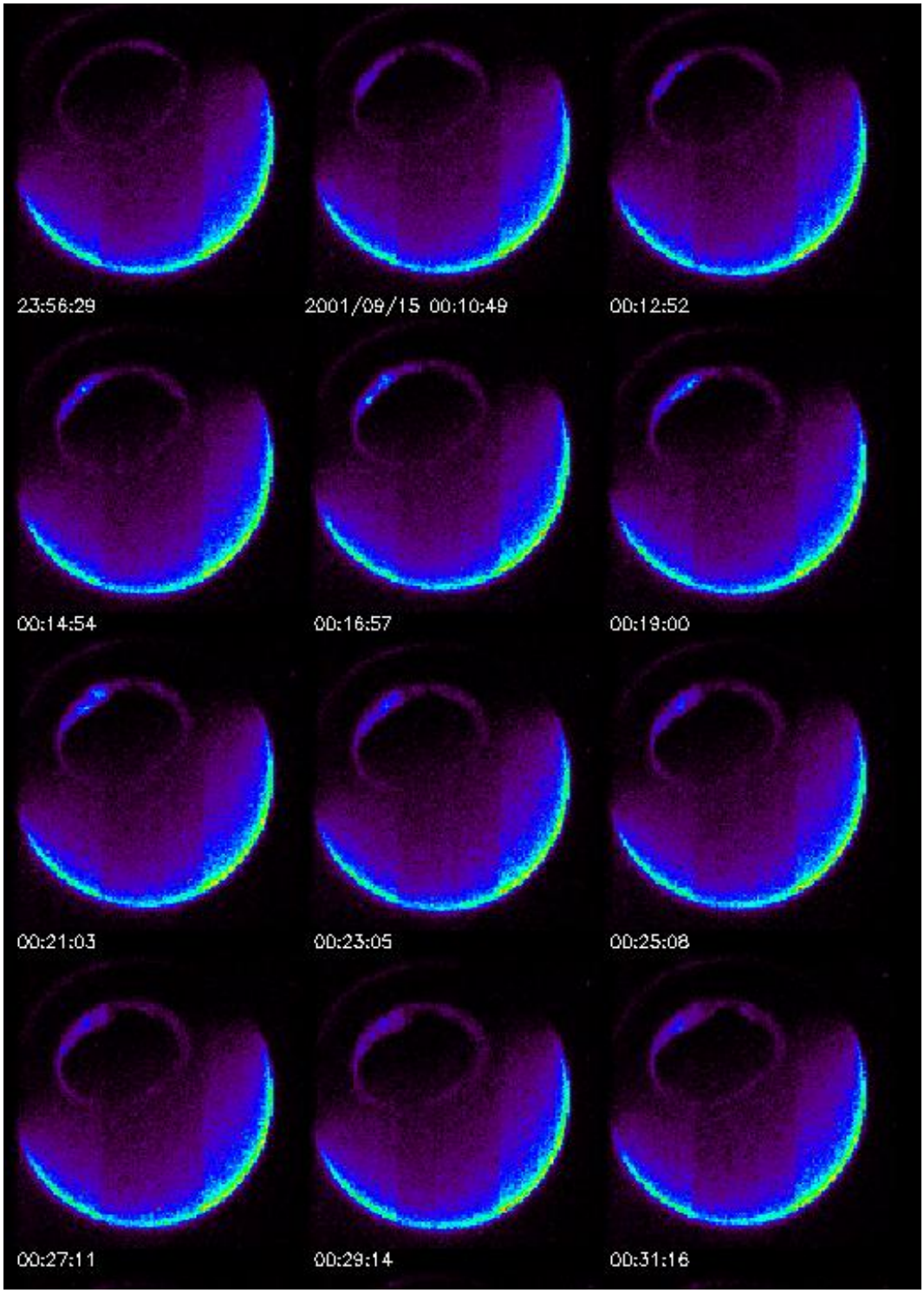

Figure 4-5: The auroral substorm on September 14, 2001 shown by NASA IMAGE SIE electron auroral images. This image is generated by NASA CDAWeb.

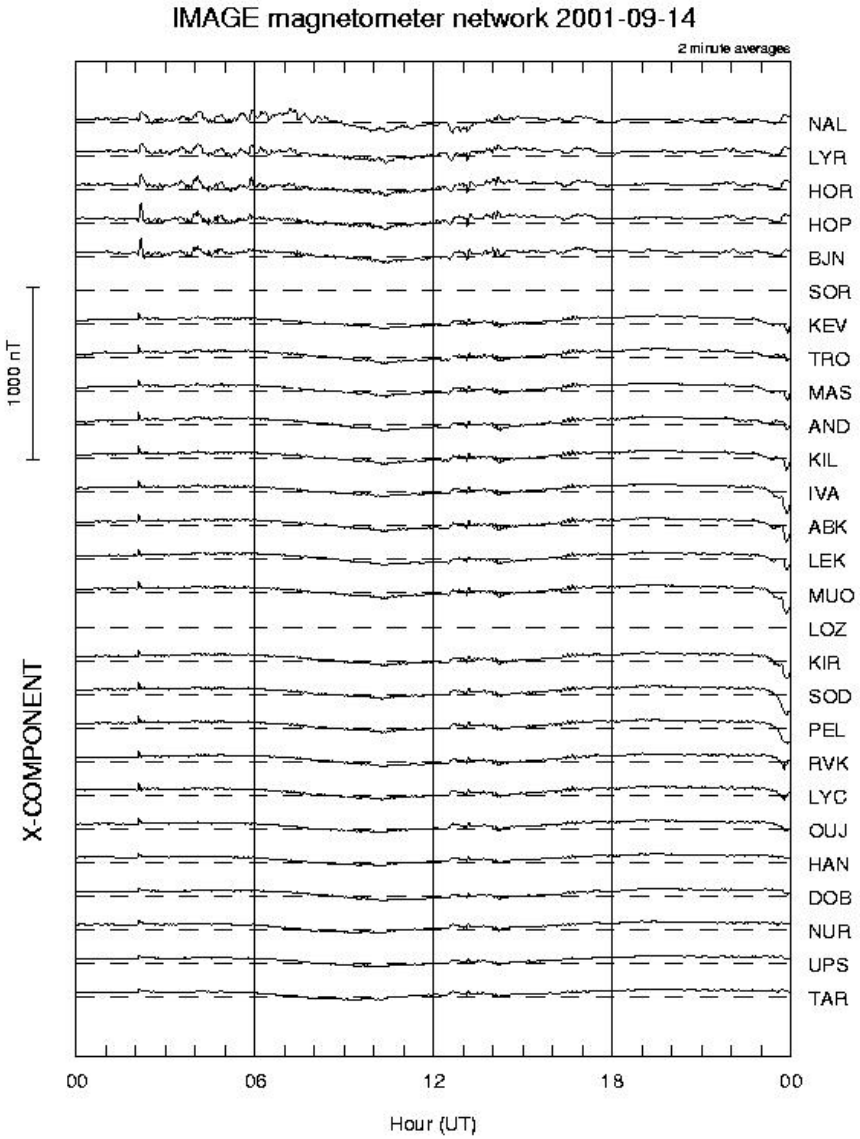

Figure 4-6: Northward component of ground magnetic field on September 14, 2001 from International Monitor for Aurora Geomagnetic Effects (IMAGE) magnetometer network. (Created from IMAGE)

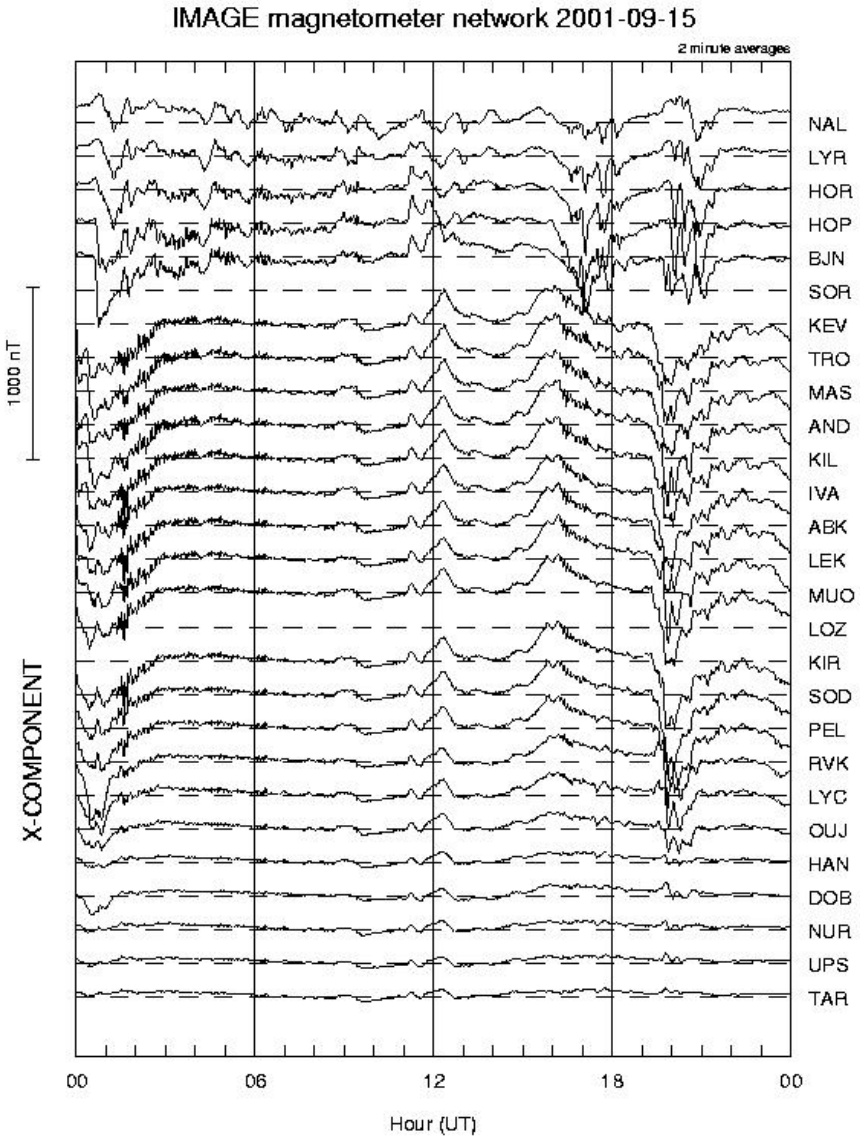

Figure 4-7: Northward component of ground magnetic field on September 14, 2001 from International Monitor for Aurora Geomagnetic Effects (IMAGE) magnetometer network. (Created from IMAGE)

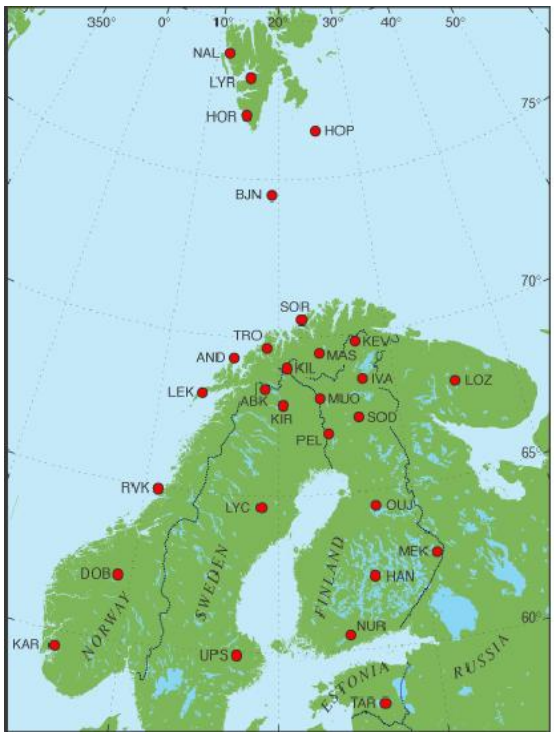

Figure 4-8: The locations of the stations in International Monitor for Aurora Geomagnetic Effects (IMAGE) magnetometer network. (Created from IMAGE)

During this event, the *Dst* index just decreased mildly, which is typical for substorm.

4.2.7 Observation summary

A summary of this SDPS event can be made from combining the analysis of the observations of ACE, Cluster and LANL spacecrafts. The IMF had been northward for $\sim$ 20 hours until 22:54:00 UT September 14 when it turned southward at the dayside magnetopause. The CDPS thus had been formed due to the long period of northward IMF. At 22:40 UT, the magnetic field at Cluster (12 R_E in the tail) begins to attain a stretched configuration. Cluster observed a substorm growth phase from $\sim$23:00 to $\sim$00:15 UT during which the tail magnetic field built up and stretched. At $\sim$23:22, the high density plasma begins to appear at 6.6 R_E at midnight, and becomes superdense for $\sim$ 40 minutes. From $\sim$ 00:15 UT on the next day, the

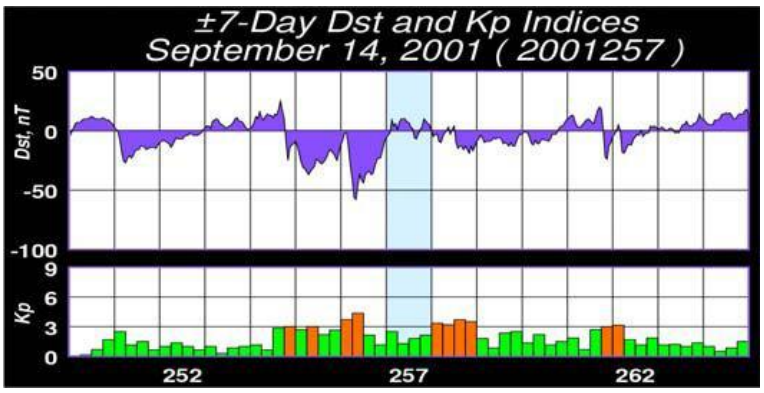

Figure 4-9: The *Dst* and *Kp* indices on days around September 14, 2001.

plasma density begins to decrease, the plasma flow slows down, and the temperature increases, returning to pre-SDPS levels. The dipolization observed at 00:30 UT by Cluster correlates with observations 15 minutes later at geosynchronous orbit. During this event, from 23:00:00 to 02:00:00, the corresponding auroral substorm and ground magnetic disturbance were also observed, as shown before.

4.3 Event Simulation

4.3.1 Simulation

An OpenGGCM simulation for this event with real time solar wind data from ACE, using minimum variance method to determine the direction of the fronts of the solar wind was performed. The simulated period ranges from 18:00:00 UT on September 14 to 02:00:00 UT on September 15. The magnetic dipole orientation is set to 2001:09:14:23:00:00 UT, the time of the southward IMF turning at the magnetopause. The simulation domain is [-600.01, 25.01]R_E× [-45.01,45.01]R_E×[-45.01,45.01]R_E in GSE coordinates.. The grid is $480(x) \times 250(y) \times 250(z)$, which is much higher resolution than in simulations for CDPS events presented in Chapter 3. The minimum grid spacing is 0.2 R_E near the dayside magnetopause region.

4.3.2 Comparison

The simulation results are compared with Cluster observations in Figure 4-10. The simulation reproduces the CDPS, but with lower temperature. The main reason is that the simulation starts with northward IMF rather than southward IMF. The southward IMF causes an increase of the average temperature of the magnetosphere to more realistic values. The more important simulation result shown in Figure 4-10 is that it reproduces the exit of Cluster from the CDPS and also reproduces the bursty plasma flows. This bursty flow, seen in the simulation, is also directed toward the Earth (V_x not shown here). The simulation also shows the stretched magnetic field during the substorm growth phase and substorm onset, and the magnetic field dipolization, as shown in the top frame of Figure 4-10.

Figure 4-10 shows that the Cluster exit from the CDPS in the simulation occurs $\sim$ 40 minutes earlier than the reality. The main reason is that the southward IMF in the simulation arrives earlier at the magnetopause by about 22 minutes. The actual southward IMF arrival time at the magnetopause is 22:54 UT, as estimated in section 4.2.2. Its corresponding time in the simulation is $\sim$22:32 UT. The discrepancy is mainly caused by the error in computing the normal vector of the IMF front by minimum variance method, as shown in 4-11. Another reason is that the location of mid-tail reconnection may be closer to Cluster in the simulation than in reality. The third reason is that the anomalous resistivity in the simulation possibly causes reconnection occur earlier than reality. A similar time difference also exists in the comparison of simulation with observations of LANL spacecrafts in Figure 4-12, 4-13, and 4-14.

The simulation reproduces the arrival of superdense plasma sheet at all the three LANL spacecraft with almost the same time difference between simulation and observations. The time difference of 30 minutes, less than the time difference for Cluster

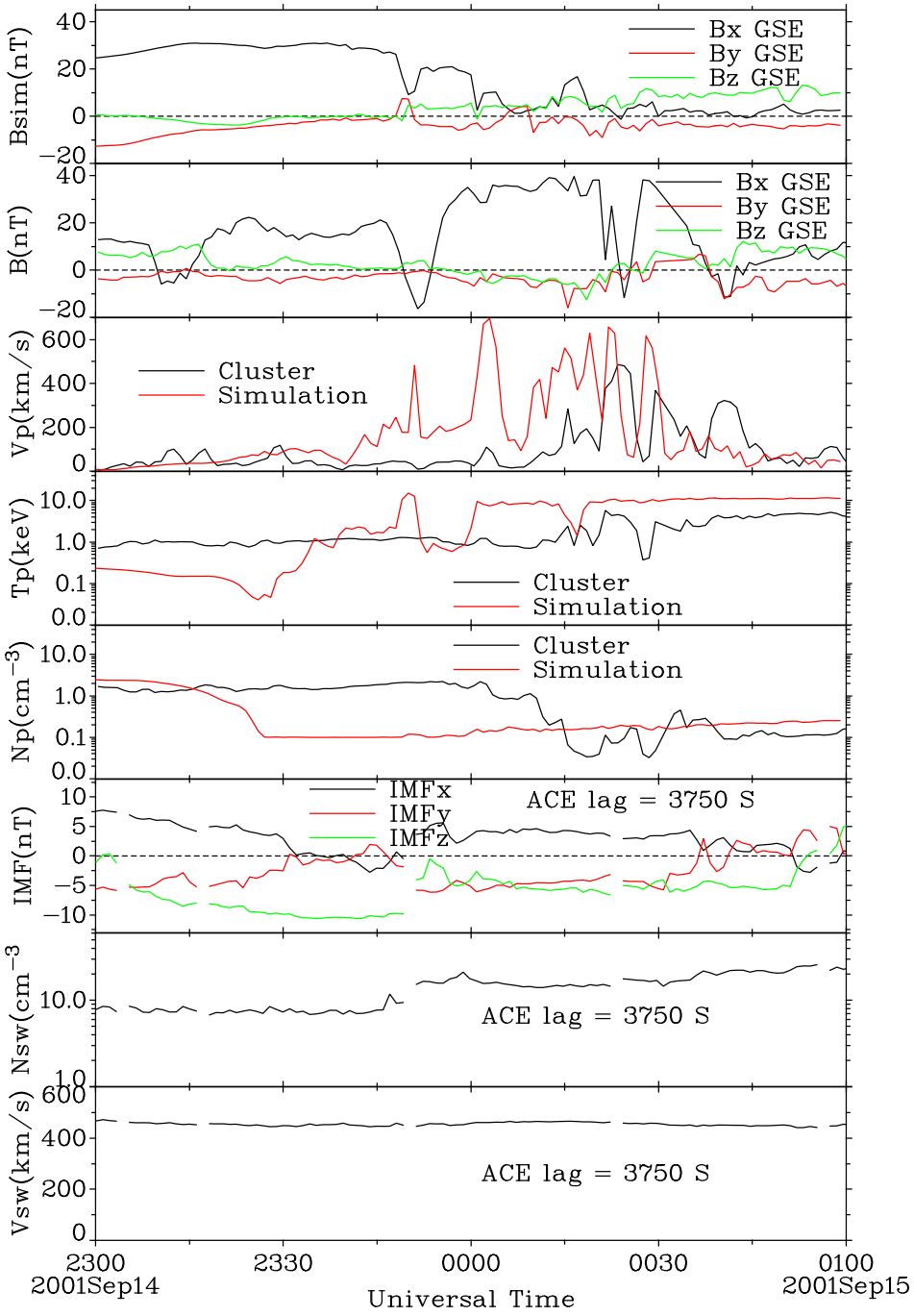

Figure 4-10: Simulation vs. Cluster observations from 23:00:00 UT on September 14 to 01:00:00 UT on September 15. The top two frames show the simulation magnetic field and observed magnetic field. The other frames show plasma flow speed, plasma temperature, and plasma density from top to bottom with red lines for simulation and black lines for observations.

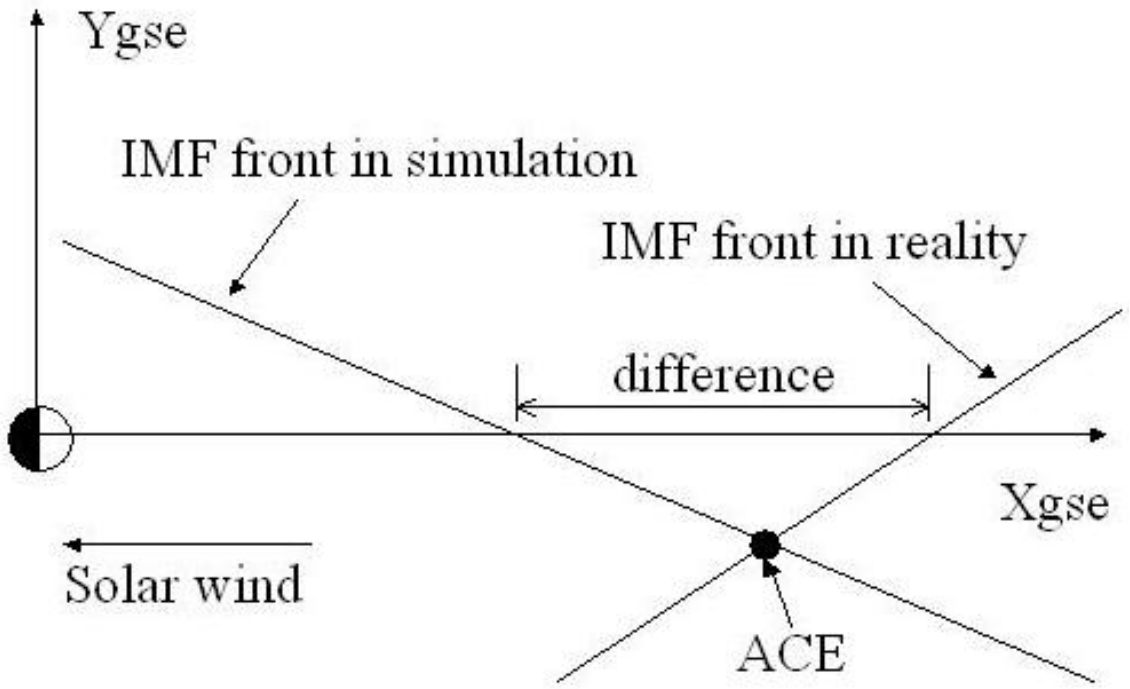

Figure 4-11: The possible IMF front in simulation and reality. The IMF front in the simulation will arrive at the magnetopause earlier than in reality for an amount of time related to the spatial difference indicated in the figure and the corresponding solar wind speed.

observation, is compatible with the time difference of southward IMF arrival time. It is possible that the precise location of mid-tail reconnection may not play a significant role in transporting the cold dense plasma to the inner magnetosphere. Although the temperature level is not in agreement with observation, it reflects the temperature change when the superdense plasma sheet arrives. It seems that the temperature in simulation is lower than the observed one before the superdense plasma sheet arrival. It is mainly due to the simulation not being started with southward IMF. After the arrival of the SDPS, the duration of the SDPS in the simulation is shorter than the observed period of the SDPS. In other words, the superdense plasma, which is also cold, depletes faster in simulation than in reality. Consequently the temperature after the depletion of SDPS in the simulation is higher than the corresponding observation. Faster depletion in the simulation is probably caused by the lack of non $\mathbf{E} \times \mathbf{B}$ drifts in the model.

Comparing to observations from LANL01A at the midnight location, the superdense plasma sheet disappears faster in the simulation. The flow speed is also higher in the simulation. The simulation result for LANL90 at the dusk side matches the observations more closely. However, the density in the simulation is higher when superdense plasma is accumulating, and also decreases faster than observation. Comparing to observations of LANL97A in the dawn side, the superdense plasma disappears faster in the simulation beginning at ∼23:40 UT. The transition from the hot tenuous state to the superdense plasma state is out of the time range shown in Figure 4-14. After ∼00:30 UT in the simulation, another piece of superdense plasma sheet seems to appear again in the dawn side. We will discuss the discrepancy between the observations and the simulation after we discuss the detail superdense plasma sheet formation process.

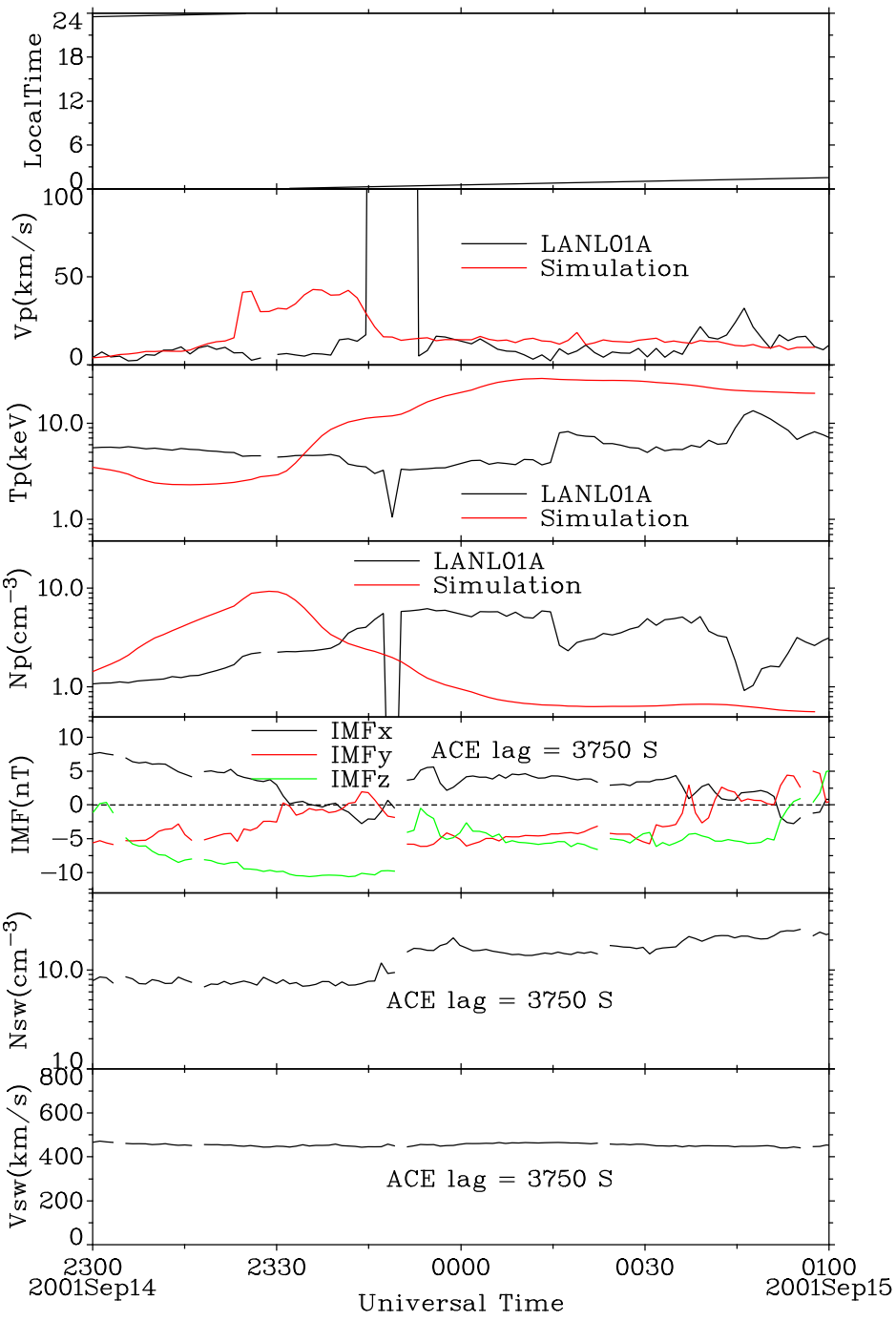

Figure 4-12: Simulation vs. LANL01A observations from 23:00:00 UT on September 14 to 01:00:00 UT on September 15. The top frame shows the local time position of LANL01A. The next 3 frames from top to bottom show plasma flow speed, plasma temperature, and plasma density, with red lines for simulation and black lines for observation. The other frames from top to bottom show the IMF, solar wind density, and solar wind speed, with a time lag of 3750 seconds.

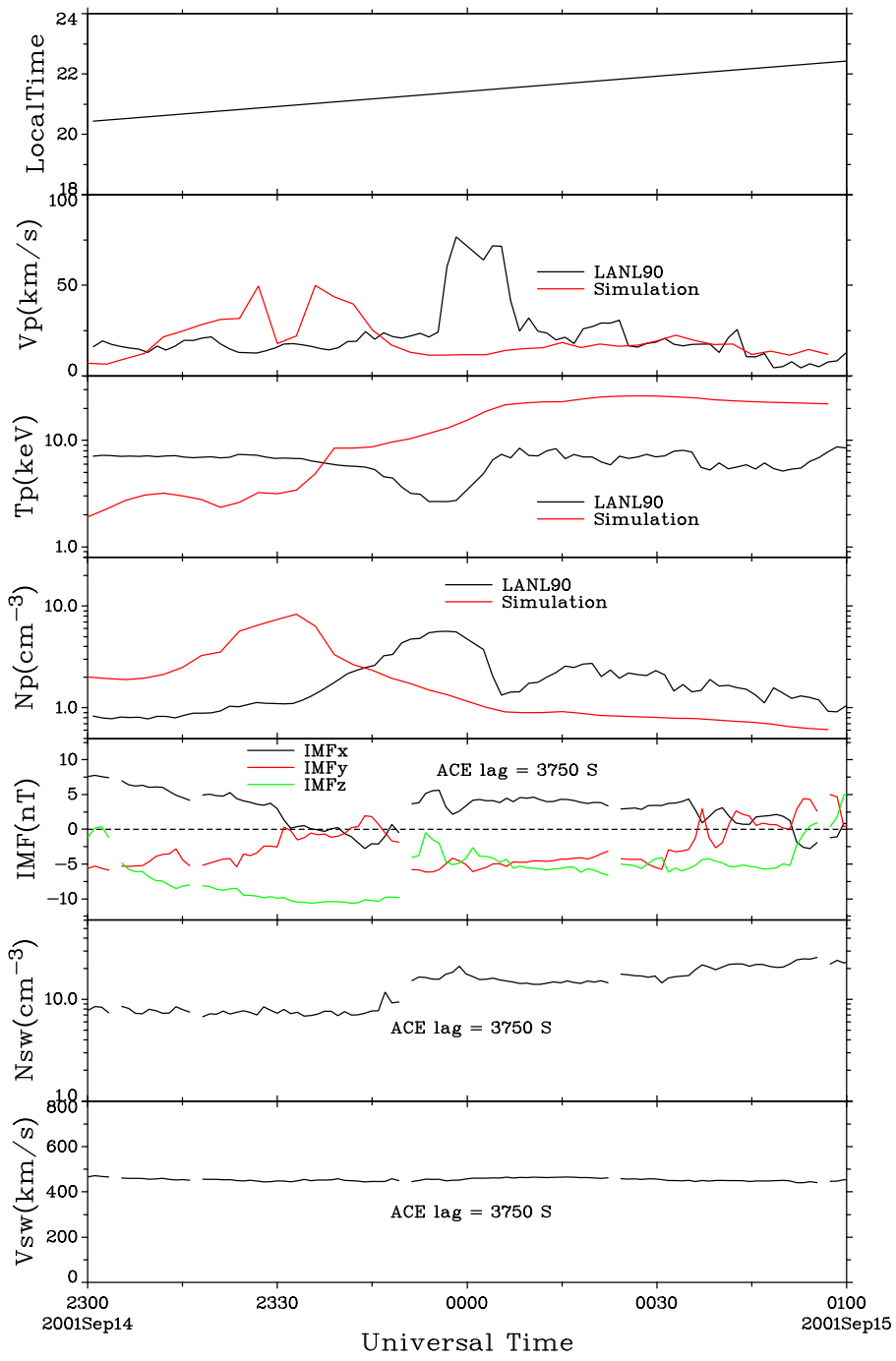

Figure 4-13: Simulation vs. LANL90 observations from 23:00:00 UT on September 14 to 01:00:00 UT on September 15. The top frame shows the local time position of LANL90. The next 3 frames from top to bottom show plasma flow speed, plasma temperature, and plasma density, with red lines for simulation and black lines for observation. The other frames from top to bottom show the IMF, solar wind density, and solar wind speed, with a time lag of 3750 seconds.

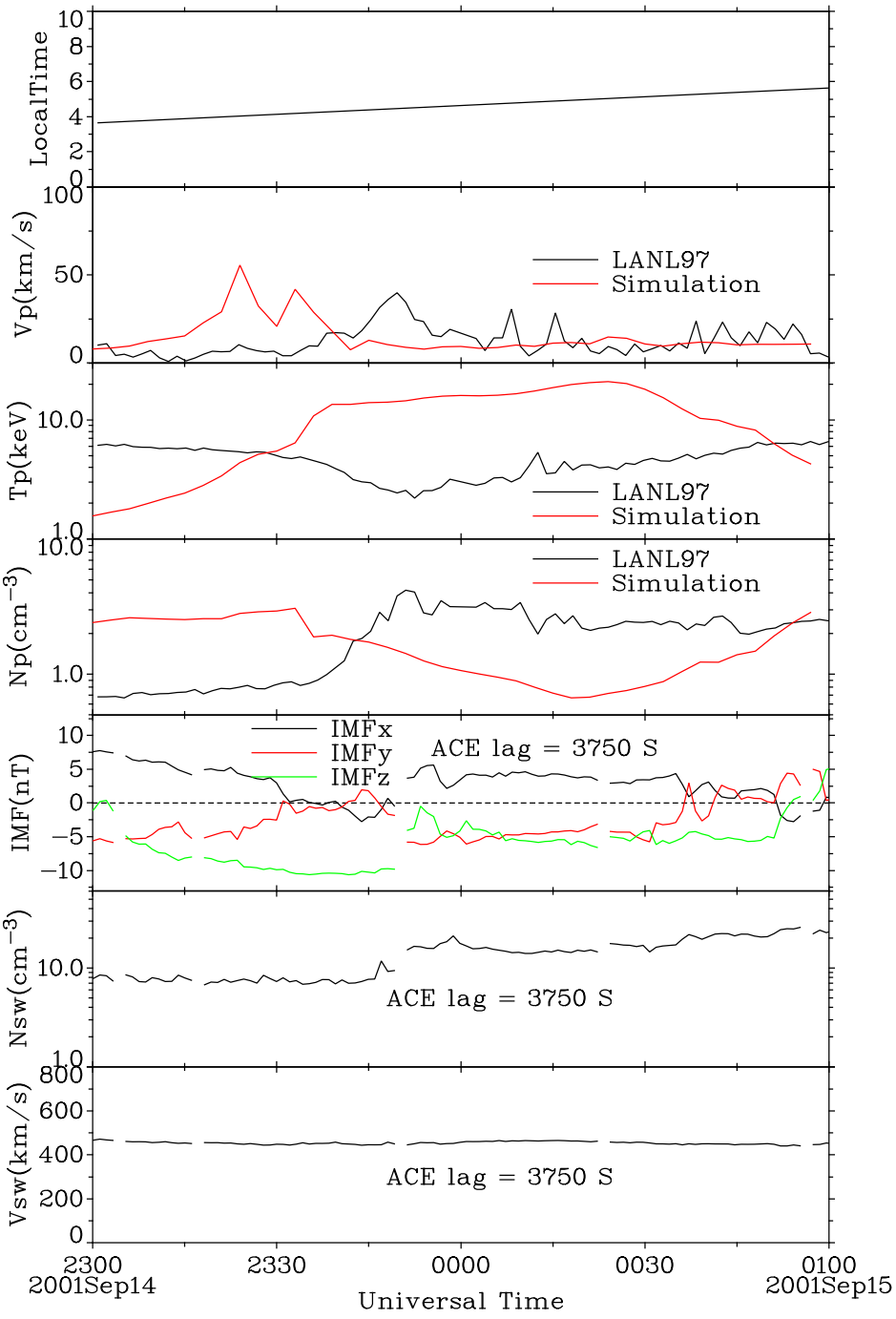

Figure 4-14: Simulation vs. LANL97A observations from 23:00:00 UT on September 14 to 01:00:00 UT on September 15. The top frame shows the local time position of LANL97A. The next 3 frames from top to bottom show plasma flow speed, plasma temperature, and plasma density, with red lines for simulation and black lines for observation. The other frames from top to bottom show the IMF, solar wind density, and solar wind speed, with a time lag of 3750 seconds.

4.3.3 Formation of the SDPS

The comparison between the simulations results and the observations of Cluster and LANL spacecrafts indicates that the simulation reproduces the main features of the SDPS event, including the formation and disappearance of cold dense plasma sheet at Cluster, and the arrival of superdense plasma sheet at the three LANL satellites on geosynchronous orbit. By analyzing the simulation results, the detailed mechanism of the SDPS formation can be found. The following Figures 4-15 - 4-20 showing density, V_x, V_z and B_z values on the equatorial plane or the noon-midnight meridian at different moments display the formation process of the superdense plasma sheet. The following discussion is based on these simulation results.

At 22:32 UT in the simulation, the southward IMF arrives at the magnetopause, as shown by the first appearance of negative B_z in frame (a) of Figure 4-19 and frame (a) of Figure 4-20. At this moment, the CDPS has been in existence for an extended period. Frame (a) of Figure 4-16 and frame (a) of Figure 4-15 show that the average plasma density of the plasma sheet is high, at least $\sim$1.0 cm^{-3}, after the long period of northward IMF. In frame (a) of Figure 4-16, there are two pieces of CDPS extending from the dusk flank at $\sim x_{gse}(-20 - -30)$ R$_E$ and from the dawn flank at $\sim x_{gse}(-10 - -20)$ R$_E$, called CDPSa and CDPSb here respectively. There are also other two pieces of CDPS near the noon-midnight meridian just above or below the equatorial plane, which I call CDPSc and CDPSd in the following descriptions, as shown in frame (a) of Figure 4-15. The plasma flow is almost stagnant in the plasma sheet at this time (frame (a) of Figure 4-17).

At 22:53 UT, the southward IMF has compressed the magnetotail for $\sim$20 minutes. Consequently, CDPSc and CDPSd are pushed toward the equatorial plane, as shown by frame (b) of Figure 4-15, and their dense plasma material appears on the equatorial plane near $x_{gse} = -12$ R$_E$, as shown by frame (b) of Figure 4-16. For convenience of

discussion, this portion of cold dense plasma sheet is called CDPSe.

Frame (c) of Figure 4-16 and frame (c) of Figure 4-15 indicate that the cold dense plasma material continues to accumulate around (-12,0,0)R_E in GSE coordinates, and that CDPSe is growing as a result of the compression of tailward convecting open flux tubes that are newly created at the dayside magnetopause. At 23:16 UT, one part of the plasma in the plasma sheet is convecting earthward and the other part is flowing tailward. The separating boundary is roughly indicated by the boundary between the light blue region and the green region in the magnetotail as shown in frame (c) of Figure 4-17. This is in the substorm growth phase. At this moment, the northern part of plasma sheet is moving southward, and the southern part of plasma sheet is moving northward, as shown in frame (c) of Figure 4-18, as a result of the compression.

At around 23:22 UT, near Earth tail reconnection occurs, making the onset of the substorm (*Baker et al.*, 1996). The plasma sheet is more compressed at around 15 R_E in the tail, and becomes very thin there (frame (d) of Figure 4-15). CDPSe becomes much denser and its earthward convection is accelerating. As it is convecting earthward, it slows down near the inner magnetosphere region. Thus CDPSe is also compressed earthward and the density increases significantly when it approaches geosynchronous orbit (frame (d)'s of Figure 4-16 and Figure 4-17). At this point the CDPSe becomes the superdense plasma sheet. The tailward moving newly reconnected field lines make it more clear that the B_z is southward in the tailward flowing plasma in the plasma sheet (frame (d)'s of Figure 4-19 and Figure 4-20).

At around 23:29 UT, the near-tail reconnection rate becomes very high as indicated by the high plasma bulk flow speed shown in frame (e) of Figure 4-17, and the enhanced plasma convection toward the equatorial plane as shown in frame (e) of Figure 4-18. Frame (e) of Figure 4-20 shows that B_z is southward in the tailward

flowing plasma in the plasma sheet. The CDPSe, now a piece of super dense plasma sheet, flows near geosynchronous orbit. The CDPSe is not just a narrow flow channel that first flows to the midnight region then diverts to dawn and dusk, as one might conclude from the observations of the LANL spacecrafts. Rather, CDPSe extends over a wide range in local time, and flows directly sunward (Figure 4-16).

In Figure 4-14, the plasma detected by LANL97A in the simulation is superdense and cold before ∼23:30 UT, then becomes tenuous and hot for ∼75 minutes, then slowly becomes cold and dense again. It is because near the end of this event, some of the hot and tenuous plasma intrudes into the superdense plasma sheet as indicated by the blue intrusion into the yellow coded dense plasma sheet in frame (e) of Figure 4-16. The virtual LANL97A satellite in the simulation encounters first the superdense plasma, then the intrusion of the hot and tenuous plasma sheet and then the superdense plasma again but with less dense plasma.

At around 23:45 UT, most of the superdense plasma of CDPSe reaches geosynchronous orbit and convects to the inner magnetosphere, some also convects to the dayside, as shown in frame (f) of Figure 4-16 and frame (f) of Figure 4-15. The cold dense plasma including the CDPSa and CDPSb has been depleted. The reconnection rate begins to decrease as the tailward high speed plasma bulk flow is reduced as suggested by frame (f) of Figure 4-17. Frame (f) of Figure 4-20 and frame (f) of Figure 4-19 indicate that the stretched magnetic field also begins to be dipolized.

The two pieces of CDPS extending from the flanks (CDPSa and CDPSb) contribute little to this SDPS formation process. Most of their plasma flows tailward during this process (Figure 4-16 and Figure 4-17). It is the cold dense plasma material from above and below the equatorial plane near midnight in the plasma sheet that is compressed and convected earthward to form the SDPS.

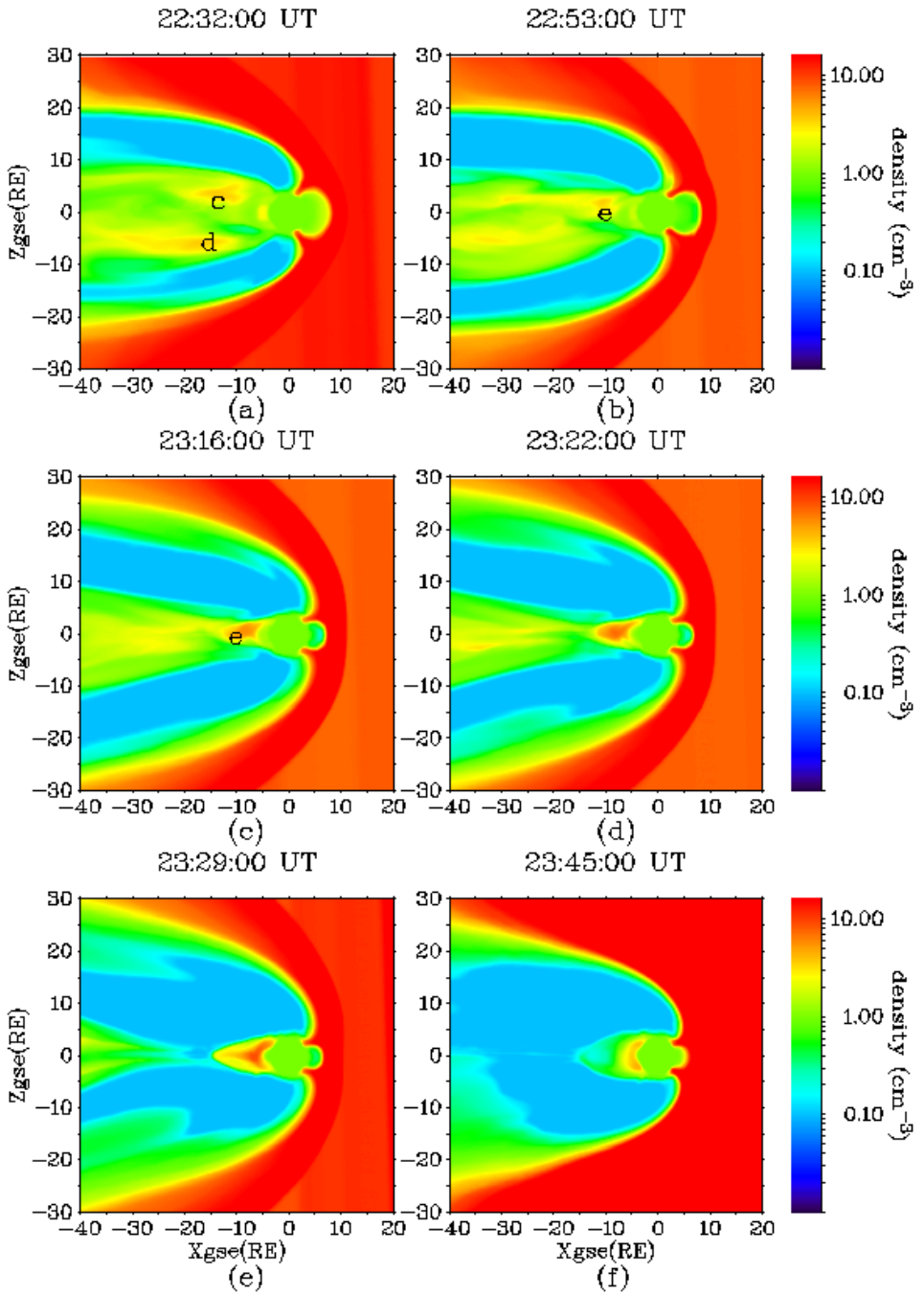

Figure 4-15: The plasma density in noon-midnight meridian plane at different moments during the SDPS event. The magnetosheath in the frames is not visible because all the points with density greater than 16.0 cm^{-3} are shown in one color corresponding to 16.0 cm^{-3}. The frames show the magnetopause (the inner boundary of the red region), magnetotail lobe (north and south blue regions), and the plasma sheet (the central green and orange region). The letters c and d in frame (a), and e in frame (b) and (c) indicate the locations of CDPSc, CDPSd and CDPSe as defined in the text, respectively.

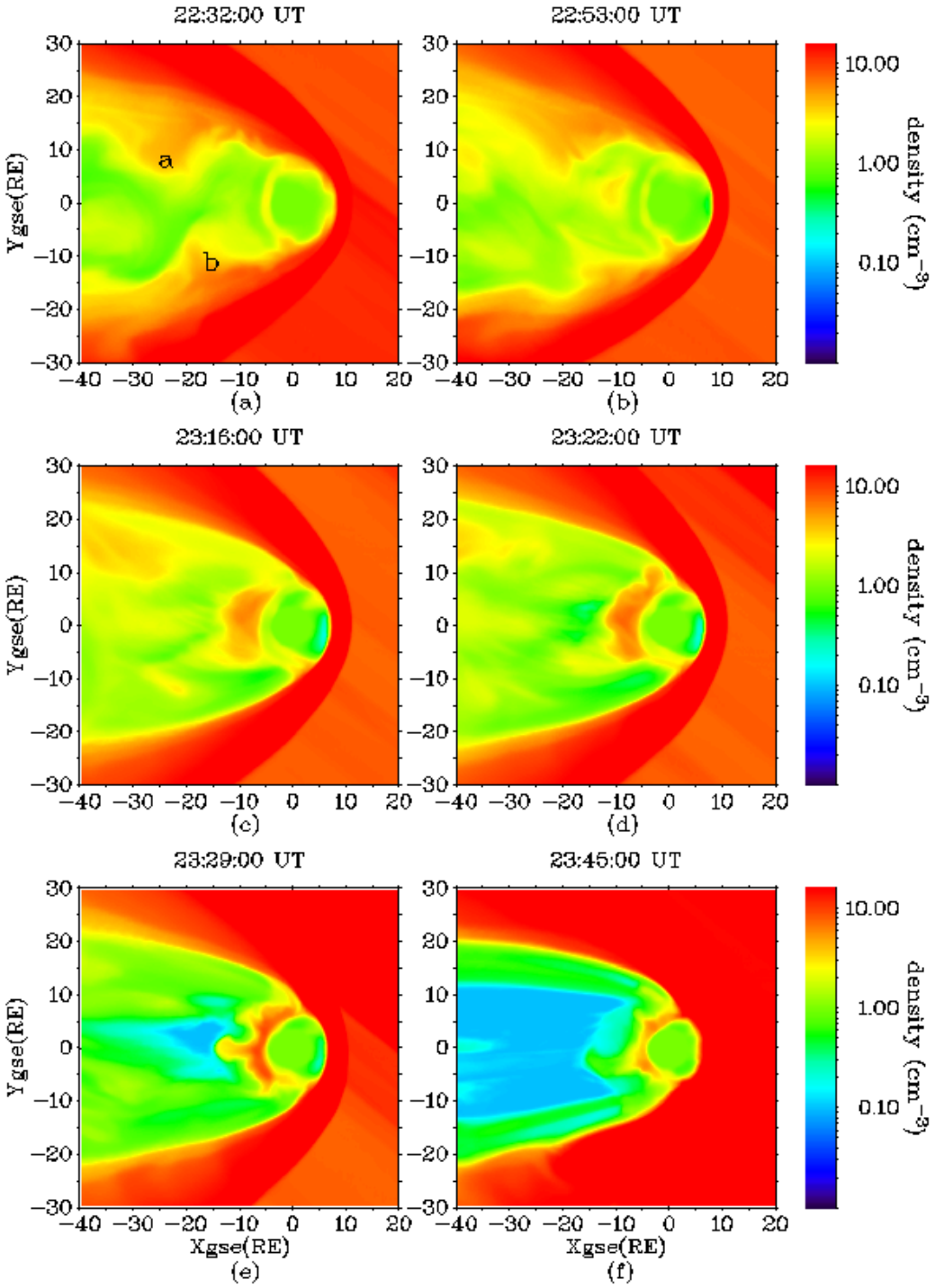

Figure 4-16: The plasma density in the equatorial plane at different moments during the SDPS event. The frames in this Figure correspond to the frames in Figure 4-15. The letters a, and b in frame (a) indicate the locations of CDPSa and CDPSb defined in the text, respectively.

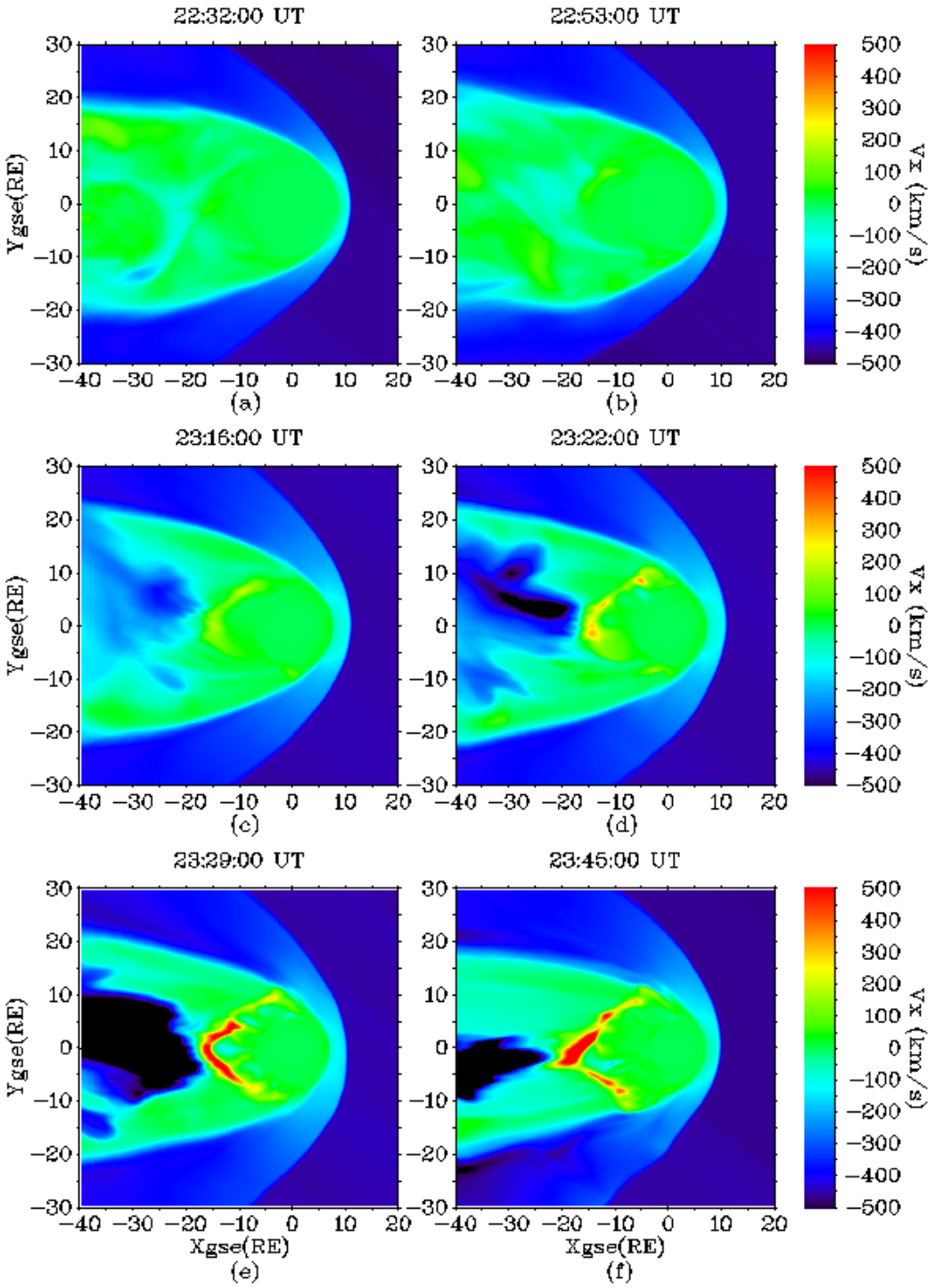

Figure 4-17: The x-component of the plasma bulk speed in the equatorial plane at different moments during the SDPS event. The frames in this Figure correspond to the frames in Figure 4-15.

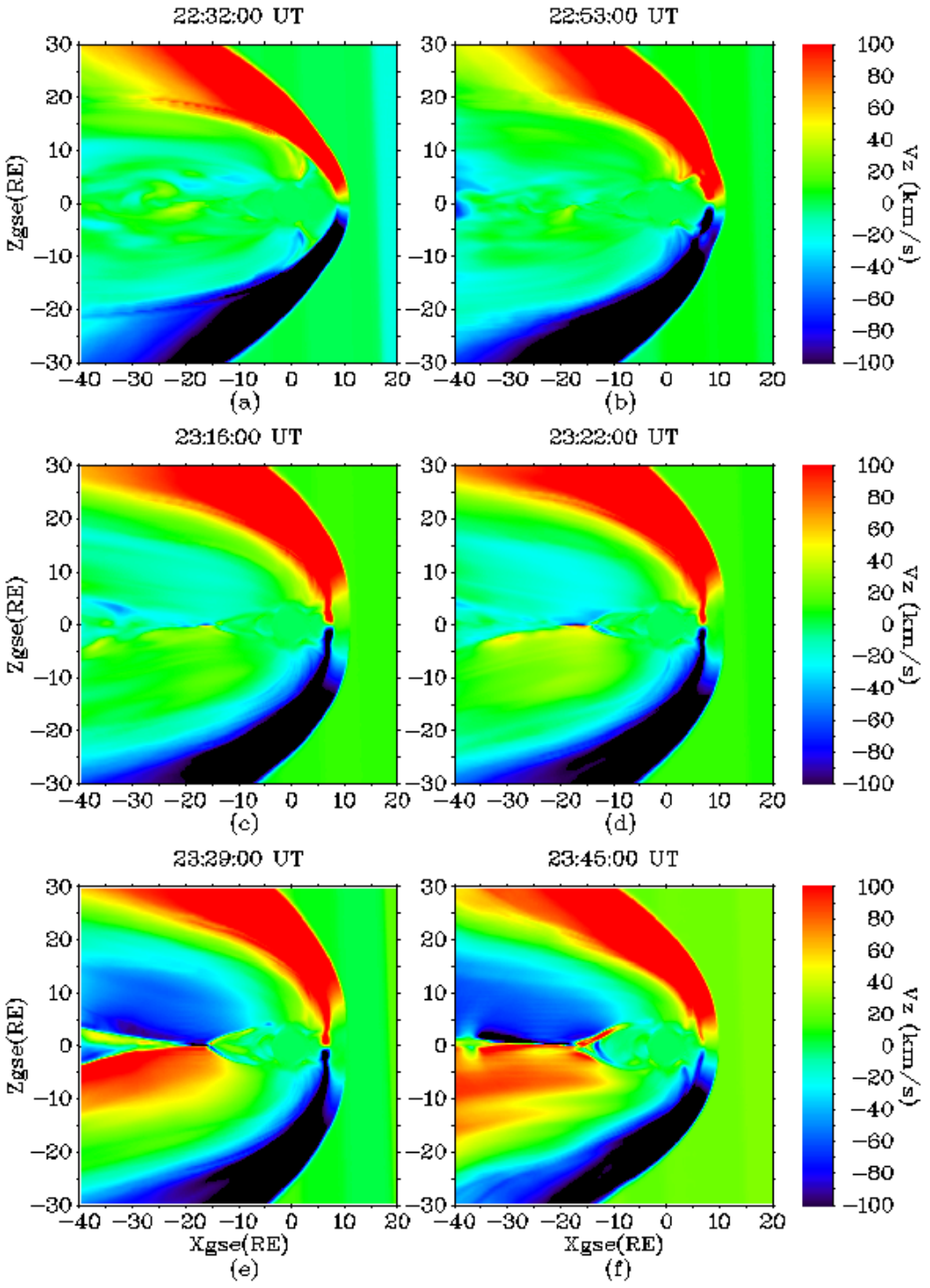

Figure 4-18: The z-component of the plasma velocity in the noon-midnight meridian plane at different moments during the SDPS event. The frames in this Figure correspond to the frames in Figure 4-15. The northern red region and the southern dark region show the northern and southern magnetosheath respectively.

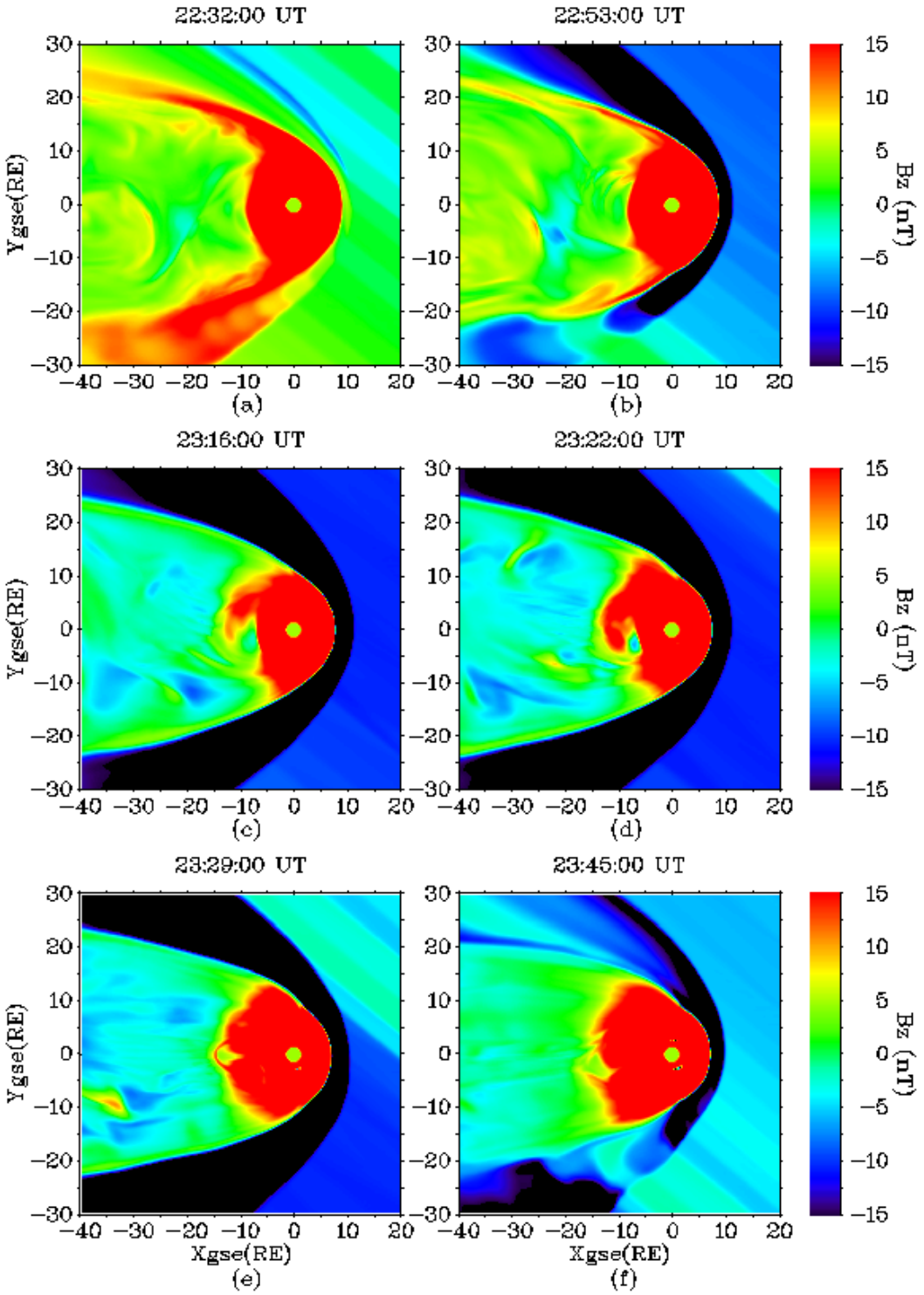

Figure 4-19: The z-component of the magnetic field in the equatorial plane at different moments during the SDPS event. The frames in this Figure correspond to the frames in Figure 4-15. The points with magnitude greater than 15 nT are shown in color corresponding to -15 nT or 15 nT.

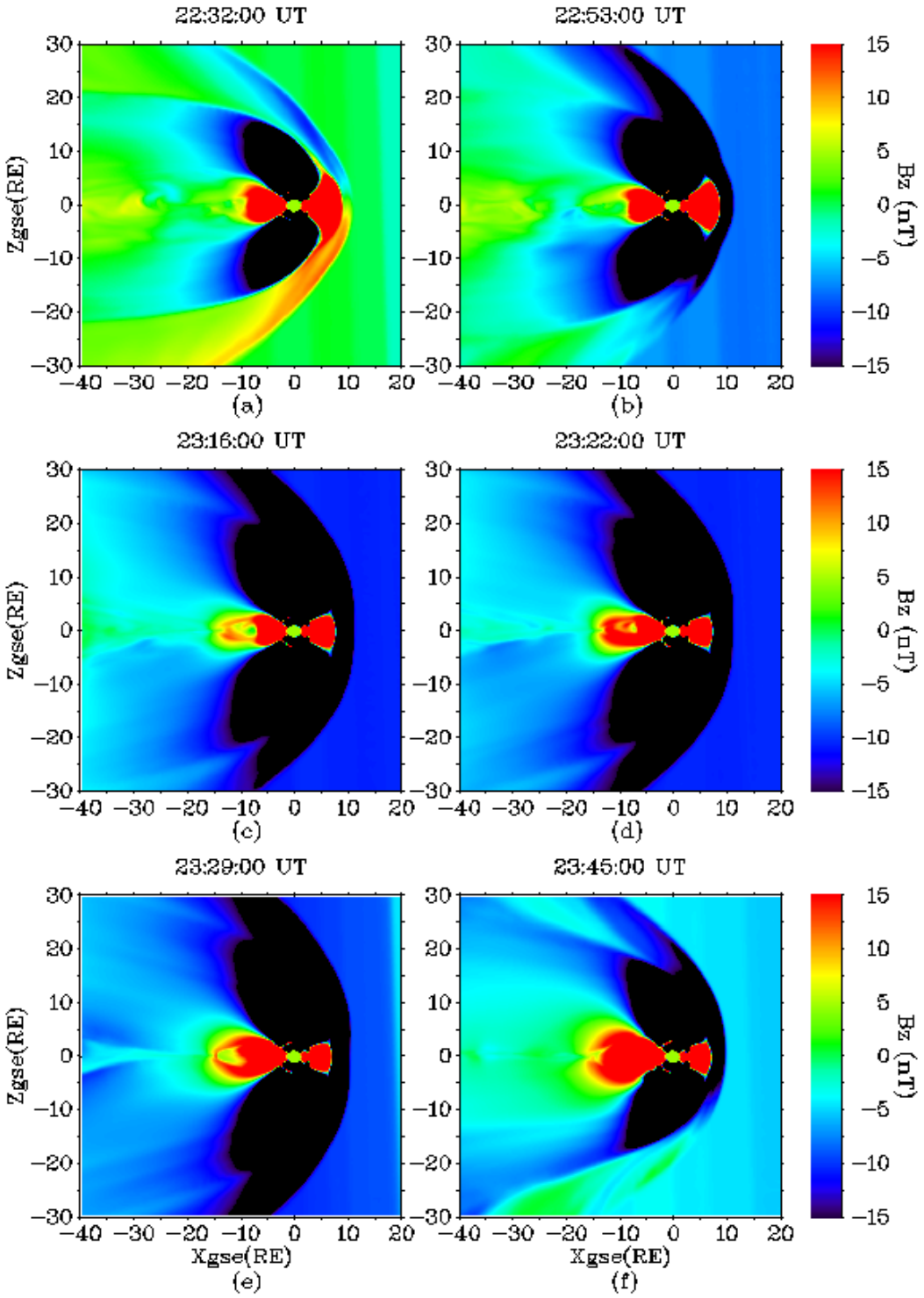

Figure 4-20: The z-component of the magnetic field in the noon-midnight meridian plane at different moments during the SDPS event. The frames in this Figure correspond to the frames in Figure 4-15. The points with magnitude greater than 15 nT are shown in color corresponding to -15 nT or 15 nT.

4.4 Summary and Discussion

In this chapter, I studied the formation mechanism of superdense plasma sheet detected near the geosynchronous orbit under the condition that the IMF turns southward after a long period of northward IMF condition. The SDPS event occurred on September 14/15, 2001. I first investigate the formation process by showing the observations of the event from the solar wind monitors ACE, the Cluster in midnight at $\sim$12 R_E in the tail, the three geosynchronous spacecrafts in the nightside, and the ground magnetic field disturbance during this event. These observations show a chain of events prior to the arrival of the southward IMF following the long period of northward IMF.

This event was simulated with OpenGGCM and was compared to observations of Cluster and LANL satellites. The simulation reproduces the SDPS event quite well. It not only reproduces the CDPS and its disappearance observed by Cluster, but also reproduces the arrival of SDPS at the three LANL satellite locations.

Based on this simulation, I then analyze the simulation to further examine the detailed formation process of the superdense plasma sheet by investigating the time series of plasma density, V_x, V_z, and B_z in equatorial plane and in the noon-midnight meridian.

A long period of northward IMF causes the formation of two pieces of cold dense plasma sheet above and below of the equatorial plane at the midnight local time location in the mid-tail. Subsequent southward IMF first compresses the plasma sheet and causes the compressed CDPS move toward the equatorial plane and then to convect toward the Earth. The continuing compression of the southward IMF then causes the onset of reconnection in the mid-tail plasma sheet at a location beyond -12 R_E (x_{gse}) in the tail. The compressed CDPS forms the superdense plasma sheet and is then accelerated toward the Earth, passes through and flows around

the geosynchronous orbit, and finally disappears in the inner magnetosphere. This formation mechanism is consistent with what *Thomsen et al.* [2003] proposed in their study of the superdense plasma events. The contribution in this simulation study is that the CDPS that forms the SDPS is identified, and the detailed formation process is shown here.

The simulation results show that there are two pieces of CDPS extending from the flanks in the mid-tail, which is in agreement with the Geotail observations discussed in Chapter 3. However, these two pieces of cold dense plasma sheet contribute little to the formation of superdense plasma sheet since most of the dense plasma near the flanks flows tailward after the southward IMF arrival. This can be explained by the compression of the tail lobes by the southward IMF mainly occurring on the high-latitude magnetopause near the noon-midnight meridian. Most of the dense plasma near the flanks is not compressed, or is compressed only slightly. Thus there is little dense plasma near the flanks that convects sunward. It is the CDPS on high-latitude of plasma sheet near the midnight location that can be compressed by southward IMF and form the superdense plasma sheet.

Comparing the simulation and the observations in section 4.3.2, there are some discrepancies between them in addition to the timing differences of the event. Near the end of the superdense plasma sheet event, the density tends to decrease faster in the simulation than in the observation. That means the superdense plasma sheet convects faster in the simulation. The differences may be caused by the difference in environment and physical processes near the inner magnetosphere between simulation and reality. In particular, since the OpenGGCM uses one-fluid MHD theory, there is only ion plasma sheet in the inner magnetosphere in the simulation. In reality, there is also an electron plasma sheet. In addition, the gradient and curvature particle drifts become significant in the inner magnetosphere because of the high energy of

the plasma population, and are not addressed by the MHD simulation. The simulation also neglects the ionospheric outflows which may become significant after the southward IMF arrival in the inner magnetosphere. During the SDPS event, there is compression and dipolization of lobe field and reconnection at the mid-tail. Thus, various waves may be generated, and wave-particle interaction, which is not included in MHD model, increases.

CHAPTER 5

SOLAR WIND PLASMA ENTRY MECHANISM

5.1 Introduction

In chapter 3, I have shown the solar wind plasma entry paths due to double high-latitude reconnection in the case of an event study. A section of an IMF flux tube at the magnetopause is cut by double high-latitude reconnection, and subsequently becomes part of a newly-created closed flux tube, which then convects tailward along the magnetopause and also convects toward midnight after entering the evening local time region. Therefore, the solar wind plasma on this captured flux tube section flows directly into the magnetosphere and becomes part of the plasma sheet. In this chapter, I study the entry mechanism in more detail. I will show the entry behavior under various solar wind, IMF and geomagnetic dipole tilt conditions by running simulations with designed conditions for these parameters. I then analyze in detail the process of high-latitude reconnection, and the related change of magnetic field line topology. I will show that there is a window upstream of the solar wind that allows solar wind plasma to enter the magnetosphere as a result of double high-latitude reconnection. I will then explore the convection behavior of the entering solar wind plasma when it flows from dayside magnetosheath to the nightside magnetotail.

5.2 Simulations for Parameter Study

The OpenGGCM has been successfully used to simulate the CDPS event with an extended period of northward IMF on October 23, 2003, during which a cold dense plasma sheet was observed by Cluster. Based on this simulation case study, I run a series of simulations using generic input parameters where I vary the solar wind and IMF conditions, and the geomagnetic dipole tilt angle. In these simulations, the ionosphere model CTIM (*Fuller-Rowell et al.*, 1996) is coupled to provide inner boundary conditions. The solar wind and IMF conditions are set with the following values: speed of 450 km/s, density of 6.6 cm^{-3}, pressure of 30 pPa, and IMF magnitude of 7.0 nT. The IMF direction is set to be pure southward for the magnetosphere for the first two hours of these simulations. The conditions are then changed according to the parameter to be investigated, and kept constant until the end of simulation. In these simulations, I only vary the geomagnetic dipole tilt angle on the GSE XZ plane, and set the angle constant during any simulation run. The x component of the IMF, and y and z components of the solar wind velocity are set to be zero for simplicity in all of these simulations.

5.3 Magnetic Field Line Topology and Reconnection Processes

In this analysis, I trace fluid elements and the magnetic field flux tubes threading through them. I compute the path (not necessarily a streamline) of an fluid element starting from the solar wind in front of the bow shock at certain time, using the flow velocity field in the simulation domain at different output times, i.e.,

$$\frac{d\vec{X}(t)}{dt} = \vec{V}(\vec{X}(t), t). \tag{5.1}$$

I use linear interpolation in both space and time to compute the velocity as well as other quantities in the simulation at a given location and a given time. I set the tracing time step, i.e., iteration step, to be 2 seconds, corresponding to $\sim 0.14 R_E$ for a flow speed of 450 km/s, or $\sim 0.03 R_E$ for a flow speed of 100 km/s. At each time step, I also compute the magnetic field line threading through the fluid element, and determine its topology (IMF, open or closed).

Here I call the magnetic field flux tube threading through a fluid element as its frozen-in magnetic field line (FIMFL), although such flux tube may not be frozen into the fluid when the fluid element is in a reconnection diffusive region, which is caused by numerical resistivity and the term for anomalous resistivity η in equation 2.102. A fluid element is considered a solar wind plasma element if its FIMFL's topology is IMF. It is identified as an element in the magnetosphere closed field region if its FIMFL's topology is closed. It is considered a lobe or mantle plasma element if its FIMFL's topology is open. Tracing a fluid element and identifying its FIMFL's topology at each tracing step, I find out how a fluid element flows from one region to the other and how it crosses seperatrices.

The simulation shows three topological types of magnetic field lines near the magnetopause: IMF field lines in magnetosheath with both ends in the solar wind, open geomagnetic field lines with one end in the ionosphere and the other end in the solar wind, and closed geomagnetic field lines with both ends in the ionosphere. I classify the field lines further according to their topology and their formation characteristics. These classifications are listed in Table 5.1, and examples are shown in Figure 5-1.

With this classification, I identify the possible reconnection processes near the magnetopause under northward IMF conditions as the 6 processes (a–f) listed in Table 5.2. Each process can occur on either the northern magnetosphere boundary or the southern boundary.

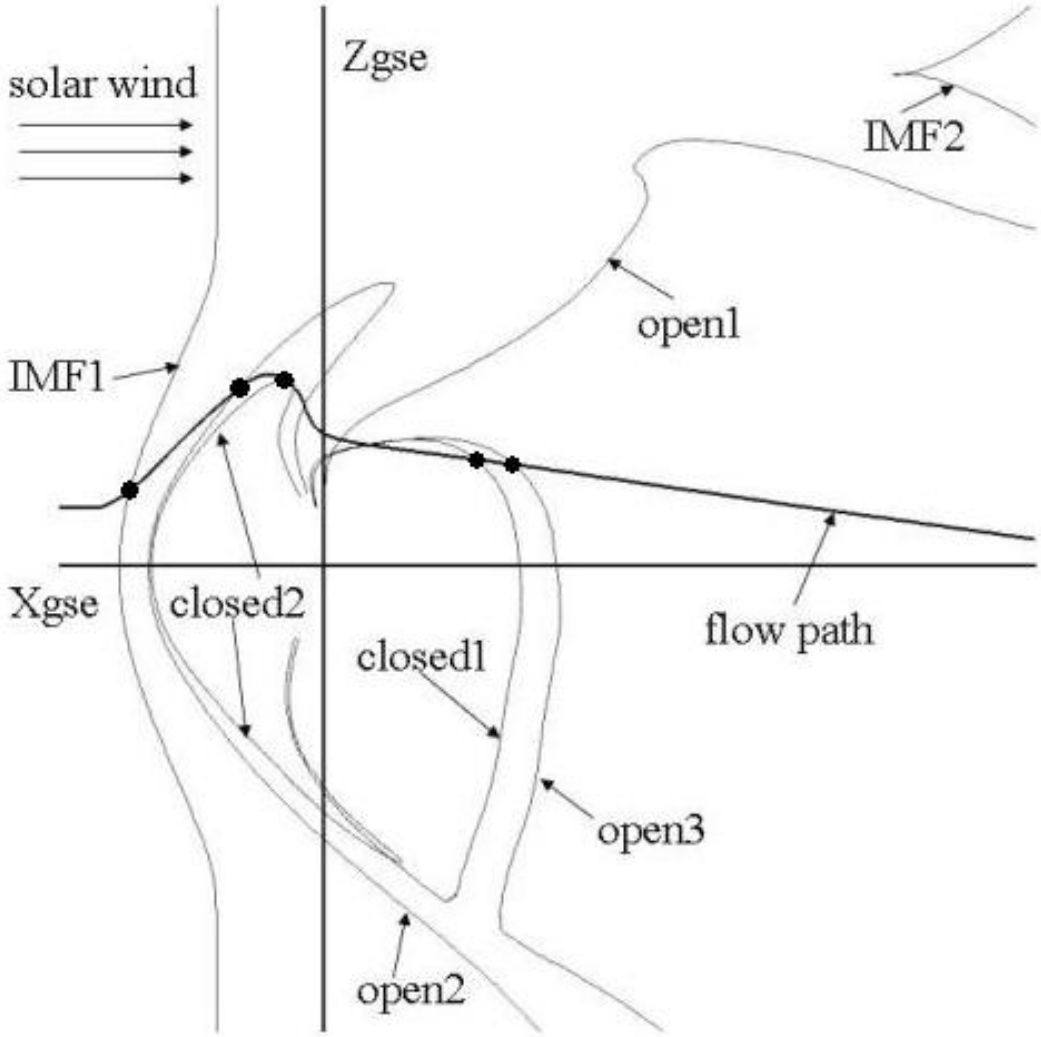

Figure 5-1: The possible topology of the magnetic field line threading a fluid element in the solar wind or the magnetosphere. This is also a sequence of FIMFL topology changes for a solar wind fluid element entering the magnetosphere and convecting tailward. The field lines and the flow path are projected onto the GSE noon-midnight meridian plane. The thinner lines are the frozen-in magnetic field lines and the wider line is the path of the fluid element. The solid circles indicate the intersections between the path and the field lines. For the open1 and IMF2 lines, the intersections are in the far tail and are beyond this figure's boundary.

Table 5.1: Field line topology classification

Name	Description
IMF1	Northward IMF field lines in the magnetosheath before any reconnection has occurred. They may drape over the magnetopause down to the near tail and they may be antiparallel to the northern and the southern lobe or to mantle field lines at some point.
open1	Lobe or mantle field lines extending tailward. They are the original lobe or mantle field lines, or new open field lines (see description of open2 and open3) that have been convected and stretched tailward.
closed1	Closed geomagnetic field lines in the nightside. Some of them may be the new closed field lines (see description of closed2) that have been convected to the nightside.
IMF2	Formed in the tail by reconnection where one section is from a open1 field line, the other section is from an IMF1 field line or an open2 field line. It is detached from the magnetosphere and flows tailward away from the magnetosphere to become the IMF again.
open2	New open field line formed by reconnecting one section from an IMF1 field line and another section from a geomagnetic field line. It drapes around the magnetopause and extends either from the southern cusp to north or from the northern cusp to south in the solar wind.
open3	New open field line formed when an IMF1 field line or a open2 field line reconnects with a closed1 field line, and this new open field line is in the nightside as a whole. It also extends either from southern cusp to north or from northern cusp to south.
closed2	New closed field line formed when an open2 field line reconnects with an open1 field line with footprint in the opposite hemisphere, or with a closed1 field line. It is formed in the dayside and is most likely convected around the magnetopause to the nightside.

Table 5.2: High-latitude reconnection (a–f) and convection (g–i) processes

(a)	IMF1	+	open1	→	open2	+	IMF2
(b)	IMF1	+	closed1	→	open2	+	open3
(c)	IMF1	+	open3	→	open2	+	IMF2
(d)	open2	+	open1	→	closed2	+	IMF2
(e)	open2	+	closed1	→	closed2	+	open3
(f)	open2	+	open3	→	closed2	+	IMF2
(g)	open2	→	open1				
(h)	open3	→	open1				
(i)	closed2	→	closed1				

When a solar wind plasma element flows around the magnetosphere, its FIMFL's topology may undergo a series of changes along the flow path at times when the FIMFL reconnects with another field line. Each topological change means that the fluid element enters into another topological region. One example is shown in Figure 5-1, which displays the path of a solar wind fluid element that enters and leaves the magnetosphere, and the FIMFL of the fluid element. The fluid element's FIMFL first changes from IMF1 to open2 as a result of a reconnection process of type (a), (b), or (c) at the northern magnetosphere boundary. The fluid element flows from solar wind region to the open region, which is the tail lobe or mantle. The FIMFL then changes from open2 to closed2 as a result of a (d), (e), or (f) reconnection process at the southern magnetosphere boundary. At the closed2 stage, this fluid element has entered the dayside magnetosphere. The closed2 field line continues to convect tailward to the nightside and becomes closed1 field line. It changes to open3 because of a reconnection process of (b) or (e) at the southern magnetosphere boundary. The fluid element then becomes an element of the open region again. The open3 FIMFL, being pulled by the solar wind and stretched tailward, then becomes open1 after some time. Finally, the open1 FIMFL participates in another (a) or (d) reconnection process and becomes an IMF2 field line. This fluid element and its IMF2 FIMFL are

now detached from the magnetosphere and become part of the solar wind again. I can combine this sequence of field line changes as a sequence {*IMF1, open2, closed2, closed1, open3, open1, IMF2*} similar to the notation of mathematical permutations.

Different flow paths may have different sequences of FIMFL topology changes. Identifying a sequence of FIMFL topology changes of a fluid element from the solar wind helps me studying the transport of solar wind plasma into the magnetosphere. The reconnection processes listed in Table 2 allow me to identify all possible sequences. A fluid element on any one of the two flux tubes before reconnection (on the left side of the reconnection "relation" in Table 5.2) will become a fluid element of one of the two flux tubes after reconnection (on the right side of the relation). One of the flux tubes in a relation's right side can then possibly become a flux tube in another relation's left side. In addition, the open2 and open3 field lines can become open1 field lines, and closed2 field lines can become closed1 field lines as a result of convection. Listing all the possible combinations of the reconnection relations, I can then find out all the possible sequences. To complete this scheme, I add three more "convection relations" in Table 5.2 to describe the changes of the magnetic field line in shape and position due to convection.

To describe a sequence of a FIMFL's change, I use magnetic field line types defined in Table 5.1 to construct a sequence set. Obviously, the first element of a sequence set is IMF1 since the fluid element comes from solar wind. IMF2 may be the final element of a sequence set since it never appears in the left side of a relation, and a IMF2 field line has been detached from the magnetosphere. Closed1, closed2, and open1 can also be a final element of a sequence because they may not change anymore, at least until the end of a fluid element tracing period. In this analysis, I set the tracing period to be 90 minutes. Based on the simulation results, this time period is the typical time scale for a fluid element to enter the near magnetic tail region.

Using the method described above, a huge number of sequences is possible. However, in reality, most of them will never occur. This is because the reconnection relations in Table 5.2 do not discriminate which section of one flux tube will reconnect with which section of the other flux tube, and do not discriminate the reconnection location. Thus, many combinations of the FIMFL types in a sequence set are not physically possible or unlikely occur. Table 5.3 lists the sequences that I have observed in the simulations.

Of these sequences, I am mainly interested in cases (5), (6), (7), and (8) because only in these sequences the FIMFL is ever closed for some time along the flow path of a fluid element. These sequences represent the possible paths of a fluid element on the central part of an IMF flux tube near equatorial plane, which is eventually cut from the IMF flux tube by double high-latitude reconnection. Such fluid elements from the solar wind are considered being "captured" by double high-latitude reconnection. Other sequences represent the paths of the fluid elements that will not enter the magnetosphere. Such fluid elements are from the northern end or the southern end section of an IMF flux tube that is cut from the IMF flux tube by high-latitude reconnection.

In cases (5) and (6), the newly created closed field lines become part of the geomagnetic closed field, at least until the end of the tracing period. For cases (7) and (8), the fluid element is first captured by double high-latitude reconnection, and is then "released" by another double high-latitude reconnection event occurring at the same location as the previous one. Thus, a captured solar wind fluid element will either become part of the plasma of the magnetosphere, or will be released toward the far magnetotail and detached from the magnetosphere.

Table 5.3: Common sequences of FIMFL topological changes along a flow path

ID	Sequence
(1)	{*IMF1*}
(2)	{*IMF1, IMF2*}
(3)	{*IMF1, open2, IMF2*}
(4)	{*IMF1, open2, open1, IMF2*}
(5)	{*IMF1, open2, closed2*}
(6)	{*IMF1, open2, closed2, closed1*}
(7)	{*IMF1, open2, closed2, closed1, open3, open1, IMF2*}
(8)	{*IMF1, open2, closed2, closed1, open3, IMF2*}
(9)	{*IMF1, open2, open3, open1, IMF2*}
(10)	{*IMF1, open2, open3, IMF2*}
(11)	{*IMF1, open3, IMF2*}
(12)	{*IMF1, open3, open1, IMF2*}

5.4 Solar Wind Plasma Entry into the Magnetosphere

I study the solar wind flow and its FIMFLs by tracing uniformly distributed 400×400 fluid elements starting from a plane upstream of the bowshock with Y_{gse} and Z_{gse} ranging from -20 R_E to 20 R_E. When tracing a fluid element, I compute its FIMFL for each tracing step and determine its topology (IMF, open, or closed). The field line topology is determined by finding out where the end points of the computed field line locate. A field line with both end points within 6 R_E is considered to be a closed geomagnetic field line. It is considered to be a open field line if only one end point is within 6 R_E. Otherwise, the field line is considered to be an interplanetary magnetic field line.

5.4.1 Entry window

I consider a fluid element as being captured if its FIMFL ever becomes closed for some time along the flow path, as described by the sequences (5), (6), (7) and (8) in Table 3. As shown in frames 1–4 in Figure 5-2, I plot the GSE YZ plane projection of each

fluid element at 4 stages: (1)when the fluid element is launched from a location before the bowshock; (2)when the fluid element's FIMFL changes from IMF to open, usually at the dayside magnetopause; (3)when the FIMFL changes from open to closed, also usually at the dayside magnetopause; and (4) when it changes from closed to open again, usually in the tail; or when the tracing is ended. In these four plots, color is used to indicate which flow element is captured and how much time its FIMFL stays in closed topology. Thus, any color other than white indicates that the fluid element will be located on a closed field line for at least a short period of time. For the color points on the plots of the 4 stages as shown in frames 1–4 in Figure 5-2, each color point on one plot has a one-to-one correspondence to the other three points on the other three plots, respectively, with the flow path passing through them. Under constant boundary conditions within a certain time period, the plasma flow in and out of the magnetosphere will be relatively stable. One can think of the color areas on the plots of the first three stages as solar wind "entry windows" at three different stages. Through these windows, the solar wind plasma enters the magnetosphere. I also use color to indicate each fluid element's X_{gse} coordinate for the corresponding stages as shown in frames 5–7 in Figure 5-2. The plots in frames 5–6 of Figure 5-2 represent a three-dimensional view of the entry windows at the magnetopause.

Obviously, the entry window has a different shape at different stages. This analysis also shows that, for each stage, and for different times at which a fluid element is launched may result in different shape of entry window. The entry widows with launching times near the turning of southward IMF to northward IMF is different from the ones with launching times several hours after the northward turning of the IMF. Even after hours of constant uniform solar wind and IMF input conditions, the shape of entry window is not perfectly symmetric and still changes in time. This is because the reconnection rate is not constant as a result of the anomalous resistivity,

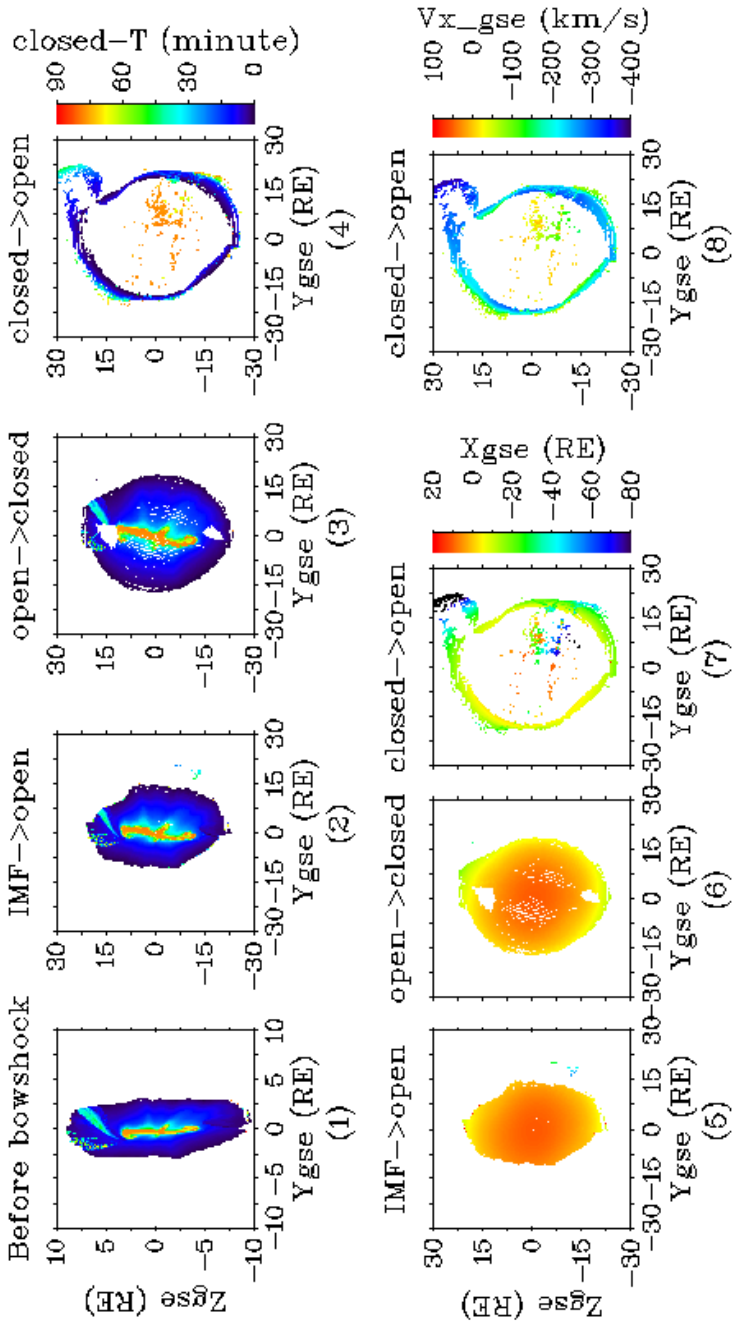

Figure 5-2: Solar wind entry window at different stages. The IMF is pure northward and the geomagnetic dipole tilt is zero. Frames 1–4 show the color-coded closed-time, which is the life time of a newly created closed field line during a flow path tracing. Frames 5–7 show the color-coded X_{gse} coordinate corresponding to Frames 2–4 respectively. Frame 8 shows the color-coded average V_x corresponding to Frames 4 and 7. See text for a detailed description

current density variations, and the dynamic nature of the plasma flow. The ionosphere variations also cause the entry window to change in time and break its symmetry (see section 6.4).

The plasma fluid elements on the same captured flux tube should in principle flow to the same area and have the same amount of closed-time, if the assumption of frozen-in flux holds. However, on the entry window, near the end of the north or south boundary, the fluid element has a shorter closed-time than the one in the center, and flows to a different area. Examining the FIMFLs of fluid elements on the same starting IMF flux tube, I found that the plasma element near the reconnection site jumps from the original flux tube to another flux tube. This results from the fact that the frozen-in condition is broken at the reconnection site and the plasma is decelerated or accelerated near the reconnection site. Indeed, I find that the electric field and current density are high in this area (not shown here).

The time between stage (2) and stage (3), i.e., the time between a field line reconnecting in one hemisphere and then reconnecting in the other hemisphere, is short, from seconds to a few minutes. The entry window of stage (3) shown in frame 6 of Figure 5-2 can be considered as the separatrix surface, inside which there is a layer of newly created closed field lines. Outside this separatrix surface, there is a layer of open field lines.

5.4.2 Solar wind entry flow pattern

Frames 1–4 and 7–8 in Figure 5-2 indicate that the captured plasma fluid elements may be classified into three groups. The first group of fluid elements is located on the central flux tubes that face the nose of the magnetopause, and are the brightest points on the entry window. The FIMFLs of these fluid elements stay for a long period of time in closed topology, usually more than 60 minutes. This group is also divided into

two subgroups. One subgroup of fluid elements flow to near the dawn or dusk side of the plasma sheet, and some flow deep inside the plasma sheet. Their flow speed is low, and is usually less than 100 km/s. Examining the density and temperature along the flow paths of some of these fluid elements, I find that the density is ∼1–10 cm^{-3}, and the temperature is about 1 KeV when they are in the plasma sheet. Comparing to the properties of the observed cold dense plasma sheet (e.g., *Fujimoto et al.*, 1996, 1998; *Phan et al.*, 1998; *Fuselier et al.*, 1999; *Øieroset et al.*, 2002), I conclude that this subgroup of solar wind plasma elements forms the cold dense plasma sheet. The other subgroup of fluid elements is represented by the points with long closed-time in frame 4 and positive X_{gse} coordinates in frame 7 of Figure 5-2. This subgroup of fluid elements flows into the dayside closed field region, and their associated new closed field lines become part of the closed field lines in the dayside. The flow path in Figure 5-3 is such an example. Its sequence of FIMFL's change (not shown here) along the path is also an example of the sequence (5) in Table 5.3 ({*IMF1, open2, closed2*}). This fluid element flows from a place near the sun-earth axis to the magnetosphere. After its FIMFL becomes closed, i.e., after it becomes a closed2 field line, the fluid element first flows eastward along the magnetopause and then turns southwestward. The flow speed in the magnetosphere is very slow since the whole path takes 90 minutes.

Fluid elements of the second group are located on the flux tubes near the first group's flux tubes, and are represented by the green or blue points on the entry windows shown in frames 1–3 of Figure 5-2. Their closed topology time period is shorter than the first group fluid elements, and ranges from about 30 minutes to about 60 minutes. Most of these fluid elements flow to the boundary of the magnetotail, creating a dawn/dusk asymmetric feature. The dawn side fluid elements of this group flow northward and tailward along the magnetopause, whereas the dusk side fluid

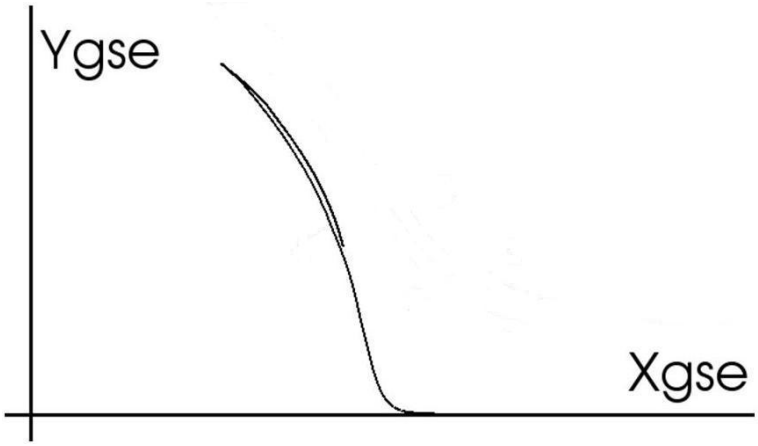

Figure 5-3: An example of flow path of a solar wind fluid element which becomes part of the dayside magnetosphere. This fluid element enters at a location very close to the subsolar region.

elements flow southward and tailward along the magnetopause. The plasma from the first and second groups form a "S" shape in the plasma sheet. The first group fluid elements also have a similar, but less obvious, asymmetric feature as the second group.

The third group of fluid elements is represented by the points with dark blue color on the entry windows in Figure 5-2. Most of them have closed-time less than 10 minutes. They flow all over the magnetosphere boundary into the very near tail where X_{gse} is greater than ∼-10 R_E. The second and third group of flow elements form a "closed boundary layer" in the near magnetotail. The plasma flow of this group has the fastest flow speed among the three groups, while the first group has the slowest speed, as indicated by the average V_X during the closed-time period in frame 8 of Figure 5-2.

The above classifications and descriptions are based on a simulation with pure northward IMF, zero geomagnetic dipole tilt angle, and typical solar wind conditions. However, the classification of 3 groups of entry fluid elements also holds for all other solar wind and IMF conditions as shown in Figures 5-5, 6-1, 6-3, 6-4, and 6-6 in which

the entry windows always have the same three types of color area corresponding to the three groups of flow elements. A survey of entry window plots as shown in Figure 5-2 for various IMF magnitude and solar wind conditions, but with pure northward IMF and zero dipole tilt angle shows that their flow pattern and distribution of the flow elements are all similar. The classification of three groups of captured flow elements is valid for all conditions that I have studied. Figure 5-4 gives examples of closed-time distributions for different IMF clock angles. The distributions show a very high peak for closed-time less than 20 minutes, which corresponds to the third group. There is another peak at around 70 to 80 minutes, which is related to the first group (most obvious for 0° IMF clock angle). There is also a small peak at around 40 minutes. I approximately define the three groups with the closed-time domains [60,90], [30,60) and (0,30) from the first to the third respectively. Note that the total tracing time is 90 minutes in the analysis, and there is a travel time of about 10 minutes for the fluid elements to reach the magnetopause. The formation of the three groups of captured plasma (or new-closed field lines) is mainly due to the entry position of the fluid elements. However, the $J \times B$ force on the new-closed field lines and the electrodynamic properties of the magnetopause may also affect into which group an IMF field line enters.

Figure 5-5 shows plots in the same manner as frame 4 of Figure 5-2 for other IMF clock angles and other dipole tilt angle cases. For positive IMF clock angles, the captured fluid elements have similar convection behavior as discussed above. For negative IMF clock angles, the behavior of the captured flow elements is also similar, although there are some differences in the shape of the third group. For small dipole tilt angles, the entry behavior is similar to that for zero dipole tilt angle. Large dipole tilt breaks the dawn/dusk asymmetric flow behavior of the captured fluid elements. For positive (negative) dipole tilt angle, the captured plasma tends to flow southward

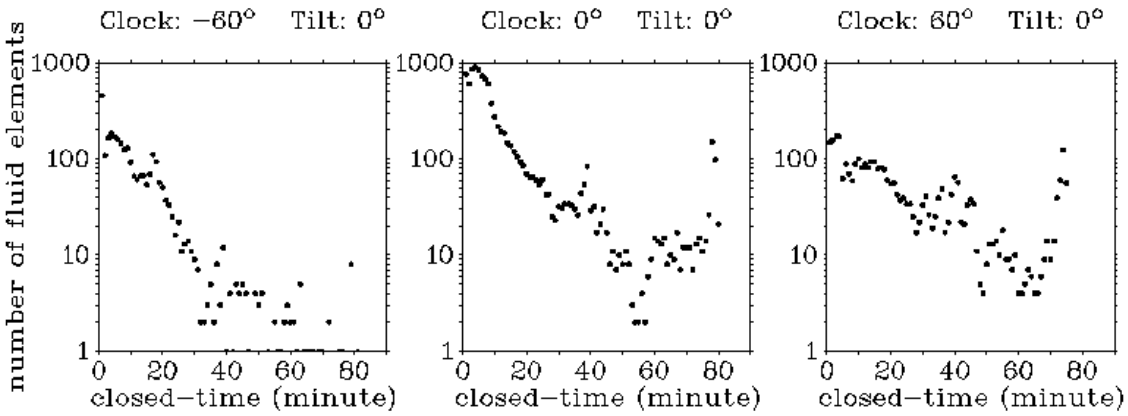

Figure 5-4: Examples of distribution of the time period (closed-time) that a fluid element dwells on closed field line. The left is closed-time distribution for IMF with $-60°$ clock angle. The middle is for pure northward IMF, and the right is for $60°$ IMF clock angle. All have zero geomagnetic dipole tilt. These 3 distributions all have peaks around 5 minutes, 40 minutes and 80 minutes.

(northward) and tailward.

In one case, the simulation of CDPS event 1 in Chapter 3, I find that the flow pattern is opposite. In this case, the dusk (dawn) side captured fluid elements flow northward (southward) and tailward. The dipole tilt in XZ(GSE) plane is $-12.6°$, and the tilt in YZ(GSE) plane is $-9.5°$. During this event, the IMF is almost pure northward and has almost no B_x component. I ran another simulation with zero dipole tilt and the same solar wind and IMF conditions. The particular flow pattern still exists. Therefore, the flow pattern may also most likely be affected by solar wind velocity in addition to IMF clock angle and dipole tilt angle.

The open boundary layer formed by newly created open field lines also affects the flow behavior of the captured fluid elements. In other words, it affects the convection of the newly created closed field lines. All the open field lines created by high-latitude reconnection extend either from the northern cusp to the southern hemisphere in the solar wind, or from the southern cusp to the northern hemisphere in the solar wind, as shown in Figure 5-6. Draping over the magnetopause, such open field lines may

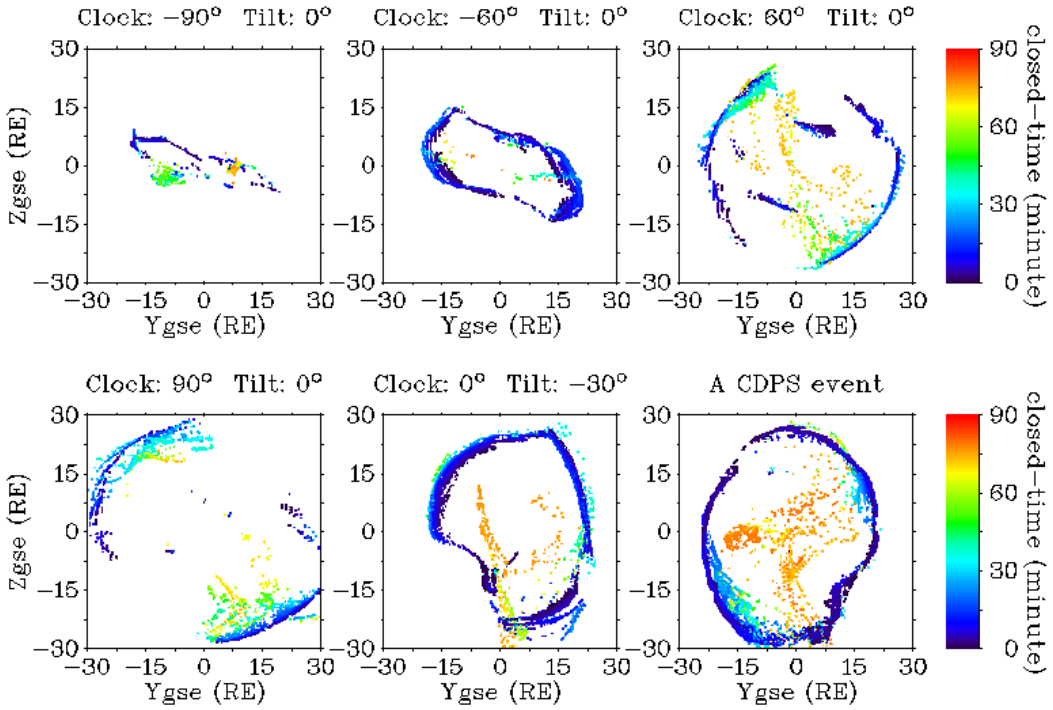

Figure 5-5: YZ(GSE) plane projection of captured fluid elements at the stage when their frozen-in magnetic field lines change from closed field lines to open field lines, or when the tracing of the fluid elements ends. These plots are the same kind of plot as in frame 4 of Figure 5-2 for different IMF clock angles and dipole tilt angles, as well as for the CDPS event on October 23, 2003.

have a curvature force on the magnetopause in the regions where there is curvature in the magnetic field. The direction of this curvature force depends on how the open field lines extend from the cusps. Such curvature force may affect the convection of the new-closed field lines. When the open field lines on dusk and dawn side extend in the opposite direction, as shown in Figure 5-6, the open field lines may exert a torque over the magnetopause. For example, when most of the new-open field lines at the dusk side extend from northern cusp to the south, and most of the new-open field lines at the dawn side extend from southern cusp to the north, there will be a clockwise torque over the magnetopause looking from the Sun.

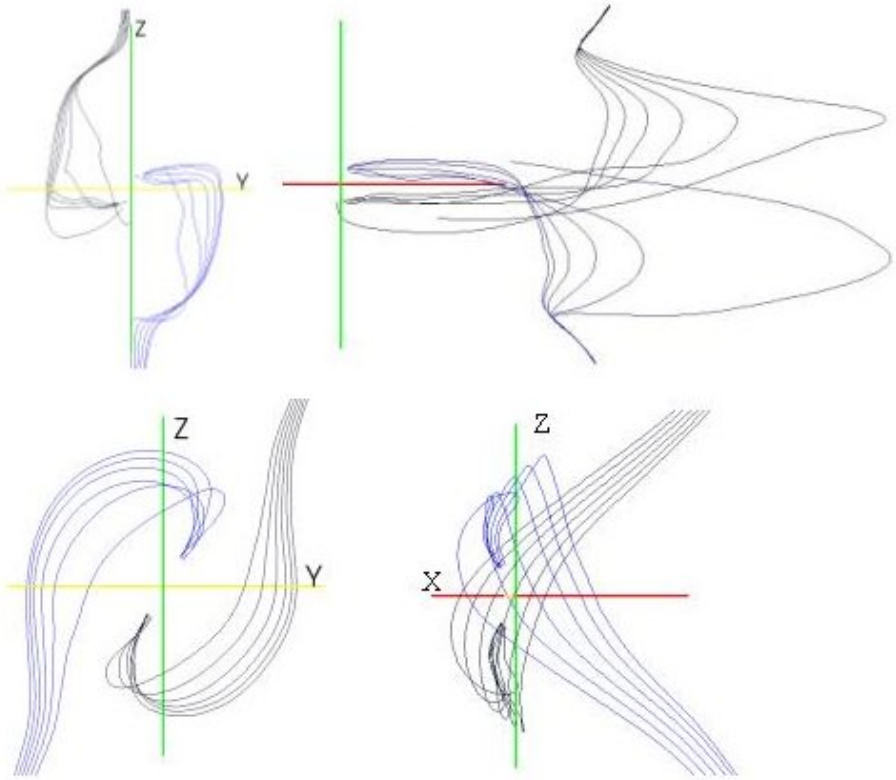

Figure 5-6: Examples of newly-created open field lines as a result of high-latitude reconnection. The top two frames show the open3 field lines and the bottom two frames show the open2 field lines.

I also found that the ionosphere has a significant effect on the convection of the

new-closed field lines. I will discuss this in section 6.4. The convection behavior of the new-closed field lines is related to the entry rate (see section 6.4). Thus convection is affected by IMF clock angle, dipole tilt angle, solar wind conditions, new-open field lines and the ionosphere. However, a more detailed study of the convection of new-closed field lines in the tail, as well as the formation of the three groups of captured fluid elements, is beyond the scope of this dissertation study.

5.4.3 The distribution of cold dense plasma

I have so far discussed the distribution and convection behavior of the captured solar wind plasma. I also classified the captured solar wind flow elements into three distinct groups. Since the captured plasma is magnetosheath plasma, which is cold and dense in spite of a slightly heated component that comes from high-latitude reconnection, the distribution of the captured plasma represents the distribution of cold dense plasma in the magnetosphere. Here I assume that double high-latitude reconnection is the dominate process that brings the magnetosheath plasma into the magnetosphere, because the simulation reproduces the observed cold dense plasma sheet, but has not sufficient resolution to resolve the Kelvin-Helmholtz instability, which is considered another important process that can possibly transport solar wind plasma into the magnetosphere.

Comparing the properties of the fluid elements of the first group with observed properties of the cold dense plasma sheet, I conclude that they form the observed cold dense plasma sheet. They flow along the dayside magnetopause and enter mostly into a region near the flanks in the near tail. As a result, cold dense plasma will be observed on the high-latitude plasma sheet and also near the flanks. It appears that there are two pieces of cold dense plasma area that extend inward from the dawn and dusk flanks respectively. This is in agreement with observation made by Wind and Geotail

spacecrafts (*Phan et al.*, 1998; *Øieroset et al.*, 2002). Each of these cold dense plasma areas has an inner boundary which is defined by the inner most layer of new-closed field lines that have been convected to the nightside.

The fluid elements of the second or third group Figures 5-2 and 5-5 suggest that there is also cold dense plasma at the near tail magnetosphere boundary. Our simulation shows that the cold dense plasma on the boundary (plasma elements of the second or third group) is denser and flows faster than the cold dense plasma in the central plasma sheet (plasma elements of the first group). In other words, the plasma near the tail boundary is more like magnetosheath plasma and may not be associated with the CDPS as defined from spacecraft measurements.

5.4.4 Depletion of cold dense plasma and geomagnetic field convection cycle

Under constant northward IMF conditions, high-latitude reconnection continuously occurs between IMF and high-latitude tailward of cusp geomagnetic field, and consequently causes magnetosheath plasma to enter the magnetosphere continuously. Two questions arise: (1) whether the lobe field vanishes at some point and the whole magnetosphere becomes completely closed, and (2) whether the whole plasma sheet becomes cold and dense, and the density increases up to magnetosheath values? However, neither of these scenarios is what I observe in the simulations or what observations would indicate. The Cluster observations of the steady long period northward IMF event on October 23, 2003 UT shows that the density of CDPS first rises over a 3-hour period and then remains at the 1.5 cm^{-3} level during almost the whole remaining period (*Øieroset et al.*, 2005). Our simulation of this event also shows a nearly constant density of the CDPS after about 3 hours of northward IMF. The second CDPS event discussed in Chapter 3 also shows a CDPS with steady density during the northward IMF period. Thus, there must be a process that depletes the cold

dense plasma so that a balance between plasma inflow and outflow is established.

The reconnection processes (b) and (e) discussed in section 5.3 imply that the magnetosphere will never completely close since new closed field lines, open3 field lines, are created from closed field lines. These processes also provide a cold dense plasma depletion mechanism. After the reconnection processes (b) and (e) occur, some closed1 field lines, the newly created closed field lines that have been convected to the tail, become open again. The sequences (7) (together with Figure 5-1) and (8), discussed in section 5.3, show a process that releases the captured cold dense plasma by subsequent double high-latitude reconnection at the same locations as those where the dayside plasma is being captured simultaneously. A plasma fluid element that has been captured may become one element on a new IMF field line that will flow away from the magnetosphere. Diffusive processes may also let the cold dense plasma diffuse into neighboring regions such as the inner magnetosphere and the lobes. It is also possible that some cold dense plasma depletes into the ionosphere along closed flux tubes. However, the simulation results indicate that the re-reconnection process is sufficient to drain enough cold dense plasma from the plasma sheet to establish an equilibrium of inflowing and outflowing plasma.

Figure 5-5 shows the y and z GSE coordinates of the captured fluid elements in the tail when the associated new-closed field lines change to open. The y and z coordinates and the associated color show that it takes from $\sim$1 to $\sim$80 minutes for a new-closed field line to convect to a place where it becomes open again, depending on which entering group it belongs to. Some new-closed field lines staying closed at the end of the tracing will also open eventually if I extend the tracing time.

Figure 5-1 and the sequences (7) and (8) suggest a cycle of the geomagnetic field line convection for northward IMF conditions. Considering a field line in the tail-ward northern cusp, it goes from open1 (or closed1), first becomes open2 convecting

sunward, then becomes closed2 convecting tailward and becomes closed1, and may finally change back to open1.

5.5 Summary and Discussion

Based on the successful simulation of the CDPS event on October 23, 2003, I have simulated the magnetosphere with the global MHD model OpenGGCM for various solar wind conditions, northward IMF clock angles and geomagnetic dipole tilt angles. In the analysis, I trace the solar wind plasma flow globally, and study fluid elements' flow paths and the magnetic field lines threading through the fluid elements. I construct solar wind entry windows to display how the solar wind plasma enters the magnetosphere, and reveal the entered plasma's convection behavior in the magnetotail. I investigate the distribution of entered magnetosheath plasma in the magnetosphere, including the distribution of cold dense plasma in the plasma sheet. I also show that there is a mechanism for the depletion of cold dense plasma in the plasma sheet during northward IMF condition.

The present simulation shows that high-latitude reconnection occurs between IMF field lines and lobe field lines, between IMF field lines and new-closed field lines that have been convected to the nightside, between new-open field lines and lobe field lines, and between new-open field lines and nightside new-closed field lines. These high-latitude reconnection processes are listed in Table 5.2. Reconnection occurs for any IMF clock angle between $-90°$ and $90°$, and for any geomagnetic dipole tilt between $-30°$ and $30°$. Under constant northward IMF conditions, high-latitude reconnection continuously converts lobe/mantle open field lines into closed field lines, and also converts newly created closed field lines that have been convected to the nightside back into open field lines.

Double high-latitude reconnection captures magnetosheath plasma and brings it

into the magnetosphere. Under constant northward IMF conditions, there is an entry window through which solar wind plasma flows into the magnetosphere as a result of double high-latitude reconnection. The entering solar wind plasma can be classified into 3 classes. The first class enters the dayside inner magnetosphere and the plasma sheet. The second class flows to the tail boundary. The third class flows to the near tail boundary, and stays on closed field just for a relatively short period (< 30 minutes). When convecting tailward, the first and second classes of captured plasma tend to flow northward in one side of the magnetosphere and flow southward at the other side for conditions of small geomagnetic dipole tilt angle.

The path and destination of the entering magnetosheath plasma determines the distribution of cold dense plasma in the magnetosphere. The first class of the entering plasma is the main source of the cold dense plasma sheet, which has two main pieces extending from the near tail flanks. Some of the first part of the entering plasma stays in the dayside inner magnetosphere. The path and destination of the second and third classes of entering plasma indicate that there is also cold dense plasma distributed on the near-magnetotail boundary. Such cold dense plasma is located on closed field lines, and is denser and flows faster than the cold dense plasma in the plasma sheet.

Double high-latitude reconnection can not only capture magnetosheath plasma, but also simultaneously release some of the captured plasma that has convected to the nightside. Cold dense plasma may also diffuse into neighboring regions. Therefore, a balance between inflow and outflow of cold dense plasma is established at some point under constant northward IMF condition. Such capture-release process also implies a geomagnetic field convection cycle from open to close and back to open.

Our simulation results are consistent with several observational studies. First of all, the high-latitude reconnection has been long proposed (*Dungey*, 1963; *Russell*,

1972; *Cowley*, 1981). Observations have provided evidence (e.g., *Gosling et al.*, 1991; *Kessel et al.*, 1996; *Fuselier et al.*, 2000; *Le et al.*, 2001; *Onsager et al.*, 2001; *Phan et al.*, 2003; *Lavraud et al.*, 2002, 2005b), and global MHD numerical simulation modules have reproduced this process (*Raeder et al.*, 1997; *Gombosi et al.*, 1998; *Guzdar et al.*, 2001). *Onsager et al.* [2001] reported a broad local-time range of reconnection locations near the cusp. Our entry windows for IMF clock angles between $-90°$ and $90°$ suggests that the reconnection location is not limited around midnight at high-latitude poleward of cusp. The reconnection location may be near the flanks as well. Reconnection near the northern dawn side flank under northward IMF conditions has been reported by *Eriksson et al.* [2004]. *Onsager et al.* [2001] also identified all the characteristic field lines that resulted from high-latitude reconnection: new open field lines with footprints in either northern or southern hemisphere, new closed field lines, and high-latitude closed field lines participating in high-latitude reconnection. Using the nomenclature presented here, these are open2, closed2, and high-latitude closed1 field lines, respectively.

At the dayside magnetopause, a layer of new open field lines and a layer of new closed field lines are indicated by entry windows at the magnetopause shown in Figure 5-2. Such layers have been identified by *Le et al.* [1996], and *Onsager et al.* [2001].

The second class of entering solar wind fluid elements flows to the tail boundary. The plasma of this group is thus forming a boundary layer in the magnetotail. *Raeder et al.* [1997] proposed a so called tail flank boundary layer (TFBL) under northward IMF condition based on global simulations and Geotail observations. Geotail observed plasma near $X_{gse} = -46$ R_E with a slow tailward speed and on closed field lines.

The simulations in this study reproduce a cold dense plasma sheet that has the observed values of density and temperature. Its location and distribution is also consistent with observations, which show that the CDPS is mainly near the tail

flanks but can also be found deep inside plasma sheet (e.g., *Fujimoto et al.*, 1996, 1998; *Phan et al.*, 1998; *Fuselier et al.*, 1999; *Øieroset et al.*, 2002).

The convection behavior of the newly created open or closed field flux tubes have critical effect on the structure of the outer magnetosphere including the boundary layer inside the magnetopause, the tail lobe and the plasma sheet. I have analyzed the behavior of high-latitude reconnection which consequently affect the convection of the newly created open or closed field flux tubes. However, the detailed convection behavior and how it affects the outer magnetosphere are beyond the scope of this dissertation study and need further investigation.

CHAPTER 6

SOLAR WIND ENTRY RATE

6.1 Introduction

In Chapter 5, I have established the entry window that allows solar wind plasma to enter the magnetosphere as a result of double high-latitude reconnection. In this Chapter, I will further study how the entry window's size, shape and orientation depend on the solar wind, IMF and geomagnetic dipole conditions. I will then compute the solar wind entry rate due to the entry window and establish the relationship between the entry rate and the solar wind, IMF and dipole parameters. I will also show that the ionosphere has an important effect on the entry window as well as the high-latitude reconnection rate and the convection behavior of the entering magnetosheath plasma.

Eastman et al. [1985] estimated that a few times 10^{26} particles per second enter the magnetosphere based on ISEE observations of cold- and hot-plasma components within the central plasma sheet. They also suggested that the contributions to the low temperature component of the plasma sheet enter directly from the boundary layer located along the magnetotail flanks. *Richard et al.* [1994] calculated the total entry rate to be 1.7×10^{27} particles per second using test particle simulation for northward IMF conditions. They also show that the particles mainly enter the magnetosphere as a result of convection into the magnetosphere on reconnecting field lines.

In Chapter 3, I showed that OpenGGCM reproduces the CDPS with great fidelity and also reproduces the plasma sheet state transition both from the hot tenuous

state to the cold dense state when the IMF changes from southward to northward, and from the cold dense state to the hot tenuous state when the IMF changes from northward to southward. In these simulations, I did not find any indication of the KHI process that may also bring magnetosheath plasma into the magnetosphere as suggested by *Fujimoto and Terasawa* [1994] and *Fairfield et al.* [2000]. Thus, I conclude that the double high-latitude reconnection process is the dominant mechanism that causes magnetosheath plasma enter into the magnetosphere and consequently form the CDPS. Based on this assumption, I estimate the main plasma entry rate using the size of the estimated window and solar wind conditions.

6.2 Entry Window Dependence on Solar Wind, IMF and Geomagnetic Dipole Tilt

The solar wind entry rate is related to the size of the entry window. The shape and size of the entry window is controlled by the characteristics of the geomagnetic field, the solar wind and IMF. Figures 6-1, 6-3, 6-4, and 6-6 show how the area of the entry window located before bowshock is related to these conditions. Since the entry window changes in time slightly even under constant solar wind and IMF conditions, I compute the entry windows for different fluid element launching times, and show their average and standard deviation in Figure 6-7. For each data point in Figure 6-7, there are 9 computed entry windows corresponding to fluid element launching times 4:55, 5:00, 5:05, 5:55, 6:00, 6:05, 6:55, 7:00, and 7:05, where 4:55 means 4 hours and 55 minutes after the beginning of a simulation, and after $\sim$1 hour and 55 minutes of northward IMF at the magnetopause. Figure 6-8 summaries the average entry rates in terms of particle flux only through the entry window area with long closed-time ($>$ 30 minutes).

6.2.1 IMF clock angle dependence

Figure 6-1 and frame (a) of Figure 6-7 show how the entry window's size and orientation change with the IMF clock angle. The window size becomes smaller when the absolute value of clock angle is larger, and the window orientation aligns with the IMF direction.

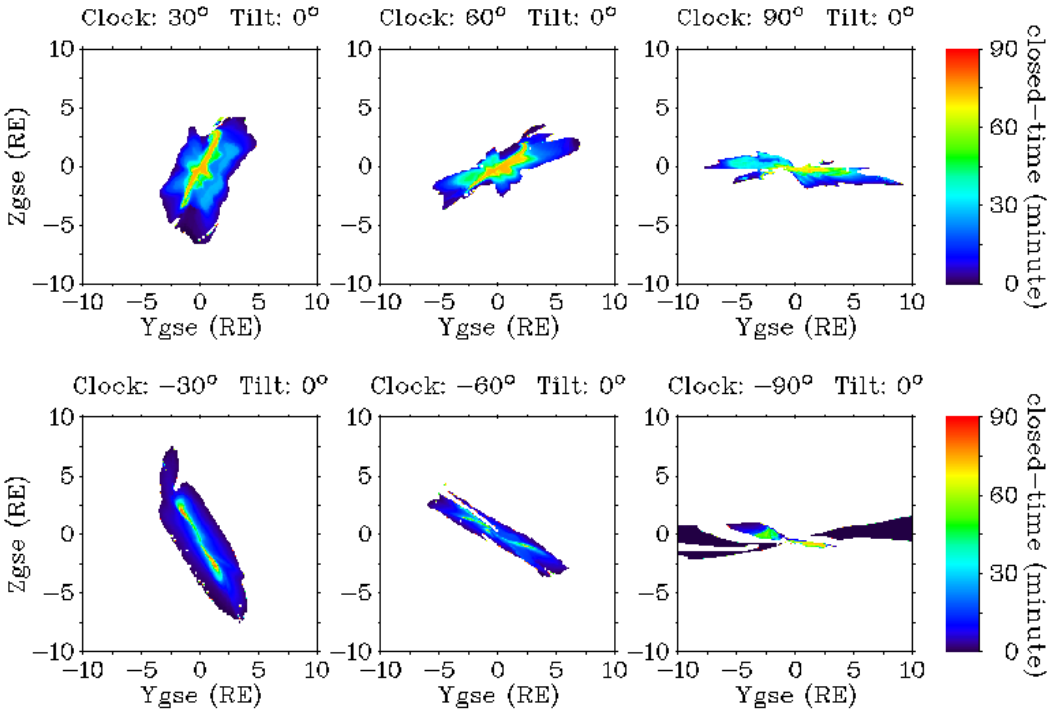

Figure 6-1: Solar wind entry windows located before the bowshock for different IMF clock angles. The geomagnetic dipole tilt is zero, and the solar wind conditions have the normal values. They are the same kind of plot as the one in frame 1 of Figure 5-2. The colors suggest three groups of fluid elements: the first group with orange to red color, the second group with green to light blue color, and the third group with blue to dark blue color, according to the dwell time of the fluid element on a closed field line.

In the simulation, I find that the IMF clock angle may not be conserved near the magnetopause before the reconnection of an IMF field line with a geomagnetic field line occurs. The IMF field line section draping around the magnetopause is deformed

by $J \times B$ force. For the IMF with near positive 90 degree clock angle, such deformation makes the IMF to become more antiparallel to the southern dawn and northern dusk geomagnetic field lines and then makes reconnection possible. For negative 90 degree IMF clock angle, the IMF is deformed so that it becomes nearly antiparallel with the northern dawn and southern dusk geomagnetic field lines. As shown in Figure 6-2, a dawn-dusk field line near the subsolar point has northeast $J \times B$ force on dusk side of the boundary, and has southwest $J \times B$ force on dawn side of the boundary. The force along the field line has the shape of a sine curve with the maximum about 6 R_E away from the subsolar point. Such a distribution of the $J \times B$ force makes this field line become antiparallel to a southern dawn or a northern dusk geomagnetic field at tailward cusps.

In addition to the reconnection due to the antiparallel IMF and geomagnetic field at the reconnection location, there is another theory, i.e., the component reconnection where shear angles between the magnetospheric field and the IMF can be much less than 180° (*Fuselier et al.*, 1997, 2000; *Chandler et al.*, 1999; *Trattner et al.*, 2004). However, how the component reconnection occurs is still not clear. The component reconnection is considered to occur equatorward of the cusp at low latitudes. It is also not clear if it involves in a double reconnection process similar to the double high-latitude reconnection process that can capture the solar wind plasma.

Since I have not investigated the reconnection location and the shear angles in detail, I cannot rule out the possibility of component reconnection occurring in the simulation. However, the reconnection locations that I have seen so far during the analysis of the simulations, i.e., examining the location where the IMF becomes open or closed, are all at tailward of cusp. In the event that component reconnection can occur for shear angle near 90°, then any northward IMF field line has a good chance to reconnect with the tail lobe field lines extending straight tailward anywhere on

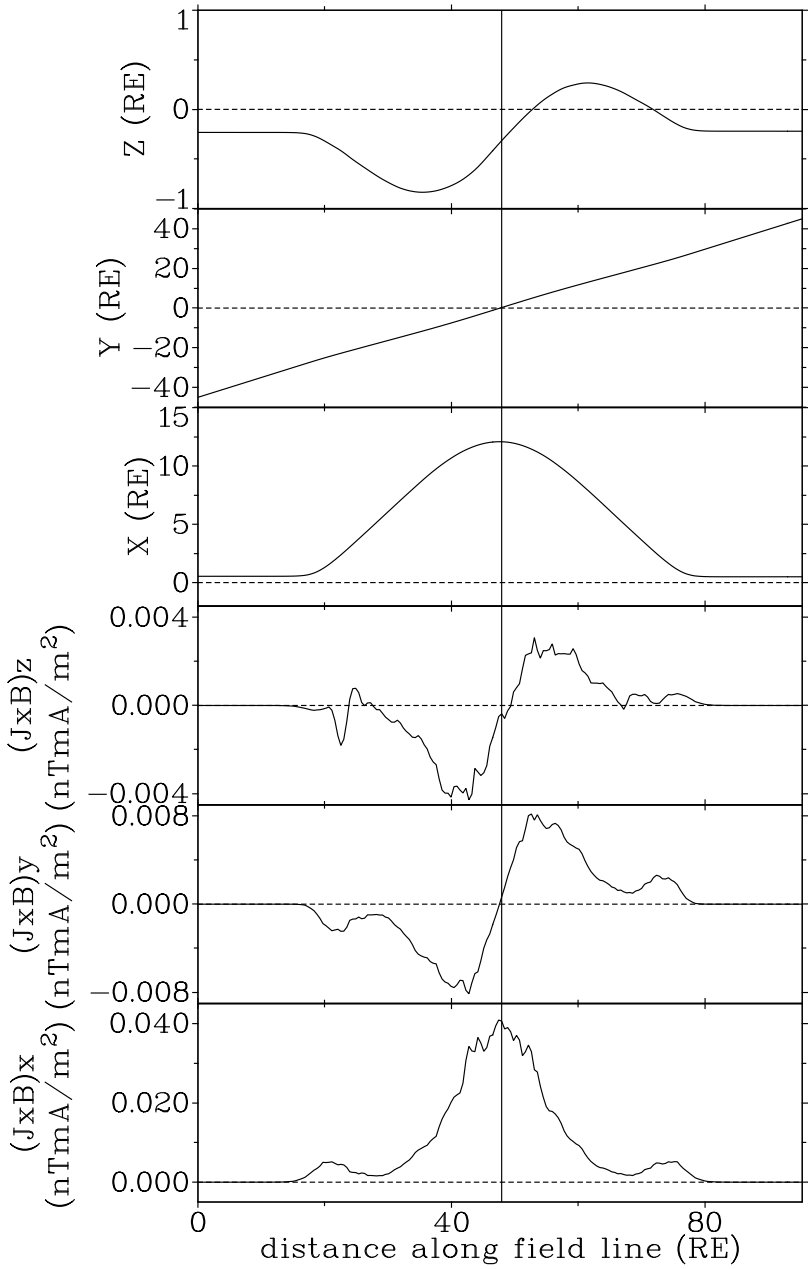

Figure 6-2: The $J \times B$ force distribution along a dawn-dusk magnetosheath magnetic flux tube from dawn to dusk looking from the Sun. The vertical solid line near the center corresponds the subsolar point.

the tail magnetopause. I do not see such reconnection occurring in our simulation. Therefore, I assume antiparallel reconnection plays a major role in the simulation.

In the simulation, I found that the IMF draping over the magnetopause can become antiparallel with open or closed field lines over a broad range of local time and thus can cause reconnection tailward of the cusp. An IMF field line can not only reconnect with an open field line, but can also reconnect with a new-closed field line convecting in the nightside. Here, high-latitude reconnection may not be an appropriate term, since reconnection may be able to occur near the dawn and dusk tail flanks. Tailward cusp reconnection may be a better term.

During such a double tailward cusp reconnection process, generally an IMF field line first reconnects with a magnetospheric field line at one side of the noon-midnight meridian in one hemisphere, then at the other side in the other hemisphere. The requirement that the two merging field lines are near antiparallel in our simulation, and the geometry of the field lines near the cusps constrains the places where reconnection can occur, and thus constrains the window size according to the IMF clock angle and determines the orientation of the window.

6.2.2 Geomagnetic dipole tilt angle dependence

Figure 6-3 and frame (b) of Figure 6-7 suggest that a small negative (anti-sunward) dipole tilt angle between 0° and -15° maximizes the entry window. More solar wind plasma is captured south (north) of the equatorial plane for positive (negative) tilt angle. The simulations show that a new-closed field line with its northern (or southern) part near high-latitude magnetopause in the tail will be more likely to participate in the high-latitude reconnection again and become open, as indicated by Figure 5-1, in which the closed1 field line changes to open3 field line. Taking the field lines as an example, when the geomagnetic dipole has a anti-sunward tilt angle about

15°, the southern parts of a new-closed field line is not likely near the high-latitude magnetopause. It then is less likely to participate in the high-latitude reconnection, and thus has more chance to convect into the magnetosphere.

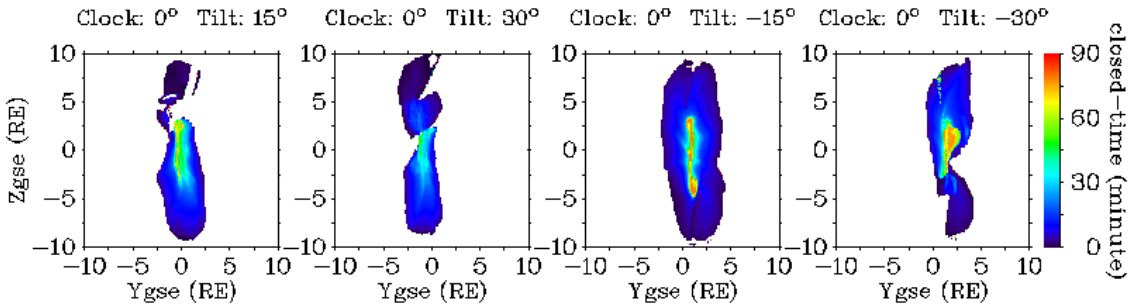

Figure 6-3: Solar wind entry windows located before the bowshock for different geomagnetic dipole tilt angles. The IMF is pure northward, and the solar wind conditions have the normal values.

The simulations show that when the dipole tilt angle is positive, an IMF flux tube first interconnects with a geomagnetic field flux tube at the northern cusp and later at the southern cusp. This is expected since an IMF flux tube with zero B_x will touch the northern cusp field first when the dipole tilt sunward. The initial IMF B_x is set to be zero in our simulations. The opposite sequence holds for negative dipole tilt angles. Most of the open2 field lines will consequently have footprints in the northern hemisphere for positive dipole tilt angle. Examining the FIMFLs along some flow paths flowing through the entry window for our simulations with dipole tilt angles of 15° and 30°, I find that all the FIMFLs become open with footprints in the northern hemisphere (not shown here). On the other hand, the FIMFLs become open with footprints in the southern hemisphere for tilt angles of −15° and −30°.

6.2.3 IMF magnitude dependence

The entry window becomes thinner in the y direction, and its area consequently become smaller when the IMF is stronger as shown in Figure 6-4 and frame (c) of Figure 6-7. As the IMF magnitude increases, the Alfvèn Mach number and magnetosonic Mach number decrease upstream of the bowshock. Previous MHD simulations (*Cairns and Lyon*, 1995) and theoretical studies (*Farris and Russell*, 1994) have shown that the standoff distance of the bowshock increases with decreasing Alfvèn Mach number or with decreasing magnetosonic Mach number. That means a larger IMF magnitude leads to a thicker magnetosheath. A thicker magnetosheath causes a fluid element to be diverted earlier and have a larger distance to the magnetopause, and thus have less chance to connect with the geomagnetic field, than the same fluid element flowing through a magnetosheath with shorter standoff distance of the bowshock. The lines with number 1, 2, and 3 in Figure 6-5 are the equatorial plane projections of three flow paths of the same fluid element for three different IMF magnitudes. The flow path with stronger IMF is sunward of the one with weaker IMF. That is, the flow path with stronger IMF is diverted farther away from the magnetopause than the path with weaker IMF. Therefore, the entry window with stronger IMF is thinner than that with weaker IMF.

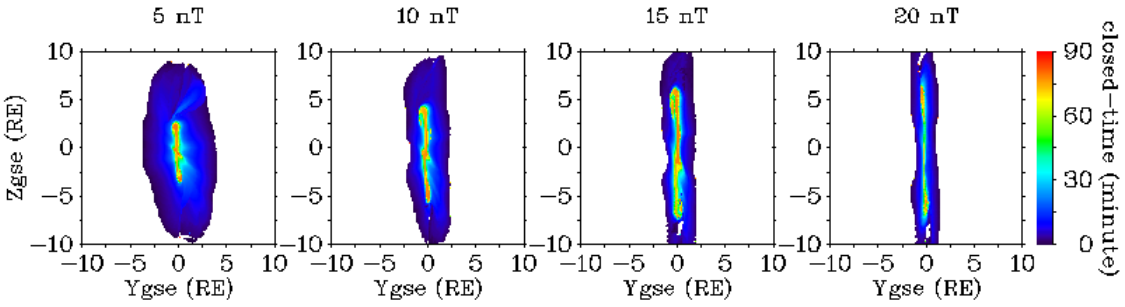

Figure 6-4: Solar wind entry windows located before the bowshock for different IMF magnitudes. The IMF clock angle and dipole tilt are both zero. The solar wind conditions have the typical values.

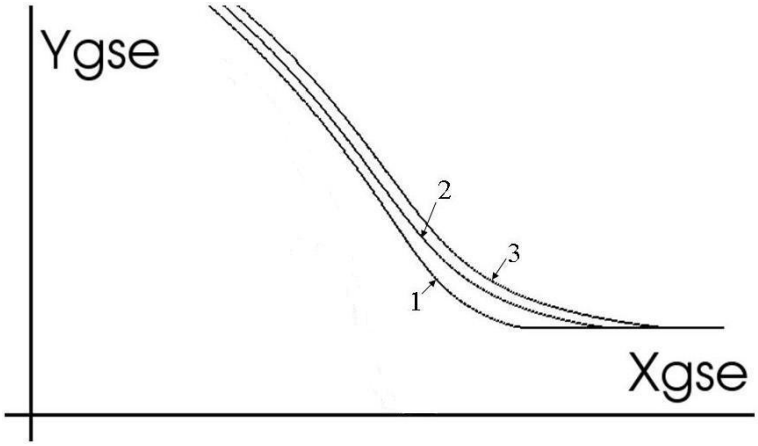

Figure 6-5: Solar wind flow paths projected on the GSE equatorial plane. The paths numbered 1, 2 and 3 are the flow paths of the same flow element for various IMF magnitudes: 5 nT, 15 nT, and 20 nT, respectively.

6.2.4 Solar wind dynamic pressure dependence

The pressure balance between the two sides of the magnetopause determines the diameter of the magnetosphere and the standoff distance of the subsolar point from the Earth. The pressure exerted by the solar wind on the nose of the dayside magnetopause is proportional to the dynamic pressure of the solar wind. Therefore, the size of the magnetosphere will decrease as the dynamic pressure increase. As shown in Figure 6-6, a smaller magnetosphere size will then lead to a smaller entry window because the captured IMF flux tubes are shorter. However, for low ($<\sim$400 km/s) and high ($>\sim$800 km/s) solar wind speed, the window size may not decrease linearly with increased solar wind speed as shown in frame (d) of Figure 6-7. The uncertainty of the window size is high for low or high solar wind speed compared to the normal speed of 450 km/s. This suggests that properties other than solar wind dynamic pressure, such as magnetic Mach number and plasma β, may also affect the entry window. However, further detail study is beyond the scope of present paper.

As the solar wind density or the velocity increases, the solar wind Alfvèn Mach

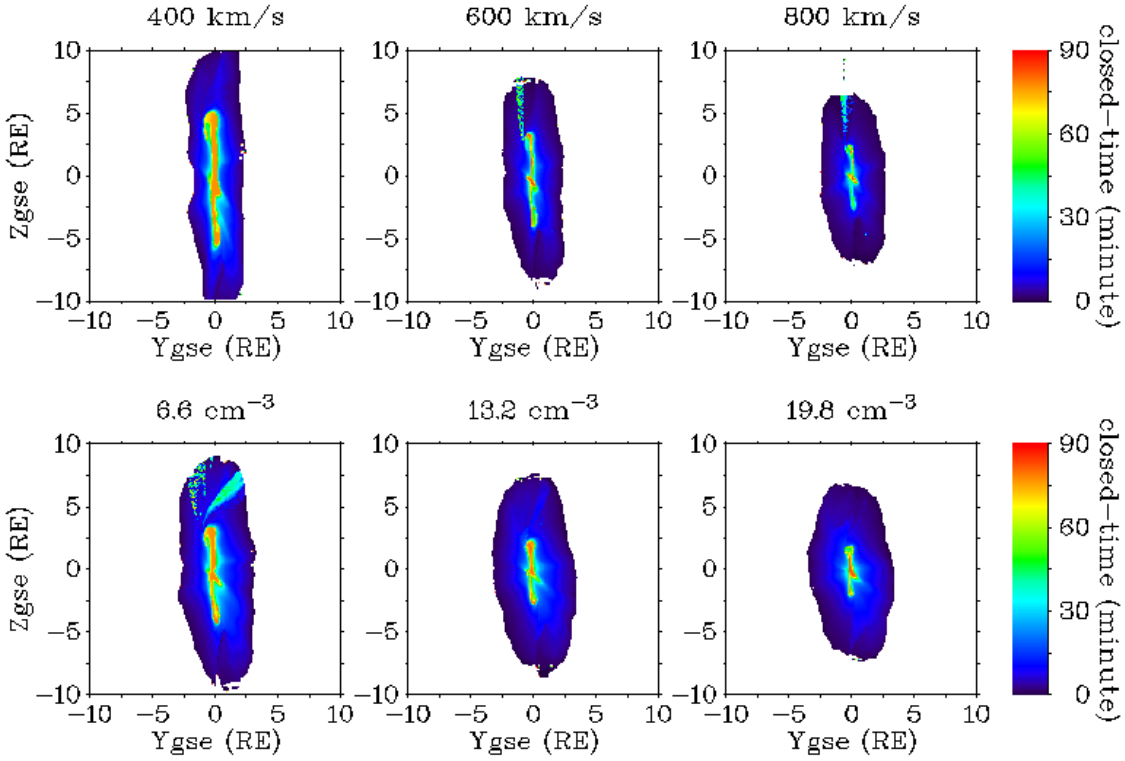

Figure 6-6: Solar wind entry windows located before the bowshock for different solar wind speed and density. The IMF clock angle and dipole tilt are both zero. The upper row entry windows have a solar wind density of 6.6 cm^{-3}, and the lower row entry windows have a solar wind velocity of 450 km/s.

number increases as well, and the standoff distance of bowshock decreases. In contrast to the case of increasing IMF magnitude, the entry window becomes wider in the Y_{gse} direction as solar wind density or velocity is increased, as shown by the entry windows in Figure 6-6.

6.3 Solar Wind Plasma Entry Rate

Although there may be other mechanisms of solar wind entry into the magnetosphere under northward IMF conditions, such as diffusive processes, I consider double high-latitude reconnection mechanism as the dominant process, because it is sufficient to form the cold dense plasma sheet in the simulation. I now estimate the solar wind plasma entry rate by measuring the amount of plasma that is captured by high-latitude reconnection per unit time. Specifically, the entering plasma per unit time is the product of the entry window area, the solar wind speed and the solar wind density at a location before the bowshock for constant uniform solar wind and IMF conditions.

This entry rate estimation avoids the use of detailed information about how the solar wind plasma entry occurs, and also does not require a detailed analysis of the reconnection process itself. The distribution of velocity and density on the separatrix surface is not uniform. The plasma passing the entry window located before the bowshock at the same time may not enter across the separatrix at the same time. However, as long as the entry is relatively steady and the window size is relatively constant, this estimate will be a good approximation for the real plasma entry rate. I have computed the entry window for a number of different times during the simulation. I find that the entry window sizes during a given time period differs only by small amounts except for simulations with extreme solar wind and IMF conditions. Therefore, I assume that the plasma entry is more or less continuous for typical

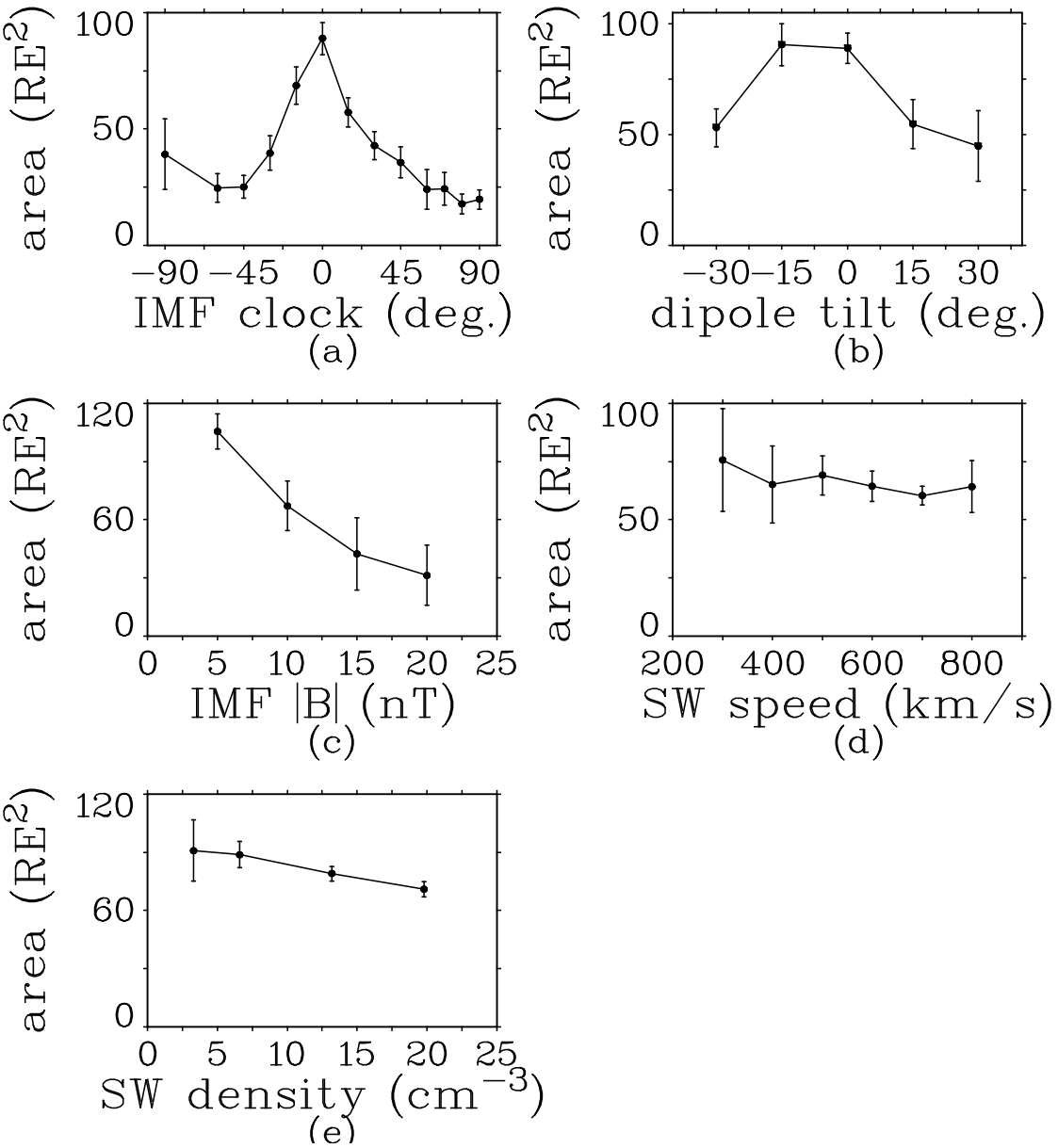

Figure 6-7: The area of entry window for various conditions. Each data point is an average of 9 entry windows computed for 9 different fluid element launching times. The error bar indicates the standard deviation of the variation of these 9 entry widows.

constant solar wind and IMF conditions.

Strictly speaking, I should only consider the first and second groups of plasma fluid elements discussed in section 5.4.2 to be the plasma that actually enters the magnetosphere because the fluid elements of the third group only stay on the closed field lines on the magnetosphere boundary for a short period of time. In my computation, I require 30 minutes of closed-time as the criterion to determine if a fluid element belongs to the third group or not. Figure 6-8 summaries the variation of the entry window area of long closed period and the entry rate represented by particle flux through the corresponding window area, with respect to geomagnetic dipole tilt angle, solar wind and IMF conditions. The variation of the particle flux shown in Figure 6-8 shows that the solar wind entry rate is on the order of 10^{26} to 10^{27} particles per second.

Frames (a1) and (a2) of Figure 6-8 show that due north IMF clock angle maximizes plasma entry. Frame (a) of Figure 6-7 shows a rather symmetric distribution of window size with respect to the IMF clock angle. However, IMF with positive clock angle leads to a larger entry rate than IMF with negative clock angle as shown in frames (a1) and (a2) of Figure 6-8. This asymmetry is significant and it is due to the ionosphere control of convection and will be discussed further below. Even though the entry rate decrease with increasing clock angle, there is still a significant amount of solar wind plasma entering the magnetosphere for 90° IMF clock angle.

Frames (b1) and (b2) of Figure 6-8 show that the entry rate is maximum when the geomagnetic dipole tilts anti-sunward for a small angle instead of zero angle, as a result of the reason discussed in section 5.2.

For the typical solar wind conditions stated in section 2, the solar wind entry is most efficient when the IMF magnitude is of the order of 10 nT as shown in frames (c1) and (c2) of Figure 6-8. It appears that a stronger IMF lets more captured plasma

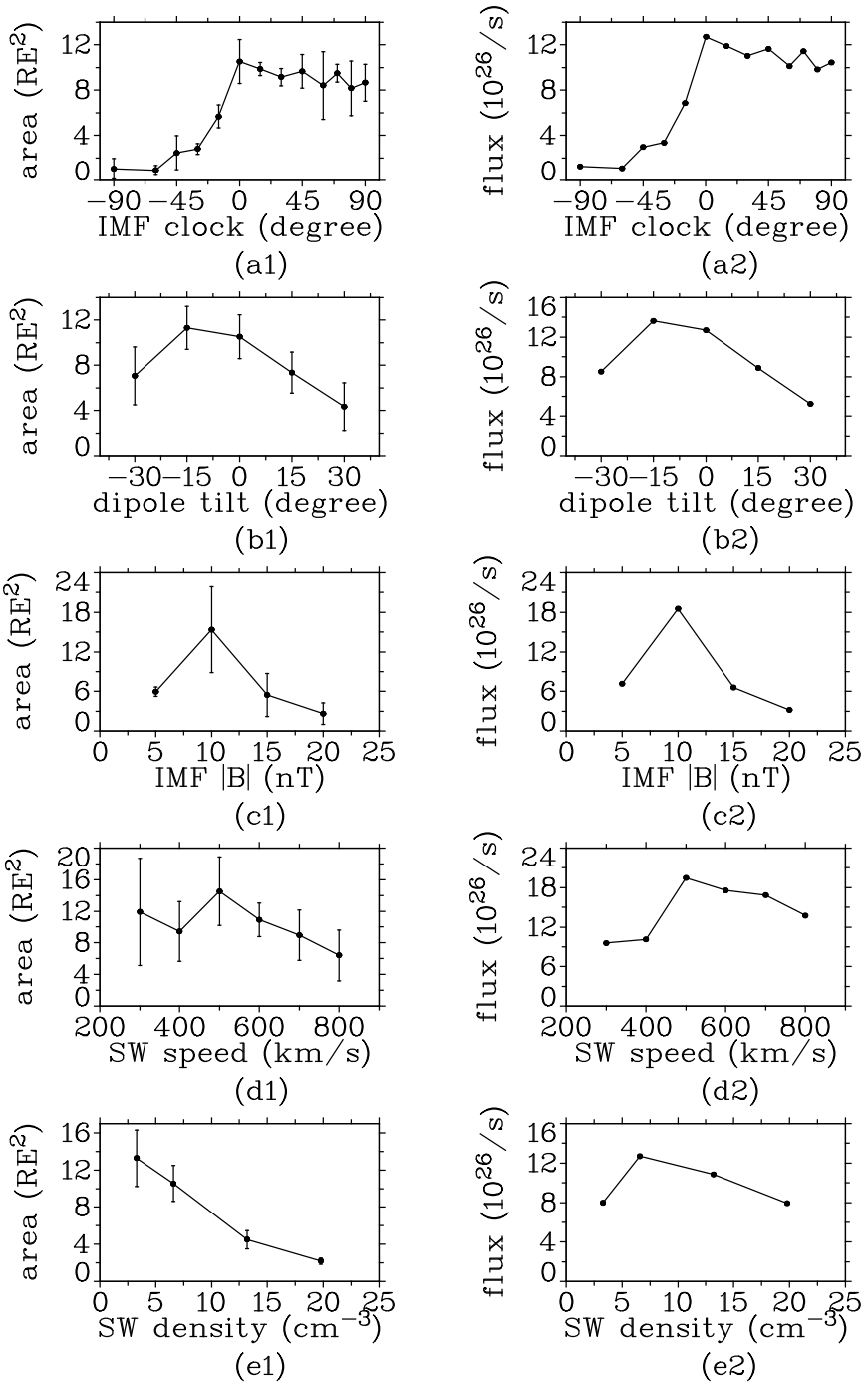

Figure 6-8: Left frames: variation of entry window's area of the fluid elements with closed-time longer than 30 minutes, corresponding to frames in Figure 6-7. Right frames: the corresponding variation of entry rate, which is a product of the area shown in left frames, the solar wind density and the solar wind speed. For parameter study of IMF clock angle, dipole tilt angle, and IMF magnitude, the solar wind density is set to be 6.6 cm^{-3}, and the solar wind speed is set to be 450 km/s.

enter deep inside the magnetosphere as a result of stronger $J \times B$ force acting on the newly created closed field lines. However, when the IMF is so strong that the entry window becomes very narrow, the entry rate is reduced.

The entry rate maximizes as a function of solar wind speed when the solar wind speed is ∼500 km/s for the typical solar wind conditions, as shown in frames (d1) and (d2) of Figure 6-8. It seems that low solar wind speed will let less solar wind plasma enter deep inside the magnetosphere. When solar wind speed is greater than ∼500 km/s, the decrease of the window size is more significant than the increase of the solar wind speed. Thus the entry rate decreases slightly as the solar wind speed increases.

Frames (e1) and (e2) of Figure 6-8 show that the solar wind entry rate also has a maximum value related to the solar wind density at about 6.6 cm^{-3}. This is because higher plasma density lets more plasma enter through the window per unit time, but also leads to a smaller entry window because of higher solar wind dynamic pressure. The entry rate consequently will reach a maximum when the density increases to a value at which the effect of decreasing area of entry window begins to be greater than the effect of increasing solar wind density.

In the present study the entry window and entry rate are computed after the IMF has been northward for at least 2 hours. Shortly after the IMF turns from southward to northward, the plasma and field configuration near the cusp area may be significantly different from the configuration found at a later time, as shown in Figure 6-9, because the magnetosphere is mostly open and more dynamic in electromagnetic and fluid properties when the IMF is southward. The size and shape of the entry window, and consequently the entry rate at the beginning of northward IMF condition may thus be significantly different from those several hours later.

During the long period northward IMF event on October 23, 2003, Cluster ob-

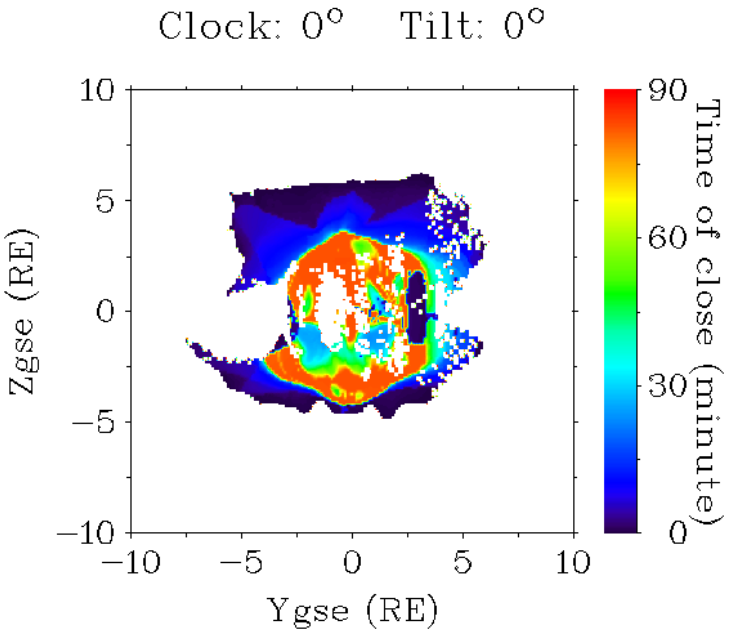

Figure 6-9: An example of the entry window located before the bowshock computed shortly after the southward IMF turns to northward IMF.

served the transition from a hot tenuous plasma sheet to a cold dense plasma sheet which remained at a nearly constant 1.5 cm^{-3} density for many hours. This transition took about 3 hours of northward IMF. To estimate the time needed to form the cold dense plasma sheet, I assume one piece of the CDPS near one side of tail flank to be 30 R_E long in X_{gse}, 10 R_E wide in Y_{gse}, and 5 R_E high in Z_{gse}. This volume estimate is based on the statistical spatial distribution of CDPS presented by *Fujimoto et al.* [2002]. The total volume of the two pieces of CDPS is thus $\sim 8 \times 10^{29}$ cm^3. Assuming the CDPS density is $\sim$1.5 cm^{-3}, and the net entry flux is $\sim 1 \times 10^{26}$ particles per second, it will take $\sim$3 hours to fill the volume. Although this is rather rough estimation, our simulation for this period has almost the same transition time from the hot tenuous plasma sheet to the cold dense plasma sheet.

In summary, the entry rate into the magnetosphere under northward IMF is on the order of 10^{26} to 10^{27} particles per second under constant typical solar wind and IMF conditions. However, the entry rate does not vary monotonically with most solar

wind and IMF parameters, but shows distinct and unexpected maxima. Although I have not investigated all possible parameter combinations, the plasma entry rate maximizes at $\sim -15^\circ$ geomagnetic dipole tilt, $\sim 0^\circ$ IMF clock angle, $\sim$10 nT IMF magnitude, $\sim$500 km/s solar wind speed and $\sim$6.6 cm^{-3} solar wind density. Future studies will refine these parameter dependence.

6.4 Effect of the Ionosphere

In the present study, the simulations are run with the OpenGGCM version that is coupled with CTIM, the NOAA Coupled Thermosphere Ionosphere Model. The magnetosphere model provides CTIM with the electron precipitation parameters along with the potential. CTIM then computes the ionosphere conductances self-consistently, and computes the ionospheric convection potential. The potential is then mapped back to the inner boundary of the magnetosphere MHD calculation where it is used as boundary condition for the flow and field integration. OpenGGCM can also be run without CTIM. In this case, the ionospheric conductance is set to be a constant uniform value, or a built-in self-consistent model is employed.

Comparing results between simulations with CTIM and simulations with constant ionospheric conductance, I find that the ionosphere has a significant effect on high-latitude reconnection rate and entry rate. For simulations with constant ionospheric conductance, the area of the entry window and the distribution of the closed-time on the window are more uniform and more symmetric with respect to the orientation of the IMF, as shown in Figure 6-10. When ionosphere conductance is uniform and constant, the entry rate and the corresponding effective entry window discussed in section 5.5 are symmetric with respect to positive and negative IMF clock angles. For example, the effective entry window for IMF clock angle of 30° and -30° are 1.24 ± 0.21 R$_E^2$ and 1.20 ± 0.15 R$_E^2$ respectively. By contrast, the corresponding values

shown in frame (a1) of Figure 6-8 are 9.16 ± 0.77 R_E^2 and 2.79 ± 0.49 R_E^2 respectively. Different conductance of the ionosphere thus results in a different size of the entry window. This may be a result of different reconnection rate of the high-latitude reconnection for different ionosphere conductance.

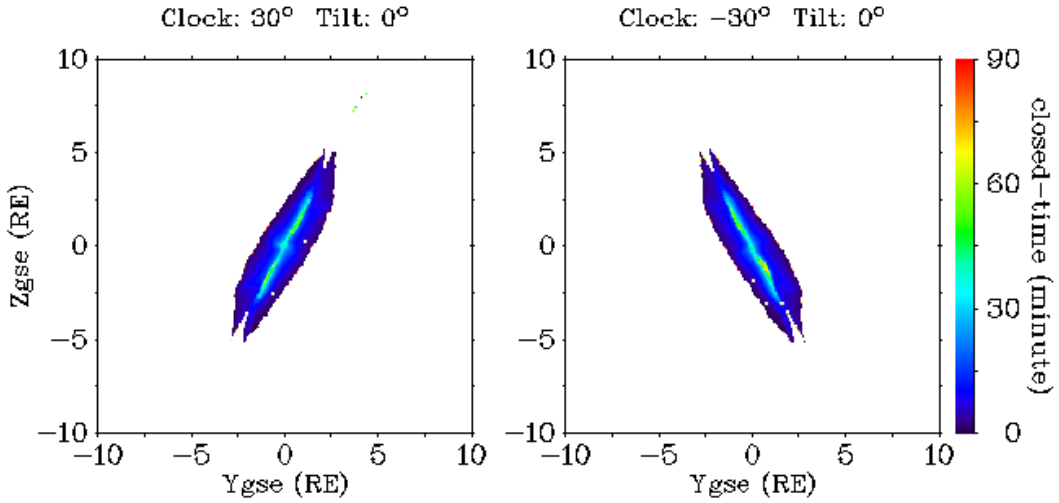

Figure 6-10: Solar wind entry windows located before the bowshock for IMF clock angles of 30° and −30° computed from simulations with constant uniform ionosphere conductance.

The total entry window area is rather symmetric between positive and negative IMF clock angle, for simulations with or without CTIM. However, the symmetry of effective entry window is broken for simulations with CTIM as shown in frames (a1) and (a2) of Figure 6-8, but is preserved for simulations with uniform conductance The effective entry window is the window through which the fluid elements stay on newly created closed field line longer than 30 minutes. For positive IMF clock angles, it seems that more captured fluid elements stay long ($>$ 30 minutes) on closed field lines. In other words, many new-closed field lines that have been convected to the night side (new-closed1 field lines) for negative IMF clock angle become open earlier ($<$ 30 minutes) than those for positive IMF clock angle. Thus, in simulations with

CTIM, many new-closed1 field lines for positive IMF clock angle participate in the next high-latitude reconnection at a later time than those for negative IMF clock angle.

The convection behavior of the captured fluid element discussed in section 5.4.2 may explain the asymmetric behavior. As discussed in section 5.4.2, the captured fluid elements flow southward (northward) and tailward on the dusk (dawn) side for either positive or negative IMF clock angle. That means the new-closed1 field lines are convected southward (northward) and tailward on the dusk (dawn) side. Consequently, the southern (northern) section of the new-closed1 field line on the dusk (dawn) side will come close to the southern (northern) magnetotail boundary, but the northern (southern) section of the new-closed1 field line on the dusk (dawn) side is not close to the northern (southern) magnetotail boundary, and is covered by a layer of open field. The closed1 field line in Figure 5-1 is an example in the dusk side. Such distribution of new-closed1 field lines in the tail will let the merging IMF field lines with positive clock angle have a smaller chance to connect with the new-closed1 field lines because the merging IMF field lines will most likely connect with open field lines on the northern tail boundary on the dusk side, and on the southern tail boundary on the dawn side. In the opposite case, the IMF field lines with negative clock angle are most likely aligned with the new-closed1 field lines. Therefore, the new-closed1 field line created from IMF with positive clock angle has better chance to stay closed for a longer time (> 30 minutes).

In the simulations with constant uniform ionosphere conductance, the convection behavior is symmetric between negative and positive IMF clock angle. That is, the new-closed1 field lines are convected southward (northward) and tailward on the dusk (dawn) side only for negative IMF clock angle. For positive IMF clock angle, the new-closed1 field lines are convected northward (southward) and tailward on the

dusk (dawn). Consequently, the effective entry window is symmetric between negative and positive IMF clock angle.

Thus, the ionosphere in reality causes an asymmetry in the magnetosphere boundary. *Atkinson and Hutchison* [1978] showed that the day-night conductivity gradient in the polar cap E region ionosphere squeezes the anti-sunward convective flow to the dawnside of the polar cap. The size of the effect increases with increasing conductivity gradient. They showed that this is the cause of the lack of the mirror symmetry in the flow pattern. The Region 1 Birkeland current pattern has been found to rotate longitudinally during periods with strong IMF B_y (*Erlandson et al.*, 1988; *Zhou et al.*, 2000). Since the currents in the ionosphere, the field aligned currents (FACs) and the currents on the magnetopause (Chapman-Ferraro currents) are all connected, and the plasma flow convection is affected by $\mathbf{J} \times \mathbf{B}$ force, the ionosphere is the source of the asymmetry found in this study.

The simulations in the present study show a higher effective entry rate for positive IMF clock angle. However, I can not rule out that there are certain conditions that may lead to the opposite result. Further parametric study will resolve this issue, but is beyond the scope of this paper.

CTIM provides a much more realistic ionosphere compared to a uniform-conductance ionosphere model (*Raeder et al.*, 2001). Therefore, the simulation shows that the ionosphere has a significant effect on the reconnection rate of high-latitude reconnection. The ionosphere also has an effect on the convection of the entering solar wind plasma, and consequently affects the entry rate with respect to different IMF clock angles.

6.5 Summary and Discussion

After establishing the dominant entry mechanism as the double high-latitude reconnection, and constructing the resulting entry window, I studied in this chapter how

and why the entry window changes with variations of parameters such as solar wind density, solar wind speed, solar wind pressure, IMF clock angle, IMF magnitude, and geomagnetic dipole tilt angle. Knowing the entry window size and assuming continuously entering uniform solar wind, I was able to estimate the entry rate with respect to common solar wind, IMF and geomagnetic dipole conditions.

The area of the entry window decreases as the magnitude of IMF clock angle increases. The orientation of the entry window aligns with the IMF clock angle. The area of the entry window decreases as the magnitude of IMF clock angle increases. The entry window for larger dipole tilt tends to be smaller. A stronger IMF leads to thinner entry window. As solar wind dynamic pressure increases, the entry window becomes smaller and wider.

I estimated the solar wind plasma entry rate to be on the order of 10^{26} to 10^{27} particles per second, depending on conditions. This estimation is consistent with the estimation made by *Eastman et al.* [1985] and *Richard et al.* [1994]. The entry rate is represented by the flux of the entering plasma that stays on closed field for more than 30 minutes. In general, the entry rate is highest when the IMF clock angle is about zero, the dipole tilt angle is $\sim -15^{\circ}$, the IMF magnitude is $\sim$10 nT, the solar wind speed is $\sim$500 km/s, and the solar wind density is $\sim$6.6 cm^{-3}. The accuracy of such parameter values can be improved with more simulations for more parameter values.

Simulations with different ionosphere conductance models show that the ionosphere changes the reconnection rate of high-latitude reconnection, and consequently change the size of the entry window. The ionosphere also affects the convection of the plasma in the tail, and consequently changes the effective entry rate by breaking the symmetry with respect to the noon-midnigh meridian.

Lavraud et al. [2005c] showed that an IMF flux tube will first participate in

reconnection at northern (southern) hemisphere, and then at southern (northern) hemisphere, when the geomagnetic dipole tilts sunward (anti-sunward), even for IMF with non-zero x component. I find the same phenomenon for IMF with zero x component in our simulations for dipole tilt angles of $+15°$, $+30°$, $-15°$, and $-30°$ in the GSE XZ plane.

IMF flux tubes near the dayside magnetopause are deformed by the $J \times B$ force. This deformation makes the effective clock angle of IMF near the magnetopause smaller for IMF with originally large clock angle (80°-90°), and thus facilitates the reconnection of IMF field lines that are oriented close to the dawn-dusk direction.

Twitty et al. [2004] found that cusp reconnection can occur for any IMF clock angle, measured by ACE, between $-90°$ and $90°$. Our entry windows shown in Figure 6-1 support this finding. On the other hand, *Lavraud et al.* [2006b] discovered that high-latitude reconnection occurs primarily when magnetosheath magnetic field line clock angle, measured by Cluster FGM, lies in the interval $[-60°, 60°]$. This observation can be explained by our simulation result that reveals the deformation of magnetosheath flux tube approaching the dayside magnetopause by $J \times B$ force. I have observed in our simulation that pure B_y IMF flux tube is tilted to a clock angle near $60°$ at the magnetopause, and reconnects with geomagnetic flux tubes. As noted by *Lavraud et al.* [2006b], their results were also potentially affected by orbit effects, owing to Cluster sampling high latitude regions primarily. *Crooker et al.* [1998] also showed in a MHD simulation that the pure B_y IMF field lines drape over the noon meridian, rather than the equator, and merge there with geomagnetic field lines.

The Kelvin-Helmholtz instability (KHI) has been proposed to be a process that enhances the diffusivity, and thus facilitates local mass transport and ion mixing at the flanks of the magnetopause under northward IMF condition (*Fujimoto and Terasawa*, 1994; *Nykyri and Otto*, 2001; *Nykyri et al.*, 2006; *Hasegawa et al.*, 2004). In the

simulations, I do not find any KHI signatures, probably as the result of insufficient grid resolution. However, KHI and high-latitude reconnection are not mutually exclusive as solar wind entry mechanism. It is possible that KHI contributes significant amount of magnetosheath plasma to the magnetosphere. The relation between the entry rate and the solar wind speed or density in the present study may help spacecraft in-situ observations to discriminate between the two processes, because KHI is expected to increase plasma entry with increasing solar wind velocity and/or density.

CHAPTER 7

SUMMARY AND CONCLUSIONS

In this dissertation study, I have studied: (1) the formation mechanism of the cold dense plasma sheet, (2) the formation mechanism of the superdense plasma sheet near the geosynchronous orbit, (3) the behavior of solar wind plasma entry into the magnetosphere under northward IMF conditions, and (4) the solar wind entry rate under northward IMF conditions for various solar wind, IMF, and geomagnetic dipole conditions.

In summary, the purpose of this dissertation study is to systematically investigate the solar wind plasma entry into the magnetosphere under northward IMF conditions, using global MHD magnetosphere simulations and incorporating data from observations. Since the dominant process that causes the solar wind entry in the simulations is double-high latitude reconnection, this dissertation study mainly investigates the behavior of the high-latitude reconnection processes and the outer magnetosphere under their influence.

I first studied the formation of the cold dense plasma sheet, which has been well observed and is directly related to the solar wind entry into the magnetosphere. I have chosen a typical CDPS event to study. In this event, the IMF is strong and almost purely northward, and lasts for almost 30 hours. The Cluster spacecraft observed not only the transition from a hot tenuous plasma sheet to a cold dense plasma

sheet, but also stayed in the cold dense plasma sheet during the whole event. The simulation for this event is very successful and reproduces nearly perfectly the CDPS as it is observed by Cluster. Through the analysis of this simulation, I found that magnetosheath plasma can flow directly into the magnetosphere as a result of double high-latitude reconnection. An IMF flux tube first reconnects with a geomagnetic flux tube tailward of the cusp of one hemisphere, then reconnects with another geomagnetic flux tube tailward of the cusp of the other hemisphere. A newly closed flux tube is consequently created and captures some magnetosheath plasma. The newly closed flux tube is subsequently convected into the dayside closed field region, or is convected tailward along the magnetopause. This simulation indicates that this process is the dominant mechanism that leads to the formation of a CDPS because the Kelvin-Helmholtz Instability (KHI), another potential large scale transportation process, is not reproduced in the simulation.

I have further run a simulation for another CDPS event on October 24/25, 2003, which is also a typical CDPS event. This OpenGGCM simulation also reproduced the observed CDPS and the depletion of this CDPS at the end of the northward IMF conditions. This simulation further confirms that the OpenGGCM model is valid in simulating the formation of a CDPS.

After the successful study of the formation of CDPS events, I have then studied the formation of the superdense plasma sheet, which is related to northward IMF conditions and to the cold dense plasma sheet. There are two conditions that has previously been found to lead to the detection of superdense plasma near the geosynchronous orbit. One is a southward turning of IMF after a long period of northward IMF. The other is a solar wind with very high dynamic pressure and northward IMF. In this dissertation study, I focus on the formation mechanism as a result of the first condition.

The SDPS event studied in this dissertation is well suited for finding out the formation mechanism. During this event, ACE and Wind provide the solar wind conditions, Cluster observed the CDPS related to the SDPS at $\sim$12 R_E in the tail and near midnight local time, and three LANL geosynchronous spacecraft detected the SDPS in the nightside at dawn, midnight and dusk locations, respectively. NASA IMAGE provides the auroral observations during this event. The ground magnetometer network "International Monitor for Aurora Geomagnetic Effects" (IMAGE) also provides observations of the north-south component of the ground magnetic field. Therefore, the chain of events following the southward turning of the IMF from northward condition is very well recorded.

I run a simulation with high grid resolution (30 million grid cells) for this event. This simulation successfully captures the observed phenomena in the plasma sheet at the Cluster location and near the geosynchronous orbit at the LANL spacecraft positions. This simulation further proves that the OpenGGCM is valid in studying the formation of the CDPS as well as the formation of SDPS. With this simulation, I describe in detail how the SDPS is formed from the pre-existing CDPS with a time series of the plasma density, plasma bulk velocity and magnetic field on the equatorial plane and the noon-midnight meridian in the simulation.

Both the observations and the simulation clearly show that the southward IMF causes the tail field to be compressed, and that it sets off the mid-tail reconnection that causes an auroral substorm. During this process, two pieces of CDPS above and below the equatorial plane are first compressed and slowly pushed toward the equatorial plane and toward the Earth as well. The reconnection then causes this piece of compressed CDPS to be pushed and accelerated toward the Earth, passing through the nightside portion of geosynchronous orbit.

Following the successful simulations for the CDPS events, I have further system-

atically studied the magnetosphere under northward IMF conditions using simulation runs with generic parameters used in the simulation of the CDPS event on October 23, 2003. I have run simulations for various solar wind, IMF and geomagnetic dipole conditions so that I could study the solar wind and magnetosphere interaction for these parameters.

To study the solar wind entry behavior as a result of high-latitude reconnection, I have classified the magnetic field in the solar wind and magnetosphere system into 7 categories (IMF1, IMF2, open1, open2, open3, closed1, and closed2) according to its topology (IMF, open or closed) and its formation characteristics in the process of reconnection. With the definition of these 7 types of magnetic field lines, I have identified the possible inter-connections between an IMF field line and an open field line, between an IMF field line and a closed field line, between an open field line and another open field line, or between an open field line and a closed field line, all at the high latitude magnetopause tailward of cusp.

The classification of the magnetic field lines and high-latitude reconnection processes helps one to trace the flow of solar wind fluid elements in the simulation. A fluid element is considered to be captured by double high-latitude reconnection and enters the magnetosphere if its frozen-in magnetic field line (FIMFL) changes from IMF field line to a closed field line. I have traced the solar wind flow from upstream and found that there is a certain window through which the solar wind plasma is captured by double high-latitude reconnection and enters the magnetosphere. This window depends on the IMF clock angle and other geophysical parameters.

Double high-latitude reconnection can not only capture the magnetosheath plasma, but this process can also release the entering plasma and let it join the solar wind again in the tail. There is a cycle of geomagnetic field line convection under northward IMF condition. That is, it changes from nightside open field line to dayside newly-

closed field line as a result of high-latitude reconnection, then it is convected to the nightside, and changes back to nightside open as a result of another high-latitude reconnection process. This convection cycle causes the footprint of the convecting field line to generate a corresponding convection pattern in the ionosphere, which has not been studied here, but should be studied eventually.

The time period for which an entering plasma fluid element stays on newly-created closed field varies according to its entry position. The plasma of an IMF flux tube entering at the dayside subsolar region has the longest life time of staying on closed field line. It may become part of the magnetosphere closed field region and populate the plasma sheet. The plasma fluid element of an IMF flux tube entering at a position farther away from the subsolar point has a smaller life time of staying on closed field line. That is, the new-closed flux tube created from such IMF flux tube is more likely to become open again, as a result of another reconnection event, after it was convected to the nightside of the cusp.

High-latitude reconnection also creates new open field lines draping the dayside magnetopause and convecting tailward around the magnetopause. Thus the newly created open field lines form an open layer on the magnetopause. The open field line created by high-latitude reconnection always extends either from the northern geomagnetic cusp toward the south, or from the southern cusp toward the north. Such field line distribution creates a layer of open field lines and exerts a torque on the magnetosphere.

The newly-created closed field lines that form as a result of double high-latitude reconnection also form a layer of closed field lines on the magnetopause. Thus, the boundary adjoining the magnetopause under northward IMF conditions is a two layer structure with the closed field layer beneath the open field layer.

After being captured by double high-latitude reconnection, the section of captured

magnetosheath flux tube is most likely convected tailward along the magnetopause. The convection is not symmetric with respect to dawn and dusk entering plasma even for pure northward IMF and uniform solar wind conditions. The convection is not symmetric either with respect to negative and positive IMF clock angles, and with respect to negative and positive geomagnetic dipole tilt angels. Consequently, the size and shape of the entry window is also asymmetric with respect to negative and positive IMF clock angle, and with respect to negative and positive geomagnetic dipole tilt angle. The asymmetry of convection is caused by the ionosphere because the day-night gradient of ionosphere conductance breaks the east-west convection symmetry because the gradient rotates the ionospheric convection pattern.

The paths of the entering plasma fluid elements and their destinations in the tail clearly indicate that the entered magnetosheath plasma fills the plasma sheet and form the CDPS mainly near the tail flanks and high latitude magnetopause since the entering plasma mainly convects along the magnetopause, and some may convect deep toward the midnight local time region. Such formation process is also well supported by the observations.

To study the solar wind entry efficiency, I have shown how the entry widow changes with various solar wind, IMF and geomagnetic dipole tilt conditions. The orientation of the entry window aligns with the IMF clock angle. The entry window with pure northward IMF has the largest area. Its area decreases as the magnitude of IMF clock angle increases. However, the window area for almost pure y IMF is non-vanishing. That means high-latitude reconnection can occur for any clock angle of northward IMF. Further study of the clock angle of the reconnecting magnetosheath field line shows that IMF is deformed mainly by $J \times B$ force. It changes its clock angle when it approaches the dayside magnetopause. IMF field lines that have a large clock angle ($\sim 80^\circ$ - $\sim 90^\circ$) in the solar wind is deformed to field lines with smaller clock angle

($\sim 60° - \sim 70°$). This clock angle change facilitates the reconnection of IMF with large clock angle at the high latitude magnetopause.

As the IMF magnitude increases, the entry window becomes thinner in the y direction but also longer. This is caused by the change of magnetosonic Mach number and consequently the change of thickness of the magnetosheath as a result of the IMF magnitude change. The entry window area decreases as the solar wind plasma density or the solar wind plasma speed, i.e., solar wind dynamic pressure, increases, because the size of the magnetopause is mainly controlled by solar wind dynamic pressure. The entry window increases its width in the dawn-dusk direction as well when the solar wind dynamic pressure increases. As solar wind density or velocity increases, the solar wind Alfvèn Mach number increases as well, and the standoff distance of the bow shock decreases. Consequently, in contrast to the case of the increasing IMF magnitude, the entry window becomes wider as solar wind density or velocity is increased. The geomagnetic dipole tilt also has significant effects on the size and shape of the entry window. If the dipole tilts toward the Sun, the solar wind plasma mainly enters the magnetosphere from the south part of the entry window, and vise versa.

In the simulation, an IMF field line without B_x component will first reconnect at northern (southern) high-latitude magnetopause and then reconnect at the southern (northern) high-latitude magnetopause, when the geomagnetic dipole tilts positively (negatively) toward the Sun. In other words, all the open field lines extend from northern (southern) cusp toward the south (north) for positive (negative) geomagnetic dipole tilt condition.

After calculating the entry windows for various conditions, I have the necessary information to estimate the solar wind plasma entry rate as a result of double high-latitude reconnection. I define the effective entry window as the portion through which

the entering plasma has closed-field life time greater than 30 minutes. I have computed the corresponding effective entry rate as the product of the area of the effective entry window, the solar wind density and the solar wind speed. The results show that the solar wind plasma entry rate as a result of double high-latitude reconnection is on the order of 10^{26} - 10^{27} particles per second depending on the geophysical conditions. My calculation shows that this entry rate is sufficient to fill the CDPS in two to three hours with plasma.

The entry window and the entry rate during early stage after a northward IMF turning is different from that at a time after several hours of northward IMF, because the electromagnetic environment is different for southward and northward IMF conditions. During the southward IMF period, the magnetosphere is more active, while it is quiet and calm during northward IMF conditions. I therefore compute the average entry rate by computing entry rates for nine different times at which the plasma passes through the entry window, and average the nine results.

As one might expect, the entry rate is affected by various solar wind, IMF and geomagnetic dipole tilt conditions. I found that there is a maximum entry rate with respect to the change of each such parameters. The parameter values at which the computed average entry rate reaches maximum are zero IMF clock angle, -15° dipole tilt angle, 10 nT IMF magnitude, 500 km/s solar wind speed, and 6.6 cm^{-3} solar wind plasma density.

Although high-latitude reconnection leads to an entry rate that is sufficient to form the cold dense plasma sheet, some other processes may also contribute. One of the significant processes is the Kelvin-Helmholtz instability (KHI). During the nonlinear phase of the KHI process, the plasma along the tail flank may swirl up and mix into the magnetosphere. Local reconnection may also occur in the swirl up waves and facilitate the mixing process. Since the grid resolution is not high enough in the tail,

the simulations in this study do not reproduce the KHI. Thus at this time I cannot estimate the contribution from a KHI. A very high resolution simulation that can reproduce the KHI should be able to estimate the entry rate due to this process and should also be able to find out the detailed entry mechanism related to a KHI.

This dissertation study has revealed many properties of the magnetosphere and described the characteristic behavior during the interaction between the solar wind and magnetosphere under northward IMF conditions. This study also raised more questions that need to be answered and showed that some processes need to be explored in more detail. For example, why some entered plasma can convect deep toward midnight local time location, how the convection of the entering plasma related to the studied parameters in detail, how the reconnection location changes, how the IMF flux tube is deformed in front of the dayside magnetopause, etc. In the simulations, I also found flux-ropes that formed at tailward of high-latitude reconnection location. How the open field layer acts on the magnetopause and affects the convection of entering plasma also needs to be studied further. How the ionospheric conductance breaks down the magnetospheric convection symmetric may need further study as well. To get better estimates of the entry rate, one may need to run many more simulations with more parameter values. An enhanced grid resolution may also help to refine the estimates. In this study, I have not studied the effects on ionosphere that result from high-latitude reconnection, which causes different ionospheric convection than under southward IMF conditions. In the future , I hope to further address theses questions and problems.

Bibliography

Atkinson, G., and D. Hutchison (1978), Effect of the day night ionospheric conductivity gradient on polar cap convective flow, *J. Geophys. Res.*, *83*, 725.

Axford, W. I., and C. O. Hines (1961), A unifying theory of high latitude geophysical phenomena and geomagnetic storms, *Can. J. Phys.*, *39*, 1433.

Baker, D. N., T. I. Pulkkinen, V. Angelopoulos, W. Baumjohann, and R. L. McPherron (1996), Neutral line model of substorms: Past results and present view, *J. Geophys. Res.*, *101*, 12,975.

Baumjohann, W., G. Paschmann, and C. A. Cattell (1989), Average plasma properties in the central plasma sheet, *J. Geophys. Res.*, *94*, 6597.

Berchem, J., J. Raeder, and M. Ashour-Abdalla (1995), Reconnection at the magnetospheric boundary: Results from global MHD simulations, in *Physics of the Magnetopause*, *AGU Geophysical Monograph*, vol. 90, edited by B. U. Sonnerup and P. Song, p. 205.

Berger, M. J., and P. Colella (1989), Local adaptive mesh refinement for shock hydrodynamics, *J. Comp. Phys.*, *82*, 64.

Berger, M. J., and J. Olinger (1984), Adaptive mesh refinement for hyperbolic partial differential equations, *J. Comp. Phys.*, *53*, 484.

Borovsky, J. E., M. F. Thomsen, and D. J. McComas (1997), The superdense plasma sheet: plasmaspheric origin, solar wind origin, or ionospheric origin?, *J. Geophys. Res.*, *102*, 22,089.

Borovsky, J. E., M. F. Thomsen, and R. C. Elphic (1998), The driving of the plasma sheet by the solar wind, *J. Geophys. Res.*, *103*, 17,617.

Cairns, I. H., and J. G. Lyon (1995), MHD simulations of Earth's bow shock at low Mach numbers: standoff distances, *J. Geophys. Res.*, *100*, 17,173.

Chandler, M. O., S. A. Fuselier, M. Lockwood, and T. E. Moore (1999), Evidence of component merging equatorward of the cusp, *J. Geophys. Res.*, *104*, 22,623.

Cowley, S. W. H. (1980), Plasma populations in a simple open model magnetosphere, *Space Sci. Rev.*, *26*, 217.

Cowley, S. W. H. (1981), Magnetospheric and ionospheric flow and the interplanetary magnetic field, in *The Physical Basis of the Ionosphere in the Solar-Terrestrial System*, AGARD-CP-295 4/1-4/14, AGARD Conf. Publ.

Cowley, S. W. H. (1982), The causes of convection in the Earth's magnetosphere: A review of developments during the IMS, *Rev. Geophys. Space Phys.*, *20*, 531–565.

Cowley, S. W. H. (1983), Interpretation of observed relations between solar wind characteristics and effects at ionospheric altitudes, in *High Latitude Space Plasma Physics*, edited by B. Hultquist and T. Hagfors, p. 225, New York, Plenum.

Cravens, T. E. (1997), *Physics of solar system plasmas*, Cambridge Univeristy Press, Cambridge, UK.

Crooker, N. U., J. G. Lyon, and J. A. Fedder (1998), MHD model merging with IMF B_y: lobe cells, sunward polar cap convection, and overdraped lobes, *J. Geophys. Res.*, *103*, 9143.

Dorelli, J. C. (2003), Effects of Hall electric fields on the saturation of forced antiparallel magnetic field merging, *Physics of Plasmas*, *10*, 3309.

Dungey, J. W. (1961), Interplanetary magnetic field and the auroral zones, *Phys. Rev. Lett.*, *6*, 47.

Dungey, J. W. (1963), The structure of the exosphere or adventures in velocity space, in *Geophysics, The Earth's Environment*, edited by C. DeWitt, J. Hieblot, and A. Lebeau, p. 550, Newark, N.J., Gordon and Breach.

Eastman, T. E., and E. W. Hones (1979), Characteristics of the magnetospheric boundary layer and magnetopause layer as observed by IMP 6, *J. Geophys. Res.*, *84*, 2019.

Eastman, T. E., B. Popielawska, and L. A. Frank (1985), Three-dimensional plasma observations near the outer magnetospheric boundary, *J. Geophys. Res.*, *90*, 9519.

Eriksson, G. M., et al. (2004), Global control of merging by the interplanetary magnetic field: Cluster observations of dawnside flank magnetopause reconnection, *J. Geophys. Res.*, *109*, 12,203.

Erlandson, R. E., L. J. Zanetti, T. A. Potemra, P. F. Bythrow, and R. Lundin (1988), IMF By dependence of region 1 Birkeland currents near noon, *J. Geophys. Res.*, *93*, 9804.

et al, J. A. S. (2004), Case studies of the dynamics of ionospheric ions in the Earth's magnetotail, *J. Geophys. Res.*, *109*, A01,212.

Evans, C. R., and J. F. Hawley (1988), Simulation of magnetohydrodynamic flows: A constrained transport method, *Astrophys. J.*, *332*, 659.

Fairfield, D. H. (1993), Solar wind control of the distant magnetotail: ISEE 3, *J. Geophys. Res.*, *98*, 21,265.

Fairfield, D. H., R. P. Lepping, E. W. Hones, S. J. Bame, and J. R. Asbridge (1981), Simultaneous measurements of magnetotail dynamics by IMP spacecraft, *J. Geophys. Res.*, *86*, 1396.

Fairfield, D. H., R. P. Lepping, L. A. Frank, K. L. Ackerson, W. R. Paterson, S. Kokubun, T. Yamamoto, K. Tsuruda, and M. Nakamura (1996), Geotail observations of an unusual magnetotail under very northward IMF conditions, *J. Geomag. Geoelec.*, *48*, 473.

Fairfield, D. H., A. Otto, T. Mukai, S. Kokubun, R. P. Lepping, J. T. Steinberg, A. J. Lazarus, and T. Yamamoto (2000), Geotail observations of the Kelvin-Helmholtz instability at the equatorial magnetotail boundary for parallel northward fields, *J. Geophys. Res.*, *105*, 21,159.

Farris, M. H., and C. T. Russell (1994), Determining the standoff distance of the bow shock: Mach number dependence and use of models, *J. Geophys. Res.*, *99*, 17,681.

Fedorov, A., E. Dubinin, P. Song, A. Skalsky, and E. Budnik (2001), Structure of the flank magnetopause for horizontal IMF: INTERBALL 1 observations, *J. Geophys. Res.*, *106*, 29,479.

Fedorov, A., E. Budnik, H. Stenuit, T. Moreau, and J. A. Sauvaud (2003), Antiparallel reconnection as a possible source of high- and low-latitude boundary layers, in *Earth's low-latitude boundary layer*, edited by P. T. Newell and T. Onsager, p. 139, AGU.

Fujimoto, M., and T. Terasawa (1994), Anomalous ion mixing within an MHD scale Kelvin-Helmholtz vortex, *J. Geophys. Res.*, *99*, 8601.

Fujimoto, M., A. Nishida, T. Mukai, Y. Saito, T. Yamamoto, and S. Kokubun (1996), Plasma entry from the flanks of the near-Earth magnetotail: Geotail observations in the dawnside LLBL and the plasma sheet, *J. Geomag. Geoelec.*, *48*, 711.

Fujimoto, M., T. Terasawa, T. Mukai, Y. Saito, T. Yamamoto, and S. Kokubun (1998), Plasma entry from the flanks of the near-Earth magnetotail: Geotail observations, *J. Geophys. Res.*, *103*, 4391.

Fujimoto, M., T. Mukai, and S. Kokubun (2002), The structure of the plasma sheet under northward IMF, in *Frontiers in magnetospheric plasma physics*, edited by M. Hoshino, Y. Omura, and L. J. Lanzerotti, COSPAR, Kanagawa, Japan, July 2002.

Fuller-Rowell, T. J., D. Rees, S. Quegan, R. J. Moffett, M. V. Codrescu, and G. H. Millward (1996), A coupled thermosphere-ionosphere model (CTIM), in *STEP Report*, edited by R. W. Schunk, p. 217, Scientific Committee on Solar Terrestrial Physics (SCOSTEP), NOAA/NGDC, Boulder, Colorado.

Fuselier, S. A., B. J. Anderson, and T. G. Onsager (1995), Particle signatures of magnetic topology at the magnetopause: AMPTE/CCE observations, *J. Geophys. Res.*, *100*, 11,805.

Fuselier, S. A., B. J. Anderson, and T. G. Onsager (1997), Electron and ion signatures of field line topology at the low-shear magnetopause, *J. Geophys. Res.*, *102*, 4847.

Fuselier, S. A., R. C. Elphic, and J. T. Gosling (1999), Composition measurements in the dusk flank magnetosphere, *J. Geophys. Res.*, *104*, 4515, doi:10.1029/1998JA900,137.

Fuselier, S. A., K. J. Trattner, and S. M. Petrinec (2000), Cusp observations of high- and low-latitude reconnection for northward interplanetary field, *J. Geophys. Res.*, *105*, 253.

Gombosi, T. I., D. L. DeZeeuw, C. P. T. Groth, K. G. Powell, and P. Song (1998), The length of the magnetotail for northward IMF: Results of 3D MHD simulations, in *Phys. Space Plasmas (1998)*, vol. 15, edited by T. Chang and J. R. Jasperse, p. 121, Cambridge, Mass.

Gopalswamy, N., L. Barbieri, G. Lu, S. P. Plunkett, and R. M. Skoug (2005), Introduction to the special section: Violent Sun-Earth connection events of October-November 2003, *Geophys. Res. Lett.*, *32*, L03S01.

Gosling, J. T., M. F. Thomsen, S. J. Bame, R. C. Elphic, and C. T. Russell (1990), Plasma flow reversals at the dayside magnetopause and the origin of asymmetric polar cap convection, *J. Geophys. Res.*, *95*, 8073.

Gosling, J. T., M. F. Thomsen, S. J. Bame, and R. C. Elphic (1991), Observations of reconnection of interplanetary and lobe magnetic field lines at the high-latitude magnetopause, *J. Geophys. Res.*, *96*, 14,097.

Gosling, J. T., M. F. Thomsen, G. Le, and C. T. Russell (1996), Observations of magnetic reconnection at the lobe magnetopause, *J. Geophys. Res.*, *101*, 24,765.

Gurnett, D. A., and A. Bhattacharjee (2005), *Introduction to Plasma Physics With Space and Laboratory Applications*, Cambridge University Press, Cambridge, United Kingdom.

Guzdar, P. N., X. Shao, C. C. Goodrich, K. Papadopoulos, M. J. Wiltberger, and J. G. Lyon (2001), Three-dimensional MHD simulations of the steady state magnetosphere with northward interplanetary magnetic field, *J. Geophys. Res.*, *106*, 275.

Harten, A., and G. Zwas (1972), Self-adjusting hybrid schemes for shock computations, *J. Comput. Phys.*, *9*, 568.

Hasegawa, H., M. Fujimoto, T. D. Phan, H. Rème, A. Balogh, M. W. Dunlop, C. Hashimoto, and R. TanDokoro (2004), Transport of solar wind into Earth's magnetosphere through rolled-up Kelvin-Helmholtz vortices, *Nature*, *430*, 755.

Horne, R. B., and R. M. Thorne (1997), Wave heating of He+ by electromagnetic ion cyclotron waves in the magnetosphere: Heating near the H+-He+ bi-ion resonance frequency, *J. Geophys. Res.*, *106*, A611,457.

Kessel, R. L., S.-H. Chen, J. L. Green, S. F. Fung, S. A. Boardsen, L. C. Tan, T. E. Eastman, J. D. Craven, and L. A. Frank (1996), Evidence of high-latitude reconnection during northward IMF: Hawkeye observations, *Geophys. Res. Lett.*, *23*, 583.

Kistler, L. M., C. Mouikis, A. Cao, H. Frey, R. H. Friedel, B. Klecker, I. Dandouras, G. Parks, and A. Balogh (2004), Impact of O^+ on substorm development, in *AGU Spring Meeting*, Montreal.

Kistler, L. M., et al. (2002), Motion of auroral ion outflow structures observed with CLUSTER and IMAGE FUV, *J. Geophys. Res.*, *107*, 1186.

Kivelson, M. G., and C. T. Russell (1995), *Introduction to Space Physics*, Cambridge University Press, Cambridge, United Kingdom.

Lavraud, B., M. H. Denton, M. F. Thomsen, J. E. Borovsky, and R. H. W. Friedel (2005a), Superposed epoch analysis of dense plasma access to geosynchronous orbit, *Ann. Geophys.*, *23*, 2519.

Lavraud, B., M. F. Thomsen, S. Wing, M. Fujimoto, M. H. Denton, J. E. Borovsky, A. Aasnes, K. Seki, and J. M. Weygand (2006a), Observation of two distinct cold, dense ion populations at geosynchronous orbit: local time asymmetry, solar wind dependence and origin, *Ann. Geophys.*, *24*, 3451.

Lavraud, B., et al. (2002), Cluster observations of the exterior cusp and its surrounding boundaries under northward IMF, *Geophys. Res. Lett.*, *29*, 1995.

Lavraud, B., et al. (2004), The exterior cusp and its boundary with the magnetosheath: Cluster multi-event analysis, *Ann. Geophys.*, *22*, 3039.

Lavraud, B., et al. (2005b), High-altitude cusp flow dependence on IMF orientation: A 3-year Cluster statistical study, *J. Geophys. Res.*, *110*, A02,209.

Lavraud, B., et al. (2005c), Characteristics of the magnetosheath electron boundary layer under northward interplanetary magnetic field: Implications for high-latitude reconnection, *J. Geophys. Res.*, *110*, A06,209.

Lavraud, B., et al. (2006b), Evidence for newly closed magnetosheath field lines at the dayside magnetopause under northward IMF, *J. Geophys. Res.*, *111*, A05,211.

Le, G., C. T. Russell, J. T. Gosling, and M. F. Thomsen (1996), ISEE observations of low-latitude boundary layer for northward interplanetary magnetic field: Implications for cusp reconnection, *J. Geophys. Res.*, *101*, 27,239.

Le, G., J. Raeder, C. T. Russell, G. Lu, S. M. Petrinec, and F. S. Mozer (2001), Polar cusp and vicinity under strongly northward IMF on April 11, 1997: Observations and MHD simulations, *J. Geophys. Res.*, *106*, 21,083.

LeMaire, J. (1977), Impulsive penetration of filamentary plasma elements into the magnetospheres of the Earth and Jupiter, *Planet. Space Sci.*, *25*, 887.

Lennartsson, W. (1992), A scenario for solar wind penetration of Earth's magnetic tail based on ion composition data from the ISEE 1 spacecraft, *J. Geophys. Res.*, *97*, 19,221.

Lennartsson, W., and E. G. Shelley (1986), Survey of 0.1 to 16 keV/e plasma sheet ion composition, *J. Geophys. Res.*, *91*, 3061.

Li, W., J. Raeder, J. Dorelli, M. Øieroset, and T. D. Phan (2005), Plasma sheet formation during long period of northward IMF, *Geophys. Res. Lett.*, *32*, L12S08.

Li, W., J. Raeder, J. Dorelli, M. F. Thomsen, and B. Lavraud (2007), Solar wind plasma entry into the magnetosphere under northward imf conditions, *J. Geophys. Res.*, *submitted*.

Lin, Y., and X. Y. Wang (2006), Formation of dayside low-latitude boundary layer under northward interplanetary magnetic field, *Geophys. Res. Lett.*, *33*, L21,104.

Matsuoka, A., K. Tsuruda, H. Hayakawa, T. Mukai, and A. Nishida (1996), Electric field structure and ion precipitation in the polar region associated with northward interplanetary magnetic field, *J. Geophys. Res.*, *101*, 10,711.

Moen, J., P. E. Sandholt, M. Lockwood, A. Egeland, and K. Fukui (1994), Multiple, discrete, arcs on sunward convecting field lines in the 14 - 15 MLT region, *J. Geophys. Res.*, *99*, 6113.

Newell, P. T., and C. I. Meng (2003), Magnetosheath injections deep inside the closed LLBL: a review of observation, in *Earth's low-latitude boundary layer*, edited by P. T. Newell and T. G. Onsager, p. 149, AGU.

Nykyri, K., and A. Otto (2001), Plasma transport at the magnetospheric boundary due to reconnection in Kelvin-Helmholtz vortices, *Geophys. Res. Lett.*, *28*, 3565.

Nykyri, K., A. Otto, B. Lavraud, C. Mouikis, L. M. Kistler, A. Balogh, and H. Rème (2006), Cluster observations of reconnection due to the Kelvin-Helmholtz instability at the dawnside magnetospheric flank, *Ann. Geophys.*, *24*, 2619.

Ogino, T. (1986), A three dimensional MHD simulation of the interaction of the solar wind with the Earth's magnetosphere: The generation of field aligned currents, *J. Geophys. Res.*, *91*, 6791.

Ogino, T., R. J. Walker, and M. Ashour-Abdalla (1994), A global magnetohydrodynamic simulation of the response of of the magnetosphere to a northward turning of the interplanetary magnetic field, *J. Geophys. Res.*, *99*, 11,027.

Øieroset, M., M. Yamauchi, L. Liszka, and B. Hultqvist (1999), Energetic ion outflow from the dayside ionosphere: Categorization, classification, and statistical study, *J. Geophys. Res.*, *104*, 24,915.

Øieroset, M., T. D. Phan, M. Fujimoto, L. Chan, R. P. Lin, and R. Skoug (2002), Spatial and temporal variations of the cold dense plasma sheet: Evidence for a low-latitude boundary layer source?, in *AGU Monograph on Earth's Low-Latitude Boundary Layer*, vol. 133, edited by P. T. Newell and T. G. Onsager, p. doi:10.1029/133GM25.

Øieroset, M., J. Raeder, T. D. Phan, S. Wing, J. P. McFadden, W. Li, M. Fujimoto, H. Rème, and a. Balogh (2005), Global cooling and densification of the plasma sheet during an extended period of purely northward IMF on October 22-24, 2003, *Geophys. Res. Lett.*, *32*, L12S07.

Omelchenko, A. N., O. L. Vaisberg, and C. T. Russell (1983), Further analysis of plasma bursts in Earth's boundary layer at high latitudes, *Cosmic Research*, *21*, 687.

Onsager, T. G., and J. D. Scudder (2003), Low-latitude boundary layer formation by magnetic reconnection, in *Earth's low-latitude boundary layer*, edited by P. T. Newell and T. G. Onsager, p. 111, AGU.

Onsager, T. G., J. D. Scudder, M. Lockwood, and C. T. Russell (2001), Reconnection at the high-latitude magnetopause during northward interplanetary magnetic field conditions, *J. Geophys. Res.*, *106*, 25,467.

Parker, E. N. (1996), The alternative paradigm for magnetospheric physics, *J. Geophys. Res.*, *101*, 10,587.

Parks, G. K. (2004), *Physics of Space Plasmas*, Westview Press, Boulder, CO.

Paschmann, G., W. Baumjohann, N. Sckopke, T. D. Phan, and H. Luhr (1993), Structure of the dayside magnetopause for low magnetic shear, *J. Geophys. Res.*, *98*, 13,409.

Petschek, H. E. (1964), Magnetic field annihilation, in *The Physics of Solar Flares*, edited by W. N. Hess, p. 425, NASA Spec. Publ. SP-50.

Phan, T. D., G. Paschmann, A. Raj, V. Angelopoulos, D. Larson, and R. P. Lin (1998), Wind observations of the halo/cold plasma sheet, in *Substorms-4*, edited by S. Kokubun and Y. Kamide, Terra Scientific/Kluwer Academic, Boston.

Phan, T. D., R. P. Lin, S. A. Fuselier, and M. Fujimoto (2000), Wind observations of mixed magnetosheath-plasma sheet ions deep inside the magnetosphere, *J. Geophys. Res.*, *105*, 5497.

Phan, T. D., et al. (1997), Low-latitude dusk flank magnetosheath, magnetopause, and boundary layer for low magnetic shear: Wind observations, *J. Geophys. Res.*, *102*, 19,883.

Phan, T. D., et al. (2003), Simultaneous Cluster and IMAGE observations of cusp reconnection and auroral proton spot for northward IMF, *Geophys. Res. Lett.*, *30*, 1509.

Pilipp, W. G., and G. Morfill (1978), The formation of the plasma sheet resulting from plasma mantle dynamics, *J. Geophys. Res.*, *83*, 5670.

Powell, K. G., P. L. Roe, T. J. Linde, T. I. Gombosi, and D. L. DeZeeuw (1999), A solution-adaptive upwind scheme for ideal magnetohydrodynamics, *J. Comp. Phys.*, *154*, 284.

Priest, E. R., and T. G. Forbes (2006), *Magnetic Reconnection: MHD Theory and Applications*, Cambridge University Press, Cambridge, United Kingdow.

Raeder, J. (1995), Global MHD simulations of the dynamics of the magnetosphere: Weak and strong solar wind forcing, in *Proceedings of the Second International Conference on Substorms*, edited by J. R. Kan, J. D. Craven, and S.-I. Akasofu, p. 561, Geophysical Institute, Univ. of Alaska Fairbanks.

Raeder, J. (1999), Modeling the magnetosphere for northward interplanetary magnetic field: Effects of electrical resistivity, *J. Geophys. Res.*, *104*, 17,357.

Raeder, J. (2003), Global Geospace Modeling: Tutorial and Review, in *Space Plasma Simulation*, edited by J. Büchner, C. T. Dum, and M. Scholer, Springer Verlag, Berlin Heidelberg New York.

Raeder, J., R. J. Walker, and M. Ashour-Abdalla (1995), The structure of the distant geomagnetic tail during long periods of northward IMF, *Geophys. Res. Lett.*, *22*, 349.

Raeder, J., J. Berchem, and M. Ashour-Abdalla (1996), The importance of small scale processes in global MHD simulations: Some numerical experiments, in *The Physics of Space Plasmas*, vol. 14, edited by T. Chang and J. R. Jasperse, p. 403, MIT Cent. for Theoret. Geo/Cosmo Plasma Phys., Cambridge, Mass.

Raeder, J., Y. L. Wang, and T. Fuller-Rowell (2001), Geomagnetic storm simulation with a coupled magnetosphere - ionosphere - thermosphere model, in *Space Weather, AGU Geophys. Monogr. Ser.*, vol. 125, edited by P. Song, G. Siscoe, and H. J. Singer, p. 377, American Geophysical Union.

Raeder, J., et al. (1997), Boundary layer formation in the magnetotail: Geotail observations and comparisons with a global MHD model, *Geophys. Res. Lett.*, *24*, 951.

Rème, H., C. Aoustin, M. Bosqued, I. Dandouras, and the CIS-team (2001), First multispacecraft ion measurements in and near the Earth's magnetosphere with the identical Cluster Ion Spectrometry (CIS) Experiment, *Ann. Geophys.*, *19*, 1303.

Richard, R. L., R. J. Walker, and M. Ashour-Abdalla (1994), The population of the magnetosphere by solar winds ions when the interplanetary magnetic field is northward, *Geophys. Res. Lett.*, *21*, 2455.

Rosenbauer, H., H. Grunwaldt, M. D. Montgomery, G. Paschmann, and N. Sckopke (1975), Heos 2 plasma observations in the distant polar magnetosphere: The plasma mantle, *J. Geophys. Res.*, *80*, 2723.

Russell, C. T. (1972), The configuration of the magnetosphere, in *Critical Problems of Magnetospheric Physics*, edited by E. R. Dyer, p. 1, Washington, D. C., Nat. Acad. of Sci.

Russell, C. T., and R. C. Elphic (1979), ISEE observations of flux transfer events at the dayside magnetopause, *Geophys. Res. Lett.*, *6*, 33.

Sckopke, N., G. Paschmann, G. Haerendel, B. U. O. Sonnerup, S. J. Bame, T. G. Forbes, E. W. Hones, and C. T. Russell (1981), Structure of the low-latitude boundary layer, *J. Geophys. Res.*, *86*, 2099.

Sod, G. A. (1985), *Numerical Methods in Fluid Dynamics*, Cambridge University Press, Cambridge.

Song, P., and C. T. Russell (1992), Model of the formation of the low-latitude boundary layer for strongly northward interplanetary magnetic field, *J. Geophys. Res.*, *97*, 1411.

Song, P., D. L. DeZeeuw, T. I. Gombosi, C. P. T. Groth, and K. G. Powell (1999), A numerical study of solar wind-magnetosphere interaction for northward interplanetary magnetic field, *J. Geophys. Res.*, *104*, 28,361.

Sonnerup, B. U. O., and L. J. Cahill (1967), Magnetopause structure and attitude from Explorer 12 observations, *J. Geophys. Res.*, *72*, 171.

Sonnerup, B. U. O., and L. J. Cahill (1968), Explorer 12 observations of the magnetopause current layer, *J. Geophys. Res.*, *73*, 1757.

Spreiter, J. R., A. L. Summers, and A. Y. Alksne (1966), Hydromagnetic flow arround the magnetosphere, *Planet. Space Sci.*, *14*, 223.

Stenuit, H., et al. (2001), A study of ion injections at the dawn and dusk polar edges of the auroral oval, *J. Geophys. Res.*, *106*, 29,619.

Strangeway, R. J., and J. Raeder (2001), On the transition from collisionless to collisional magnetohydrodynamics, *J. Geophys. Res.*, *106*, 1955.

Strangeway, R. J., R. C. Elphic, W. J. Peria, and C. W. Carlson (2000), FAST observations of electromagnetic stresses applied to the polar ionosphere, in *Magnetospheric Current Systems, AGU Monogr. Ser.*, vol. 118, edited by S.-I. Ohtani, p. 21, American Geophysical Union.

Terasawa, T., et al. (1997), Solar wind control of density and temperature in the near-earh plasma sheet: WIND/GEOTAIL collaboration, *Geophys. Res. Lett.*, *24*, 935.

Thomsen, M. F., J. E. Borovsky, R. M. Skoug, and C. W. Smith (2003), Delivery of cold, dense plasma sheet material into the near-Earth region, *J. Geophys. Res.*, *108*, 1151, doi: 10.1029/2002JA009,544.

Thorne, R. M., and B. T. Tsurutani (1991), *Physics of space plasmas, SPI conference proceedings and reprint series, number 10*, Scientific Publishers, Inc., Cambridge, MA.

Trattner, K. J., S. A. Fuselier, and S. M. Petrinec (2004), Location of the reconnection line for northward interplanetary magnetic field, *J. Geophys. Res.*, *109*, A03,219.

Treumann, R. A. (1997), Theory of super-diffusion for the magnetopause, *Geophys. Res. Lett.*, *24*, 1727.

Troshichev, O. A. (1990), Global dynamics of the magnetosphere for northward IMF conditions, *J. Atmos. Terr. Phys.*, *52*, 1135.

Tsurutani, B. T., G. S. Lakhina, L. Zhang, J. S. Pickett, and Y. Kasahara (2003), ELF/VLF plasma waves in the low latitude boundary layer, in *Earth's low-latitude boundary layer*, edited by P. T. Newell and T. G. Onsager, p. 189, AGU.

Twitty, C., T. D. Phan, G. Paschmann, B. Lavraud, H. Rème, and M. Dunlop (2004), Cluster survey of cusp reconnection and its IMF dependence, *Geophys. Res. Lett.*, *31*, 19,808.

Usadi, A., A. Kageyama, K. Watanabe, and T. Sato (1993), A global simulation of the magnetosphere with a long tail: Southward and northward interplantary magnetic field, *J. Geophys. Res.*, *98*, 7503.

Wang, Y. L. (2003), The plasma depletion layer, *UCLA PhD Dissertation*.

Watanabe, K., and T. Sato (1990), Global simulation of the solar wind-magnetosphere interaction: The importance of its numerical validity, *J. Geophys. Res.*, *95*, 75.

Wing, S., and P. T. Newell (1998), Central plasma sheet ion properties as inferred from ionosphere observations, *J. Geophys. Res.*, *103*, 6785.

Wing, S., and P. T. Newell (2002), 2D plasma sheet ion density and temperature profiles for northward and southward IMF, *Geophys. Res. Lett.*, *29*, 1307.

Woch, J., and R. Lundin (1992), Signatures of transient boundary layer processes observed with Viking, *J. Geophys. Res.*, *97*, 1431.

Yau, A. W., E. G. Shelley, W. K. Peterson, and L. Lenchyshyn (1985), Energetic auroral and polar ion outflow at DE 1 altitudes: Magnitude, composition, magnetic activity dependence, and long-term variations, *J. Geophys. Res.*, *90*, 8417.

Yee, K. S. (1966), Numerical solution of initial boundary value problems involving Maxwell's equations in isotropic media, *IEEE Trans. Antenna Propagation*, *AP-14*, 302.

Zalesak, S. T. (1981), Very high order pseudospectral flux-corrected transport (FCT) algorithms for conservation laws, in *Proceedings of the Fourth IMACS International Symposium on Computer Methods for Partial Differential Equations*, edited by R. Vichnevetsky and R. S. Stepleman, p. 126, IMACS, Rutgers University, New Brunswick.

Zhou, X. W., C. T. Russell, and G. Le (2000), Local time and interplanetary magnetic field By dependence of field-aligned currents at high altitudes, *J. Geophys. Res.*, *105*, 2533.